博士論文

Geometrical Structures and Reactivity of Gas-Phase Precious Metal Clusters with Small Molecule

（気相貴金属クラスターと小分子の幾何構造及び反応性）

山口 雅人

Contents

Chapter 1

General introduction

1.1. Introduction

Global economic growth has been accompanied by a corresponding increase in negative anthropogenic environmental impacts. NO_x, which are emitted industrially and from internal combustion engines, are harmful to the human respiratory system, and their decomposition (such as to N_2 and O_2) remains a major issue.[1]

One of the solutions already used is the promotion of decomposition using a catalyst. Catalysts made from precious metals that are used for the after-treatment of automobile exhaust gas are known as "three-way catalysts." The current priority is making these catalysts smaller by using minute particles as catalysts. The use of nano-sized catalysts, with a large specific surface area, can result in a more efficient decomposition reaction. However, proven reserves of precious metals are limited, and it is therefore necessary to elucidate their properties to establish alternative methods. The catalytic ability of nanoparticles has been evaluated by depositing them on a substrate in a vacuum and reacting them with gases. We can then measure their catalytic cycle. In this method, the interaction between the nanoparticles and the substrate cannot be ignored, regardless of how clean the substrate is. Therefore, the catalytic properties are evaluated by considering the substrate. In addition, alloying is a potentially viable method for producing more efficient catalysts. For alloys, however, not only the selection of elements to be added, but also the ratio of elements is an important factor. Therefore, even if candidate elements are identified using computational science, a vast number of combinations should nonetheless be examined experimentally.

On the other hand, it has been suggested that clusters (i.e. ensembles of limited numbers of atoms) can be regarded as models for the active center of nano-sized catalysts.[2,3] Gas phase clusters in a vacuum are isolated spatially and do not interact. Moreover, this method allows us to determine the different compositions of alloying clusters simultaneously using a mass spectrometer.

1.2. Clusters

As the size of the aggregated atoms decreases, the substance acquires new properties. Aggregates with a sub-micrometer size are called nanoparticles, and those with a size of approximately 10^{-8} m are called clusters. The number of atoms in these clusters is typically below a few hundred. Clusters are roughly classified into the following five groups according to bonding types for maintaining their structure: van der Waals, hydrogen, covalent, ionic, and metal.

Clusters that have a specific number of atoms are sometimes produced more than others and exhibit inertness against the reactant. This stability is strongly dependent on their symmetry and/or the number of electrons, that is, whether magic numbers are present. When the number of electrons is 2, 8, 18, 20, 34, 40, …, they could achieve stability as explained by the Woods-Saxon potential model. The simplest example, as demonstrated by Knights et al., is Na_n clusters.[4] The Na_n clusters, using metal bonds, are stably generated when $n = 8, 20, 40$, and 58 (Figure 1.1). A sodium atom has one valence electron in the 3s orbital, and clusters are simply stabilized when the amount of n corresponds to the magic number. Castleman et al. elucidated the stability of the Al_{13}^- cluster, which showed dramatically decreased reactivity with O_2 (Figure 1.2).[5] An aluminum atom has three valence electrons, and anionic Al_{13} possesses 40 valence electrons. However, Al_n^- does not exhibit such strong stability at other magic numbers. This characteristic can be explained by the reduced area exposed on the surface. The number of atoms is expressed as follows:

1	$n = 1$
12	$n = 2$
$12 + 30$	$n = 3$
$12 + 30 \times 2 + 1/2 \times 20$	$n = 4$
…	
$10m^2 - 20m + 12$	$n = m \ (n > 1)$ (1.1)

where n implies the n-th layer. Hence, the total number of atoms is the sum of this series, expressed as

$$\sum(10n^2 - 20n + 12) - 1 \tag{1.2}$$

For example, in M_n become stable while $n = 13, 55, 147, ...$ The results of the xenon clusters experiment was in accordance with this prediction (Figure 1.3).[6] In the case of aluminum, stability results from the combination of 40 electrons and the geometrical symmetry of 13 atoms.

One of the most famous clusters is C_{60}, which is held together by covalent bonds, and was discovered by Smalley.[7] This structure is also known as buckminsterfullerene or buckyball (Figure 1.4). The combination of pentagons and hexagons produced a symmetric structure by covalent bonding.

One advantage of using clusters is the simplicity of the experiment. By using the cluster as a proxy for the nano-sized catalyst, the reactivity of various combinations of atoms can be screened. Additionally, cluster experiments in the gas phase are performed in an isolated field, whereas clusters stabilized by ligands or supported by substrates are affected by those materials. Since clusters can be regarded as active centers in heterogeneous catalysts, high-speed analysis can be conducted by screening their reactivity in combination with mass spectrometry.[3] In this context, precious metals are suitable materials to evaluate the reactivity and decomposition mechanisms of clusters.

1.3. Gold Clusters

Gold is inactive in bulk; hence, it was not considered as a potential catalyst. In 1987, Haruta reported on the oxidation reaction of CO catalyzed by nano-sized gold clusters at low temperature.[8] Since this remarkable finding, extensive experiments and calculations on Au clusters and nanoparticles have been carried out. In the case of gold clusters, reactions with small-molecule gases such as O_2, CO, NO and NO_2 were investigated. Cox et al. reported comprehensively on the reactivity of Au_n anions, neutrals and cations.[9] A particularly interesting finding was the size dependence of the adduction of O_2. According to reports, Au_n^+ does not react with O_2, except when $n = 10$. However, the anionic Au cluster showed that only one O_2 reacts when n is odd. This propensity is explained in terms of the electron shells within the clusters composed of Au atoms, which have one 6s electron in valence. Therefore, Au_n^- ($n =$ even) has an odd number of electrons. Metiu and coworkers claimed that this excess electron is transferred into the π^* of O_2.[10] This closed shell has been confirmed in the experiment using photoelectron spectroscopy, and provides a remarkable example of the size dependence of the Au cluster. In the study of CO molecules, the oxidation of CO has been reported for clusters with specific sizes.[11,12] Regarding gas phase clusters, Bernhardt and coworkers showed CO oxidation reactions in Au_2^-, and Whetten and coworkers showed CO oxidation reactions in Au_6^-.[13,14] In an alloy cluster containing Au, He and coworkers produced an oxidation reaction using TiO_2, which is known as a supporter of transition metal oxides (TMO).[15] According to

this study, Au acts as a CO trapper and electron acceptor in $Au(TiO_2)_nO_m^-$ clusters. However, research regarding NO, especially NO decomposition, is limited. Xing et al. reported a disproportionation reaction from NO to NO_2 and N_2O on Au_nNO^- (n = 4, 6, and 8), as follows:

$$Au_n^- + 3NO \rightarrow Au_nNO_2^- + N_2O \ (n = 4, 6, \text{ and } 8) \tag{1.3}$$
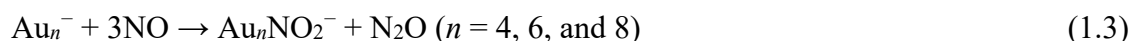
To understand these reactions, the geometrical structures and electron states of the product and reactant are important because of their contribution to the reactivities. The structure of clusters has been clarified using mobility measurements, infrared spectrometry, photoelectron spectrometry, and quantum chemical calculations. Kappes et al. measured the mobility for Au_n^q (n = 1−13, q = +1; n = 1-15, q = −1).[16,17] It was suggested that cationic clusters formed planer structures until n = 7, whereas anions remained until n = 11, and much larger clusters developed three-dimensional structures. Owing to the principle of mobility, small geometrical differences could not be identified if the isomer had the same reaction cross-section. In addition, structures were identified using infrared and photoelectron spectroscopy.[3,18,19] Infrared and photoelectron spectroscopy provide more accurate information such as vibrational frequencies and electron states. Structures in which O_2, NO, and CO were adsorbed have also been reported.[20–24] However, accurate quantum chemistry calculations are required because these results can only provide information about typical vibrations of ligands. In the computational method, however, determination of the geometries of large clusters requires computer resources. Each method has advantages and disadvantages.

1.4. Rh Clusters as Group IX in Precious Metals

Rh and Ir are metals that have already been used as catalysts. To establish an alternative catalyst or enhance their abilities, intensive experiments on the reaction mechanism using clusters, including alloys, have been widely conducted.

Much interest in Rh has centered on its decomposition of NO. It has been confirmed that the NO decomposition reaction is promoted by the adsorption of multiple NO molecules on the Rh cluster.[25,26] Mackenzie et al. reported that the decomposition of NO by small Rh_n^+ ($7<n<13$) clusters took place at room temperature, whereas larger clusters ($n>14$) showed no evidence of N_2 desorption. Additionally, in a heating experiment (Thermal desorption spectroscopy, TDS) conducted by Tawaraya et al., O_2- and O_4-adducted clusters were observed at $n>5$ with increasing temperature. In any case, the key to the decomposition reaction of NO may be the increase in internal energy. Experiments using infrared spectroscopy also showed

that the first NO on Rh_n (n = 6−16) clusters is molecularly adsorbed at a low temperature of 223 K.[27] A TDS analysis of Rh alloy clusters doped with Ta ($Rh_nTa_{6-n}NO^+$ (n = 0−6)) showed that more dissociated NO was produced by adding Ta compared with that produced in the case of a pure Rh cluster.[28]

1.5. Contents of Thesis

In this thesis, I investigated the reactivities and geometrical structures of precious metals in the presence of small molecules. Precious metals, including Au, Rh, and Ir, and small molecules, including O_2, NO, and NO_2, were used. The clusters in this study were prepared in the gas phase in a vacuum chamber. Detailed descriptions of the experimental setup, apparatuses, reaction conditions, etc., are comprehensively presented in each chapter. I will therefore restrict myself to only explaining them briefly here.

The target precious metal clusters were produced by laser ablation in the presence of He carrier gas that was injected by a pulsed valve in the vacuum chamber. For the reaction with small molecules, reactants were seeded in the carrier gas or introduced from another valve with lower pressure. The clusters generated here passed through the skimmer and were detected by a time-of-flight mass spectrometer (TOF-MS). Herein, the clusters' reactions were detected as the change in the mass-to-charge ratio.

In Chapters 2−4 the generated clusters entered the extension tube before passing through the skimmer. By heating this tube (referred to as the heating tube), the clusters reach thermal equilibrium by colliding with the surrounding He. The temperature dependence of the clusters can be recorded by plotting the change in the mass spectrum. This thermal desorption spectroscopy (TDS) is similar to thermal programmed desorption (TPD) in surface science. If the intensity ratio of the clusters varied, namely, by increasing the intensity of M_n^+ and decreasing the intensity of M_nG_m while increasing the temperature, the activation energy (E_a) of desorption can be determined using the Arrhenius equation.

$$I(T) = I_0\exp(-k(T)t) \tag{1.4}$$

$$K(T) = A\exp(-E_a/k_BT) \tag{1.5}$$

where $I(T)$ is the cluster intensity at temperature T, I_0 is the cluster intensity at 0 K, $k(T)$ is the reaction rate constant, t is the reaction time, A is the pre-exponential factor, E_a is the activation energy and k_B is the Boltzmann constant. In the desorption reaction, the activation energy, E_a,

is larger than the difference in the formation energy, ΔE., obtained by quantum chemistry calculations. Therefore, it provides a result that is closer to the actual catalytic reaction.

Chapters 6 and 7 , the clusters are cooled in the copper block before passing through the skimmer to produce Ar-adsorbed clusters. After passing through the skimmer, the clusters are irradiated by a counter-propagated IR laser before TOF-MS analysis. Clusters exposed to the IR laser absorb photons when the vibrational frequency matches the resonance of the laser. This increases the internal energy of the clusters. Ar atoms then desorb from the cluster with this internal energy. This variation is recorded as a difference in the mass spectrum. This method is called infrared multiple photon dissociation (IRMPD). Instead of the direct desorption of small molecules, the messenger method is used, which involves the detachment of rare gases such as Ar. Since the physical adsorption of rare gas does not change the vibrational frequency of the target cluster (because of its weak bond), and since it can be desorbed with a small number of photons, it is easy to obtain the IRMPD peak. For example, the energy of a photon with a typical NO frequency of 1700 cm^{-1} corresponds to 0.211 eV. The calculated stabilization energy of the molecularly adsorbed NO ($Rh_5Ta^+ + NO$) is 2.04 eV. Therefore, it is necessary to absorb at least 10 photons. In addition, if the skeletal vibration of the metal cluster appears at approximately 300 cm^{-1}, the energy per photon of the infrared laser would be 0.037 eV, and it would be necessary to absorb 55 photons for the detachment of NO. Here, it is assumed that NO is molecularly adsorbed and that there is no activation barrier in this desorption process. However, if NO has adsorption energy, it requires many more photons for detachment. On the other hand, rare gases, such as Ar, are adsorbed on Rh_5TaNO^+ at 0.18 eV. This weakly bound Ar can be detached by one-photon absorption corresponding to 1700 cm^{-1}. Even at 300 cm^{-1}, only 5 photons are sufficient for detachment. IRMPD experiments are also conducted in Chapter 5. However, the messenger method was not used in this experiment. Instead, the clusters across the IR laser cavity and the small molecule were desorbed directly by irradiation.

Chapter 2 reports the results of $Au_nO_2^-$. Although the oxygen adsorption process in the CO oxidation reaction was important, oxygen attached clusters were reported by computational studies, and few experimental values were available. In this chapter, the activation energies of the O_2 desorption reaction were accurately determined for $n = 2-14$ by heating (TDS).

Chapter 3 shows the results for $Au_nO_m^-$ using N_2O as the oxidant substitute for O_2. Oxygen was adsorbed sequentially, and clusters of $Au_nO_m^-$ ($n = 1-12$, $m = 0, 1, 2,\ldots$) were generated with increasing N_2O concentrations. Unlike the O_2 experiment, oxygen adsorption

was observed even when n was an odd number. Heating by the TDS process showed no O_2 desorption at $n = 2, 4$; $m = 2$ until 1000 K. The clusters with the same composition exhibited different responses, suggesting the formation of isomers.

Chapter 4 describes the experiment on $Au_4N_nO_m^-$ ($n = 0-3$, $m = 0-6$) clusters examined by concentration dependence and the TDS technique. The NO adsorption reaction was detected with increasing NO concentration in a stepwise manner. NO desorption was also observed sequentially by heating, and all NO molecules detached at 600 K, whereas $Au_4NO_2^-$, produced by introducing NO, maintained its composition until 900 K. The characteristics of $Au_4NO_2^-$ were compared in a control experiment using pure NO_2 gas.

In Chapter 5, the experiment using an infrared laser was applied to the $Au_4N_nO_m^-$ system. The IRMPD spectra for Au_4NO^-, $Au_4N_2O_2^-$, and $Au_4NO_2^-$ indicated that the small molecules, NO and NO_2 in this experiment, were adsorbed intact. We also discussed the NO disproportionation reaction using obtained geometries.

Up to here, I introduced the gold cluster as one of the samples that had been regarded inert in the bulk phase, but have catalytic potential in nanoparticles. On the other hand, nano-sized particles in the platinum group have already been surveyed a long time. Therefore, I focused on enhancing catalytic reactivity by alloying. Chapter 6 describes the forms of NO adsorption in Rh_nTa^+ alloy clusters. The geometric structure of one Ta-doped Rh_nTaNO^+ ($n = 2-8$) cluster was determined by IRMPD spectroscopy. Evaluation of the dissociation ability on the first NO could help to elucidate the NO decomposition reaction of Rh. Ta doping certainly promoted the NO decomposition reaction, and NO was dissociated and adsorbed in all the observed compositions. This is consistent with the TDS experiment on $Rh_nTa_{6-n}NO^+$ ($n = 0-6$) reported by Tawaraya et al. On the clusters, oxygen atom is always adsorbed on the Ta terminal site while the adsorption site of the nitrogen atom varied depending on n.

Chapter 7 describes the IRMPD experiment on Ir_6NO^+. The adsorption of NO was investigated, with approximately 50% of NO being dissociatively adsorbed, and the remaining 50% being molecularly adsorbed. In addition, the IRMPD spectrum suggests that multiple dissociatively adsorbed clusters exist at the same time. According to quantum chemical calculations, these isomers appeared in the reaction pathway for NO dissociation. This result was compared with the experiments of Rh_6, Rh_5Ta, and Rh_5Ir, and it was suggested that the oxophilicity of the clusters determines their dissociation ability.

Finally, in Chapter 8, the overall summary and future prospects are presented.
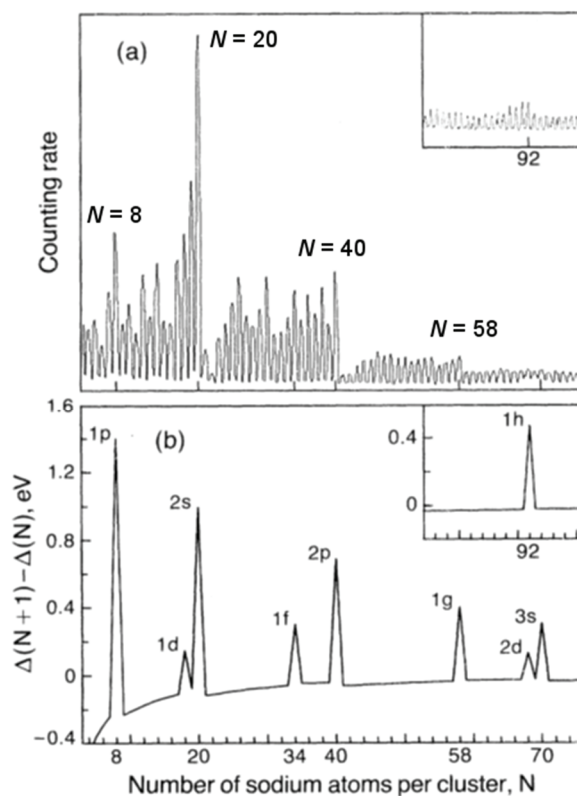
1.6. References

(1)   Schiermeier, Q. The Science behind the Volkswagen Emissions Scandal. *Nature* **2015**, https://doi.org/10.1038/nature.2015.18426.

(2)   Johnson, G. E.; Mitrić, R.; Bonačić-Koutecký, V.; Castleman, A. W. Clusters as Model Systems for Investigating Nanoscale Oxidation Catalysis. *Chem. Phys. Lett.* **2009**, *475* (1–3), 1–9, https://doi.org/10.1016/J.CPLETT.2009.04.003.

(3)   Lang, S. M.; Bernhardt, T. M. Gas Phase Metal Cluster Model Systems for Heterogeneous Catalysis. *Phys. Chem. Chem. Phys.* **2012**, *14* (26), 9255–9269, https://doi.org/10.1039/c2cp40660h.

(4)   Knight, W. D.; Clemenger, K.; de Heer, W. A.; Saunders, W. A.; Chou, M. Y.; Cohen, M. L. Electronic Shell Structure and Abundances of Sodium Clusters. *Phys. Rev. Lett.* **1984**, *52* (24), 2141–2143, https://doi.org/10.1103/PhysRevLett.52.2141.

(5)   Leuchtner, R. E.; Harms, A. C.; Castleman, A. W. Thermal Metal Cluster Anion Reactions: Behavior of Aluminum Clusters with Oxygen. *J. Chem. Phys.* **1989**, *91* (4), 2753–2754, https://doi.org/10.1063/1.456988.

(6)   Echt, O.; Sattler, K.; Recknagel, E. Magic Numbers for Sphere Packings: Experimental Verification in Free Xenon Clusters. *Phys. Rev. Lett.* **1981**, *47* (16), 1121–1124, https://doi.org/10.1103/PhysRevLett.47.1121.

(7)   Kroto, H. W.; Heath, J. R.; O'Brien, S. C.; Curl, R. F.; Smalley, R. E. C60: Buckminsterfullerene. *Nature* **1985**, *318* (6042), 162–163, https://doi.org/10.1038/318162a0.

(8)   Haruta, M.; Kobayashi, T.; Sano, H.; Yamada, N. Novel Gold Catalysts for the Oxidation of Carbon Monoxide at a Temperature Far Below 0 ℃. *Chem. Lett.* **1987**, *16* (2), 405–408, https://doi.org/10.1246/cl.1987.405.

(9)   Cox, D. M.; Brickman, R.; Creegan, K.; Kaldor, A. Gold Clusters: Reactions and Deuterium Uptake. *Zeitschrift für Phys. D Atoms, Mol. Clust.* **1991**, *19* (1–4), 353–355, https://doi.org/10.1007/BF01448327.

(10)   Mills, G.; Gordon, M. S.; Metiu, H. The Adsorption of Molecular Oxygen on Neutral and Negative Au_n Clusters ($n = 2-5$). *Chem. Phys. Lett.* **2002**, *359* (5–6), 493–499, https://doi.org/10.1016/S0009-2614(02)00746-7.

(11) Sanchez, A.; Abbet, S.; Heiz, U.; Schneider, W.-D.; Häkkinen, H.; N. Barnett, R.; Landman, U. When Gold Is Not Noble: Nanoscale Gold Catalysts. *J. Phys. Chem. A* **1999**, *103* (48), 9573–9578, https://doi.org/10.1021/jp9935992.

(12) Yoon, B.; Häkkinen, H.; Landman, U.; Wörz, A. S.; Antonietti, J.-M.; Abbet, S.; Judai, K.; Heiz, U. Charging Effects on Bonding and Catalyzed Oxidation of CO on Au8 Clusters on MgO. *Science (80-.).* **2005**, *307* (5708), 403–407, https://doi.org/10.1126/science.1104168.

(13) Socaciu, L. D.; Hagen, J.; Bernhardt, T. M.; Wöste, L.; Heiz, U.; Häkkinen, H.; Landman, U. Catalytic CO Oxidation by Free Au_2^- Experiment and Theory. *J. Am. Chem. Soc.* **2003**, *125*, 10437–10445, https://doi.org/10.1021/ja027926m.

(14) Wallace, W. T.; Whetten, R. L. Coadsorption of CO and O_2 on Selected Gold Clusters: Evidence for Efficient Room-Temperature CO_2 Generation. *J. Am. Chem. Soc.* **2002**, *124*, 7499–7505, https://doi.org/10.1021/JA0175439.

(15) Li, X.-N.; Yuan, Z.; He, S.-G. CO Oxidation Promoted by Gold Atoms Supported on Titanium Oxide Cluster Anions. *J. Am. Chem. Soc.* **2014**, *136* (9), 3617–3623, https://doi.org/10.1021/ja412608b.

(16) Gilb, S.; Weis, P.; Furche, F.; Ahlrichs, R.; Kappes, M. M. Structures of Small Gold Cluster Cations (Au_n^+, $n<14$): Ion Mobility Measurements versus Density Functional Calculations. *J. Chem. Phys.* **2002**, *116* (10), 4094–4101, https://doi.org/10.1063/1.1445121.

(17) Furche, F.; Ahlrichs, R.; Weis, P.; Jacob, C.; Gilb, S.; Bierweiler, T.; Kappes, M. M. The Structures of Small Gold Cluster Anions as Determined by a Combination of Ion Mobility Measurements and Density Functional Calculations. *J. Chem. Phys.* **2002**, *117* (15), 6982–6990, https://doi.org/10.1063/1.1507582.

(18) Li, J.; Li, X.; Zhai, H.-J.; Wang, L.-S.; Lyon, J. T.; Meijer, G.; Fielicke, A. Structures of Neutral Au7, Au19, and Au20 Clusters in the Gas Phase. *Science (80-.).* **2003**, *299* (5608), 864–867, https://doi.org/10.1126/science.1079879.

(19) Wang, L. M.; Wang, L. S. Probing the Electronic Properties and Structural Evolution of Anionic Gold Clusters in the Gas Phase. *Nanoscale* **2012**, *4* (14), 4038–4053, https://doi.org/10.1039/c2nr30186e.

(20) Sun, Q.; Jena, P.; Kim, Y. D.; Fischer, M.; Gantefor, G. Interactions of Au Cluster Anions with Oxygen. *J. Chem. Phys.* **2004**, *120* (14), 6510–6515, https://doi.org/10.1063/1.1666009.

(21) Fielicke, A.; Helden, G. Von; Meijer, G.; Simard, B.; Rayner, D. M. Direct Observation of Size Dependent Activation of NO on Gold Clusters. *Phys. Chem. Chem. Phys.* **2005**, *7* (23), 3906–3909, https://doi.org/10.1039/b511710k.

(22) Zhai, H.-J.; Kiran, B.; Dai, B.; Jun Li, A.; Wang, L.-S. Unique CO Chemisorption Properties of Gold Hexamer: $Au_6(CO)_n^-$ ($n = 0-3$). *J. Am. Chem. Soc.* **2005**, *127*, 12098–12108, https://doi.org/10.1021/JA052618K.

(23) Pal, R.; Wang, L.-M.; Pei, Y.; Wang, L.-S.; Zeng, X. C. Unraveling the Mechanisms of O2 Activation by Size-Selected Gold Clusters: Transition from Superoxo to Peroxo Chemisorption. *J. Am. Chem. Soc.* **2012**, *134* (22), 9438–9445, https://doi.org/10.1021/ja302902p.

(24) Woodham, A. P.; Meijer, G.; Fielicke, A. Activation of Molecular Oxygen by Anionic Gold Clusters. *Angew. Chemie - Int. Ed.* **2012**, *51* (18), 4444–4447, https://doi.org/10.1002/anie.201108958.

(25) Anderson, M. L.; Ford, M. S.; Derrick, P. J.; Drewello, T.; Woodruff, D. P.; Mackenzie, S. R. Nitric Oxide Decomposition on Small Rhodium Clusters, $Rh_n^{+/-}$. *J. Phys. Chem. A* **2006**, *110*, 10992–11000, https://doi.org/10.1021/JP062178Z.

(26) Tawaraya, Y.; Kudoh, S.; Miyajima, K.; Mafuné, F. Thermal Desorption and Reaction of NO Adsorbed on Rhodium Cluster Ions Studied by Thermal Desorption Spectroscopy. *J. Phys. Chem. A* **2015**, *119* (31), 8461–8468, https://doi.org/10.1021/acs.jpca.5b04224.

(27) Nagata, T.; Koyama, K.; Kudoh, S.; Miyajima, K.; Bakker, J. M.; Mafune, F. Adsorption Forms of NO on Rh_n^+ ($n = 6-16$) Revealed by Infrared Multiple Photon Dissociation Spectroscopy. *J. Phys. Chem. C* **2017**, *121* (49), 27417–27426, https://doi.org/10.1021/acs.jpcc.7b08097.

(28) Mafuné, F.; Tawaraya, Y.; Kudoh, S. Reactivity Control of Rhodium Cluster Ions by Alloying with Tantalum Atoms. *J. Phys. Chem. A* **2016**, *120* (6), 861–867, https://doi.org/10.1021/acs.jpca.5b11898.

Figures

Figure 1.1. (a) Mass spectrum of sodium clusters. Specific numbered clusters, $N = 8$, 20, 40, and 58, were located at the edges of continuous peaks suggesting that they were generated stably. (b) Simulated electronic energy difference, $\Delta(N + 1) - \Delta(N)$, using Woods-Saxon potential. Modified and reprinted figure with permission from Ref[4]. Copyright 1993 by the American Physical Society.
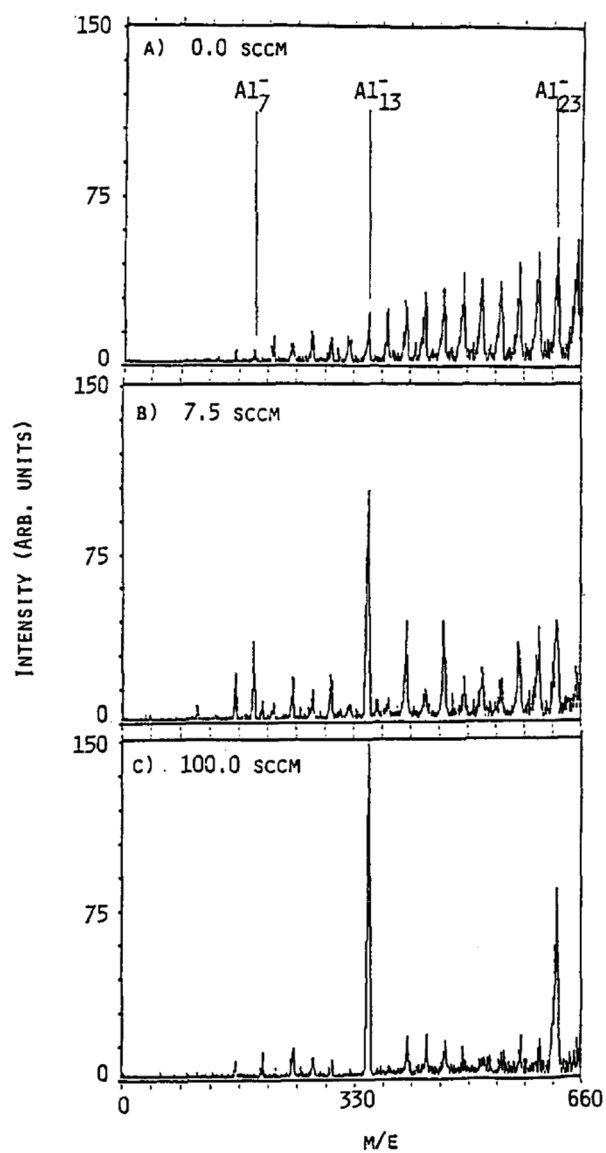
Figure 1.2. (A) The distribution of anionic aluminum clusters. Al_n^- clusters were reacted with oxygen of (B) 7.5 sccm, (c) 100.0 sccm. Al_{13}^- obviously maintains its intensity after reaction. Reprinted from Ref. [5], with the permission of AIP Publishing. Copyright 1989.

12
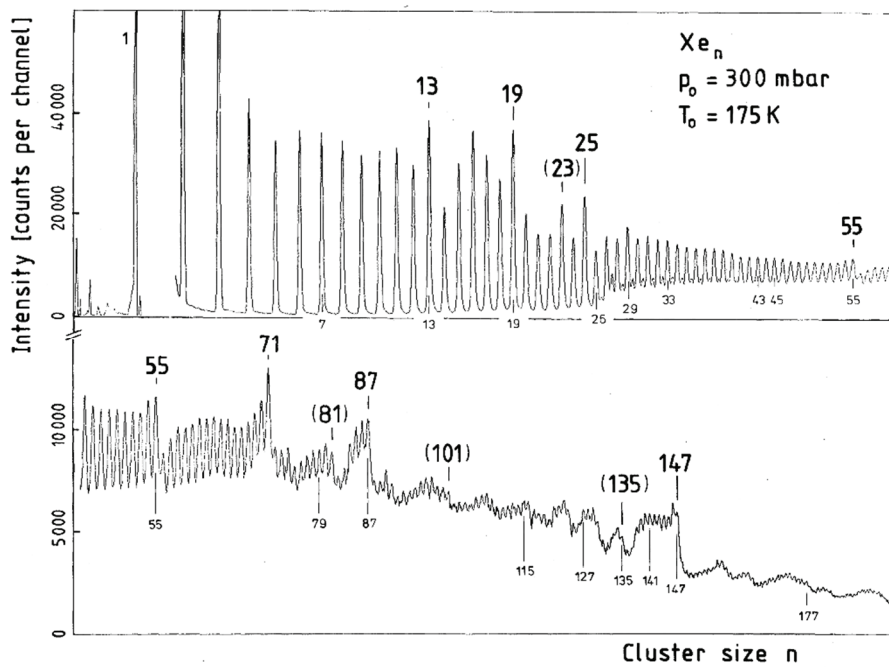
Figure 1.3. Mass spectrum of Xenon clusters. Reprinted figure with permission from Ref [6].Copyright 1981 by the American Physical Society.
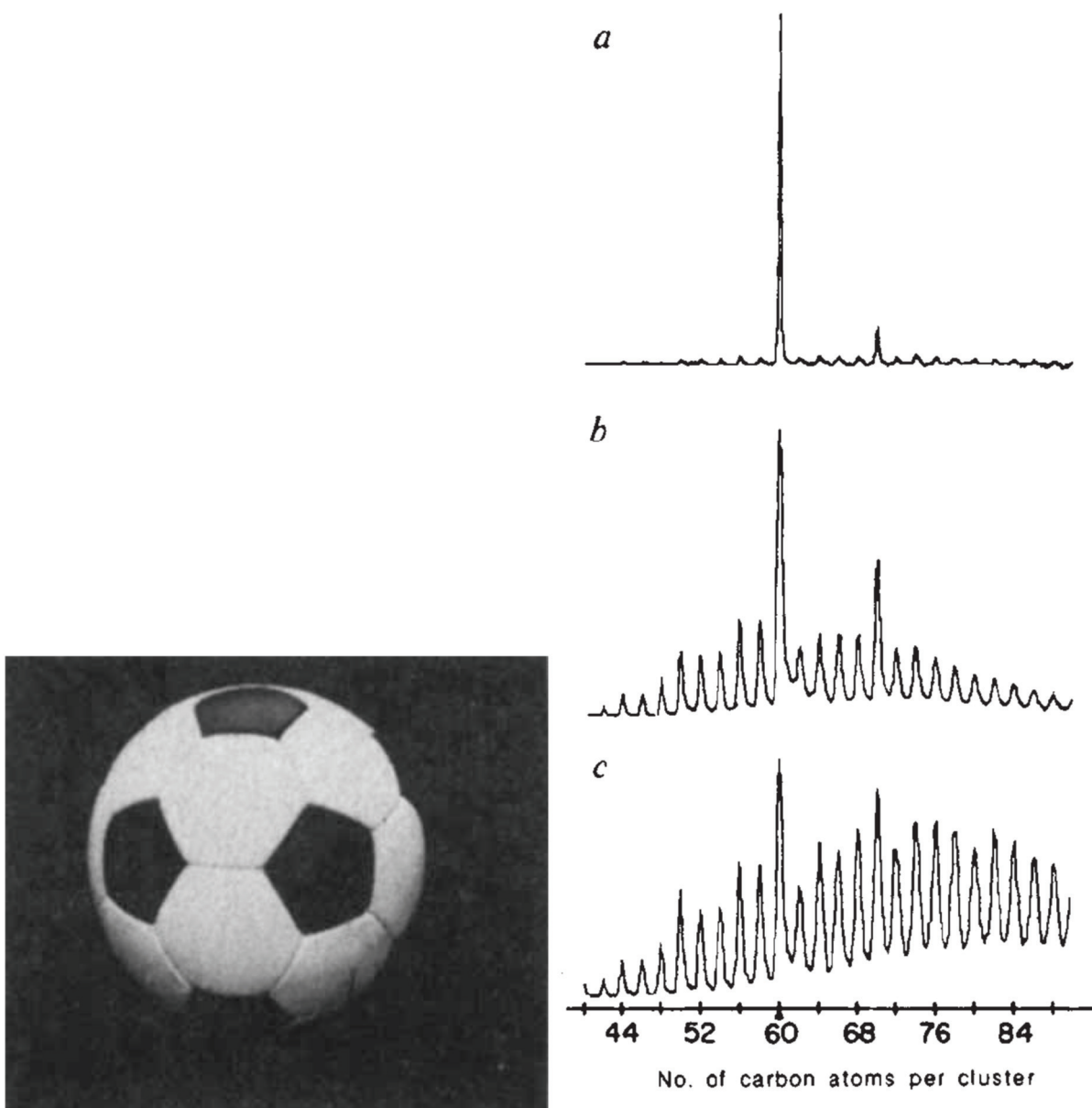
Figure 1.4. The mass spectrum of carbon cluster produced by laser ablation. (c) is the low He pressure condition around 10 torr where (b) is under 760 torr. (a) is the maximized condition to make C_{60}, showing almost only C_{60} and C_{70}. Reprinted by permission from Springer Nature, Ref.[7], Copyright 1985.

Chapter 2

Desorption Energy of Oxygen Molecule from Anionic Gold Oxide Clusters, Au$_n$O$_2^-$, Using Thermal Desorption Spectrometry

We determined the desorption energies of O$_2$ molecules from Au$_n$O$_2^-$ (n = 2, 4, 6, 8, 10, 12, and 14) by gas phase thermal desorption spectrometry. Cluster anions, Au$_n$O$_2^-$, prepared in the gas phase were heated inside a temperature-controlled copper tube. Formation of Au$_n^-$ from the desorption of O$_2$ was observed as a function of temperature. Temperature dependence of the intensities of Au$_n$O$_2^-$ and Au$_n^-$ was analyzed using the Arrhenius equation, estimating the desorption energy of O$_2$ from Au$_n$O$_2^-$. Considering the geometrical structure of Au$_n$O$_2^-$, the desorption energy must be the same as or slightly higher than the binding energy of O$_2$ to Au$_n^-$, because the desorption of O$_2$ proceeds by a simple bond cleavage of Au$_n^-$−O$_2$, without significant rearrangement of atoms in the cluster. The collision-induced dissociation experiments show that the desorption energy was nearly equal to or slightly lower than the threshold energy for n = 2, 4, and 6.

2.1. Introduction

In contrast to the chemical inertness of bulk gold, Haruta et al. showed that gold clusters exhibit catalytic reactivity for low-temperature CO oxidation in the presence of oxygen.[1] Activation of O_2 by gold clusters should be investigated in order to fully understand this remarkable chemical reactivity. Therefore, the interaction between gold clusters and O_2 has been investigated for more than two decades through experiments and theoretical calculations.[2–18]

Cox et al. were the first to report experimental work on the chemical reactions of neutral, cationic, and anionic gas-phase Au_n clusters with O_2.[19] They showed that the reactivity is strongly dependent on the size and charge-state of the clusters: Anion clusters with an even n are reactive toward O_2 and form $Au_nO_2^-$, whilst other clusters, including neutral and cationic, are not reactive, except for Au_{10}^+. Whetten and coworkers investigated the adsorption-desorption equilibria of O_2 on Au_n^- using pulsed flow-reactor methods at ambient temperature.[3] They showed a strong correlation between electron affinity and O_2 adsorption reactivity and that O_2 is bound to Au_n^- as a one-electron acceptor.

Photoelectron spectroscopy is a powerful method to investigate the geometrical and electronic structures of anionic gas-phase clusters.[2,11–15] Ganteför and coworkers showed that, for $Au_nO_2^-$ ($n = 2$, 4, or 6), O_2 molecules are chemisorbed nondissociatively on Au_n^-. They also showed that the stabilization of activated $Au_nO_2^-$ is the key for characteristic activities of Au-based catalysts.[2] More recently, Wang and coworkers showed transition of adsorption forms of O_2 on Au_n^- from the terminal configuration to the bridge configuration, corresponding to superoxo and peroxo chemisorption, respectively.[15]

The geometrical structures were more directly investigated by infrared multiphoton desorption spectroscopy using a free electron laser (FELIX).[16] Fielicke and coworkers observed the vibrational spectra of $Au_nO_2^-$ ($n = 4$, 6, 8, 10, 12, 14, 18, and 20). They showed that $Au_8O_2^-$ comprises multiple isomers using density functional theory (DFT) calculations.

One of the key parameters that characterize the activation of O_2 in $Au_nO_2^-$ is the binding energy of O_2 to Au_n^-. Several values have been suggested based on computational calculations:[4–6,17,18] Metiu and coworkers used DFT to examine the binding of O_2 to Au_n^-, confirming that O_2 binds more strongly to the clusters with an even n than those with an odd n.[17] The binding energies obtained by using the PW91 functional were 0.50 eV for $n = 1$, 1.40 eV for $n = 2$, 0.37 eV for $n = 3$, 1.19 eV for $n = 4$, and 0.76 eV for $n = 5$. In addition, the binding

energy for the second O_2 was obtained to be about 0.71 eV for $n = 2$, for instance, although no experiments proved the formation of $Au_n(O_2)_2^-$.[3,7,11] Later, it was suggested that the values obtained using the PW91 functional could systematically overestimate the binding energies by 0.2−0.4 eV.[18] More recently, Huang and coworkers calculated the binding energies by using B3LYP,[5] whereas Kim and coworkers calculated them by using MP2.[6] However, the values were distributed in a wide energy range. Although these computational calculations have been successfully used to determine geometrical structures and electronic properties, the binding energy is still an issue that needs to be investigated further.

The fundamental problem is the insufficiency of the energy values that have been determined by experiments so far. Whetten and coworkers estimated "relative" energies of the adsorption of O_2 onto Au_n^- from the adsorption-desorption equilibria.[3] It was relative, because the partial pressure of O_2 in the beam was hardly determined in the experiments. Ervin and coworkers obtained threshold energies for the release of O_2 from $Au_nO_2^-$ by collision-induced dissociation (CID) experiments.[7] The threshold energies estimated from the collision energy dependence were, 1.01, 0.91, and 0.81 eV for $n = 2$, 4, and 6, respectively. The threshold energy is regarded as the upper bound for the binding energy. More recently, Bernhardt and coworkers estimated the binding energy of O_2 to Au_2^- from the temperature-dependent kinetic data.[20] The energies obtained by employing the Rice-Ramsperger-Kassel-Marcus (RRKM) theory for both tight and loose transition states were 0.60±0.10 eV and 0.93±0.10 eV, respectively, for Au_2^-.

In the present study, we determined the desorption energy of O_2 from $Au_nO_2^-$ ($n = 2$, 4, 6, 8, 10, 12, and 14).[20–23] Considering the geometrical structure of $Au_nO_2^-$,[16] the desorption energy must be nearly equal to the binding energy, as discussed later. Cluster anions, $Au_nO_2^-$, prepared in the gas phase, were heated inside a temperature-controlled copper tube. Formation of Au_n^- resulting from the desorption of O_2 was observed as a function of temperature. The temperature dependence of the intensities of $Au_nO_2^-$ and Au_n^- was analyzed using the Arrhenius equation, and the desorption energy of O_2 from $Au_nO_2^-$ was estimated.[20–23] The desorption energies were found to be nearly equal to or slightly lower than the threshold energies obtained by CID experiments.[7]

2.2. Experimental Section

The desorption energies of an oxygen molecule from gas-phase anionic gold oxide clusters, $Au_nO_2^-$, were obtained using mass spectrometry in combination with thermal

desorption spectrometry (TDS).[20–23] The $Au_nO_2^-$ clusters were prepared using pulsed laser ablation inside a cluster source. A Au metal rod was vaporized using the focused second harmonic of the Nd:YAG pulsed laser. The cluster ions were formed in a He gas flow containing O_2 from a pulsed valve at a stagnation pressure of 0.8 MPa. The partial pressure of O_2 in the valve was finely tuned between 0.1% and 1% using mass flow and pressure controllers.

The prepared $Au_nO_2^-$ clusters were introduced into an extension tube before expansion into a vacuum chamber (see Figure 2.1). The copper extension tube was 110 mm long and 6 mm in inner diameter and it was heated to $300-1000$ K using a resistive heater; the temperature was monitored using multiple thermocouples installed at different places. The residence time of the cluster ions and the density of the He gas in the tube were estimated to be ~100 μs and ~10^{18} molecules cm^{-3}, respectively. Hence, the clusters were considered to achieve thermal equilibrium by collisions with the He carrier gas prior to expansion into the vacuum. The temperature of the tube was elevated or lowered carefully at a rate of 2 K min^{-1}. The intensities of the cluster ions were monitored as a function of temperature using mass spectrometry, and the TDS plot was obtained.

After expansion into the vacuum, the cluster ions were accelerated by a pulsed electric field to gain a kinetic energy of 3.5 keV for mass analysis with a time-of-flight spectrometer. The ions were detected using a Hamamatsu double-microchannel plate detector after passing through a 1-m field-free flight tube. The signals were amplified with a preamplifier and were digitized using an oscilloscope. The mass resolution was sufficiently high (>1000 at $m / z = 1000$) to distinguish Au and O atoms in the mass spectra.

2.3. Results and Discussion

Figure 2.2 shows the mass spectra of the anionic clusters thus produced and then passed through the extension tube heated at the indicated temperatures. Ions assignable to Au_n^- and $Au_nO_2^-$ ($n = 6-10$) are seen in the mass spectra. Even numbered Au_n^- adsorbed an oxygen molecule forming $Au_nO_2^-$, whereas odd numbered Au_n^- did not adsorb O_2, which is consistent with previously reported results: As a Au atom possesses an odd number of electrons, even numbered Au_n^- possesses the odd number of electrons. The O_2 molecule accepted one electron from Au_n^- upon adsorption, and hence, $Au_nO_2^-$ was stably formed. In the present experimental condition, $Au_6O_2^-$ was dominantly formed and the parent Au_6^- completely disappeared from the mass spectra at 300 K, showing that sufficient amount of the O_2 molecules were supplied

in the reaction region. Nevertheless, no formation of $Au_6O_4^-$ was observed, probably because the second O_2 molecule was so weakly bound to $Au_6O_2^-$ that the O_2 desorbed from it in the extension tube in a thermal equilibrium at 300 K, and/or the activation barrier for the adsorption of the second O_2 was too high for the O_2 to adsorb on $Au_6O_2^-$.[7]

When the clusters were heated in the extension tube, the mass spectrum changed, as shown in Figure 2.2: $Au_6O_2^-$, which formed dominantly at 300 K, showed reduced intensity at 500 K; instead, Au_6^- appeared in the same extent. Following this, the intensity of Au_6^- dominated at 600 K and $Au_6O_2^-$ mostly disappeared. The intensity distribution of the ions after heating was obtained from the mass spectra by integrating each peak area (Figure 2.3). Note that the intensities of the clusters reduced by heating, regardless of the size and stoichiometry, because the bunch of the cluster ions in the beam expanded spatially with respect to the probing volume for the mass spectrometry. The intensities of the clusters were plotted after normalization, assuming that the total intensity of the clusters was unity for each n, and TDS curves were obtained. The concomitant changes of the intensities of $Au_nO_2^-$ and Au_n^- are considered to be caused by the desorption of the O_2 molecule from the cluster, as shown below

$$Au_nO_2^- \rightarrow Au_n^- + O_2. \tag{2.1}$$

The temperature at which the desorption of the O_2 molecule occurs is dependent on the cluster size, n. For instance, the intensity of $Au_4O_2^-$ becomes half at 500 K, whereas the intensity of $Au_8O_2^-$ becomes half at 420 K, suggesting that O_2 in $Au_8O_2^-$ is more weakly bound than in $Au_4O_2^-$.

In our experimental setup, $Au_nO_2^-$ is considered to dissociate unimolecularly in the extension tube. Hence, the intensity of $Au_nO_2^-$, $I(T)$, decreases exponentially with the reaction time, t, as

$$\frac{I(T)}{I_0} = \exp(-k(T)t), \tag{2.2}$$

where T, I_0, and $k(T)$ refer to the temperature, intensity of $Au_nO_2^-$ before entering the extension tube, and pseudo-first order rate constant for unimolecular dissociation, respectively. In addition, the rate constant is expressed by the Arrhenius equation as

$$k(T) = A\exp(-\frac{\Delta E}{k_B T}) \tag{2.3}$$

where A, ΔE, and k_B refer to the pre-exponential factor, desorption energy, and Boltzmann constant, respectively. Combining eq. (2.2) and (2.3), we obtain the following equation

$$\frac{I(T)}{I_0} = \exp(-At\exp(-\frac{\Delta E}{k_B T})) \tag{2.4}$$

The desorption energies, ΔE, were obtained by fitting the experimental TDS curves with eq. (2.4), in which At and ΔE were set as variable parameters. Here, the reaction time, t, is about 100 μs, estimated from the speed of the beam and the length of the tube, though this value was not used for the analysis of ΔE. The fittings well reproduced the experimental data; the desorption energies thus obtained are plotted in Figure 2.4 and listed in Table 2.1. The error in the energy was the standard deviation, σ, of the estimated energies for different runs. The desorption energy is highest at $n = 2$ and ranges around 0.5 eV for $n \geq 4$, indicating that O_2 very weakly chemisorbed on Au_n^-.

Desorption of the O_2 molecule from $Au_nO_2^-$ is endothermic, and the endothermicity equals to the binding energy or the bond dissociation energy of $Au_n^- - O_2$; the difference in the formation energy between $Au_nO_2^-$ and $Au_n^- + O_2$ (see Scheme 2.1). The desorption energy can be higher than the binding energy if the desorption requires geometrical rearrangement of the atoms in a cluster. The geometrical structures of $Au_nO_2^-$, determined by photoelectron spectroscopy[2,11,15] and IRMPD spectroscopy,[16] suggest that the desorption of O_2 does not require significant geometrical rearrangement of atoms, as the molecular O_2 attaches to the terminal site for $n = 2, 4, 6$, and 8 and the bridge site for $n = 8, 10$, and 12. Note that two or three isomers are known for $n = 8$.[15,16] Hence, the binding energy of O_2 to Au_n^- is considered to nearly equal to the desorption energy. In the RRKM theory employed by Bernhardt and coworkers for $Au_2O_2^-$, the present system can be analyzed by using the loose transition state, as the desorption of O_2 from $Au_2O_2^-$ was caused by simple bond cleavage.[10] The binding energy for it has been calculated to be 0.93 ± 0.10 eV, agreeing well within the error limits.

Ervin et al. carried out the CID of $Au_nO_2^-$ and obtained the energy as 1.01, 0.91, and 0.81 eV for $n = 2, 4$ and 6, respectively.[7] The CID experiment gives the upper bounds for the binding energy of $Au_n^- - O_2$ and the values for $n = 4$ and 6 are larger than the desorption energies obtained here. The difference in energy is small for $n = 2$, as the vibrational degree of freedom of the cluster is limited. Upon collision in CID, the energy gained by the cluster is to be distributed in the internal modes in the cluster and then redistributed in time. When the energy relating to the internal mode leading to dissociation exceeds the desorption energy, the cluster

dissociates into fragments. Hence, the increase in the vibrational degree of freedom, resulting from the increase in size, n, would widen the gap between the threshold energy by CID and the desorption energy by TDS.

In summary, we obtained the desorption energies of O_2 from $Au_nO_2^-$ simply by gas-phase TDS, assuming that the pseudo-first-order rate constant changes with temperature according to the Arrhenius equation. The desorption energy is highest at $n = 2$ and ranges around 0.5 eV for $n \geq 4$, indicating that O_2 very weakly chemisorbed on Au_n^-. The desorption energy must be the same as, or very slightly higher than the binding energy, as the desorption of O_2 proceeds by a simple bond cleavage of $Au_n^--O_2$ without significant rearrangement of atoms in the cluster. The binding energies obtained by computational calculations agree rather well with the experimental data for $n = 2$. However, the calculations most likely overestimate the binding energy for larger Au_n^- ($n \geq 4$).

2.4. References

(1)   Haruta, M. Size- and Support-Dependency in the Catalysis of Gold. *Catal. Today* **1997**, *36* (1), 153–166, https://doi.org/10.1016/S0920-5861(96)00208-8.

(2)   Stolcic, D.; Fischer, M.; Ganteför, G.; Kim, Y. D.; Sun, Q.; Jena, P. Direct Observation of Key Reaction Intermediates on Gold Clusters. *J. Am. Chem. Soc.* **2003**, *125* (10), 2848–2849, https://doi.org/10.1021/ja0293406.

(3)   Salisbury, B. E.; Wallace, W. T.; Whetten, R. L. Low-Temperature Activation of Molecular Oxygen by Gold Clusters: A Stoichometric Process Correlated to Electron Affinity. *Chem. Phys.* **2000**, *262* (1), 131–141, https://doi.org/10.1016/S0301-0104(00)00272-X.

(4)   Okumura, M.; Kitagawa, Y.; Haruta, M.; Yamaguchi, K. DFT Studies of Interaction between O_2 and Au Clusters. The Role of Anionic Surface Au Atoms on Au Clusters for Catalyzed Oxygenation. *Chem. Phys. Lett.* **2001**, *346* (1–2), 163–168, https://doi.org/10.1016/S0009-2614(01)00957-5.

(5)   Liao, M.-S.; Watts, J. D.; Huang, M.-J. Theoretical Comparative Study of Oxygen Adsorption on Neutral and Anionic Ag_n and Au_n Clusters ($n = 2$–25). *J. Phys. Chem. C* **2014**, *118* (38), 21911–21927, https://doi.org/10.1021/jp501701f.

(6)   Lee, H. M.; Lee, K. H.; Lee, G.; Kim, K. S. Geometrical and Electronic Characteristics of $Au_nO_2^-$ ($n = 2-7$). *J. Phys. Chem. C* **2015**, *119* (25), 14383–14391, https://doi.org/10.1021/acs.jpcc.5b03051.

(7)   Wallace, W. T.; Leavitt, A. J.; Whetten, R. L. Comment on: The Adsorption of Molecular Oxygen on Neutral and Negative Au_N Clusters ($N = 2$-5) [Chem. Phys. Lett. 359 (2002) 493]. *Chem. Phys. Lett.* **2003**, *368* (5–6), 774–777, https://doi.org/10.1016/S0009-2614(02)01961-9.

(8)   Ding, X.; Li, Z.; Yang, J.; Hou, J. G.; Zhu, Q. Adsorption Energies of Molecular Oxygen on Au Clusters. *J. Chem. Phys.* **2004**, *120* (20), 9594–9600, https://doi.org/10.1063/1.1665323.

(9)   Wallace, W. T.; Wyrwas, R. B.; Whetten, R. L.; Mitrić, R.; Bonačić-Koutecký, V. Oxygen Adsorption on Hydrated Gold Cluster Anions: Experiment and Theory. *J. Am. Chem. Soc.* **2003**, *125*, 8408–8414, https://doi.org/10.1021/JA034905Z.

(10)   Bernhardt, T. M.; Hagen, J.; Lang, S. M.; Popolan, D. M.; Socaciu-Siebert, L. D.; Wöste, L. Binding Energies of O_2 and CO to Small Gold, Silver, and Binary Silver-Gold Cluster Anions from Temperature Dependent Reaction Kinetics Measurements. *J. Phys. Chem. A* **2009**, *113* (12), 2724–2733, https://doi.org/10.1021/jp810055q.

(11)   Häkkinen, H.; Yoon, B.; Landman, U.; Li, X.; Zhai, H.-J.; Wang, L.-S. On the Electronic and Atomic Structures of Small Au_N^- ($N = 4-14$) Clusters: A Photoelectron Spectroscopy and Density-Functional Study. *J. Phys. Chem. A* **2003**, *107*, 6168–6175, https://doi.org/10.1021/JP035437I.

(12)   Yoon, B.; Häkkinen, H.; Landman, U. Interaction of O_2 with Gold Clusters: Molecular and Dissociative Adsorption. *J. Phys. Chem. A* **2003**, *107*, 4066–4071, https://doi.org/10.1021/JP027596S.

(13)   Sun, Q.; Jena, P.; Kim, Y. D.; Fischer, M.; Ganteför, G. Interactions of Au Cluster Anions with Oxygen. *J. Chem. Phys.* **2004**, *120* (14), 6510–6515, https://doi.org/10.1063/1.1666009.

(14)   Huang, W.; Zhai, H.-J.; Wang, L.-S. Probing the Interactions of O_2 with Small Gold Cluster Anions (Au_n^-, $n = 1-7$): Chemisorption vs Physisorption. *J. Am. Chem. Soc.* **2010**, *132* (12), 4344–4351, https://doi.org/10.1021/ja910401x.

(15)   Pal, R.; Wang, L.-M.; Pei, Y.; Wang, L.-S.; Zeng, X. C. Unraveling the Mechanisms of O2 Activation by Size-Selected Gold Clusters: Transition from Superoxo to Peroxo

Chemisorption. *J. Am. Chem. Soc.* **2012**, *134* (22), 9438–9445, https://doi.org/10.1021/ja302902p.

(16) Woodham, A. P.; Meijer, G.; Fielicke, A. Activation of Molecular Oxygen by Anionic Gold Clusters. *Angew. Chemie - Int. Ed.* **2012**, *51* (18), 4444–4447, https://doi.org/10.1002/anie.201108958.

(17) Mills, G.; Gordon, M. S.; Metiu, H. The Adsorption of Molecular Oxygen on Neutral and Negative Au_n Clusters ($n = 2-5$). *Chem. Phys. Lett.* **2002**, *359* (5–6), 493–499, https://doi.org/10.1016/S0009-2614(02)00746-7.

(18) Varganov, S. A.; Olson, R. M.; Gordon, M. S.; Metiu, H. The Interaction of Oxygen with Small Gold Clusters. *J. Chem. Phys.* **2003**, *119* (5), 2531–2537, https://doi.org/10.1063/1.1587115.

(19) Cox, D. M.; Brickman, R.; Creegan, K.; Kaldor, A. Gold Clusters: Reactions and Deuterium Uptake. *Zeitschrift für Phys. D Atoms, Mol. Clust.* **1991**, *19* (1–4), 353–355, https://doi.org/10.1007/BF01448327.

(20) Mafuné, F.; Takenouchi, M.; Miyajima, K.; Kudoh, S. Rhodium Oxide Cluster Ions Studied by Thermal Desorption Spectrometry. *J. Phys. Chem. A* **2016**, *120* (3), 356–363, https://doi.org/10.1021/acs.jpca.5b09531.

(21) Nagata, T.; Miyajima, K.; Mafuné, F. Stable Stoichiometry of Gas-Phase Cerium Oxide Cluster Ions and Their Reactions with CO. *J. Phys. Chem. A* **2015**, *119* (10), 1813–1819, https://doi.org/10.1021/jp509592a.

(22) Nagata, T.; Miyajima, K.; Mafuné, F. Oxidation of Nitric Oxide on Gas-Phase Cerium Oxide Clusters via Reactant Adsorption and Product Desorption Processes. *J. Phys. Chem. A* **2015**, *119* (41), 10255–10263, https://doi.org/10.1021/acs.jpca.5b07749.

(23) Koyama, K.; Kudoh, S.; Miyajima, K.; Mafuné, F. Dissociation Energy for O_2 Release from Gas-Phase Iron Oxide Clusters Measured by Temperature-Programmed Desorption Experiments. *Chem. Phys. Lett.* **2015**, *625*, 104–109, https://doi.org/10.1016/j.cplett.2015.02.038.

Figures

Figure 2.1. Schematic diagram of the experimental apparatus used in the present study. Both the cluster source and the extension tube for heating the clusters are illustrated.
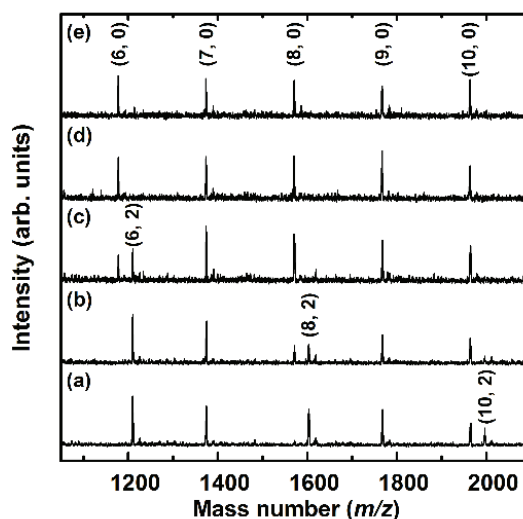
Figure 2.2. Expanded mass spectra of Au_n^- and $Au_nO_2^-$ produced by laser ablation of a Au rod in a gas mixture of He and O_2. Ion peaks are labeled as $(n, 0)$ and $(n, 2)$ for Au_n^- and $Au_nO_2^-$, respectively. The temperature of the tube was set at (a) 300 K, (b) 400 K, (c) 500 K, (d) 600 K, and (e) 650 K.
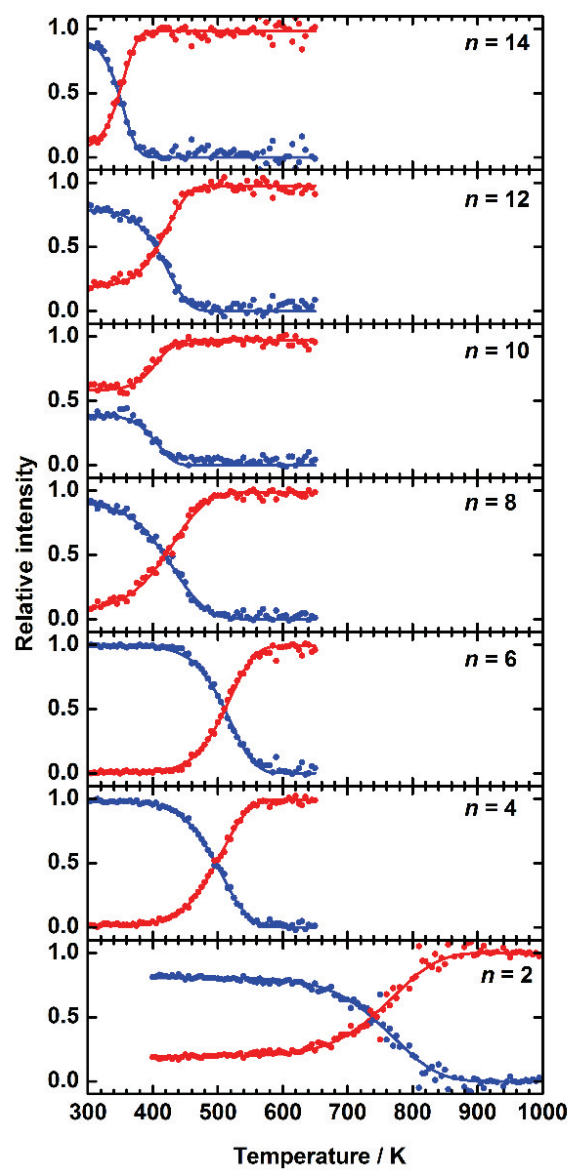
Figure 2.3. TDS plots for Au$_n$O$_2^-$ (n = 2, 4, 6, 8, 10, 12, and 14).
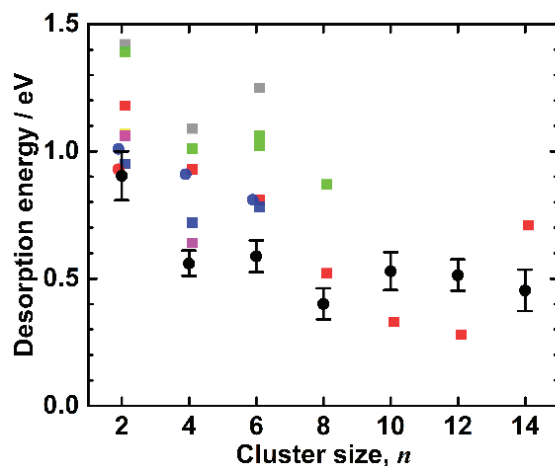
Figure 2.4. Desorption energy of O_2 molecule from $Au_nO_2^-$ estimated from the TDS curve (black solid circle). The error shown as an error bar was the standard deviation, σ, of the energy for different runs. Threshold energy obtained by the CID experiment (blue solid circle) and binding energy obtained by adsorption and desorption kinetic data (red solid circle) are shown. The binding energies obtained by the computational calculations are also shown (square marks). See references in Table 2.1.

Scheme 2.1.
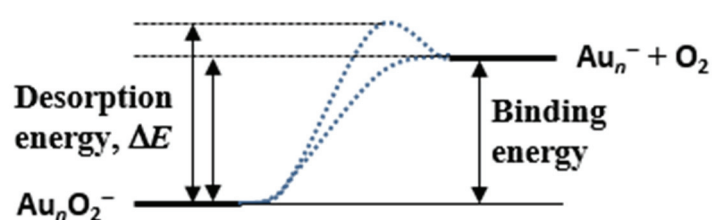
Table 2.1.

Desorption Energies of O_2 from $Au_nO_2^-$ in eV estimated from TDS experiments.

Cluster size, n	ΔE (eV)	Energy (eV)[a]	Energy (eV)[b]
2	0.90±0.10	0.93[c], 1.01[d]	0.95[e], 1.06[f], 1.07[g], 1.18[h], 1.39[i], 1.42[j]
4	0.56±0.05	0.91[d]	0.64[f], 0.72[e], 0.93[h], 1.01[i], 1.09[j]
6	0.59±0.06	0.81[d]	0.78[e], 0.81[h], 1.02[i], 1.06[i], 1.25[j]
8	0.40±0.06		0.52[h], 0.87[i]
10	0.53±0.07		0.33[h]
12	0.51±0.06		0.28[h]
14	0.45±0.08		0.71[h]

[a] Energy obtained by experiments. [b] Energy obtained by computational calculations. [c] Binding energy. Ref. 10. [d] Threshold energy of CID. Ref. 7. [e] Ref. 8. [f] Ref. 9. [g] Ref. 18. [h] Ref. 5. [i] Ref. 12. [j] Ref. 6.

Table 2.2.

A pre-exponential factor of the Arrhenius equation, A (s^{-1}), for O_2 desorption from $Au_nO_2^-$ estimated from TDS experiments by setting the reaction time in the extension tube, t, to 100 μs.

Cluster size, n	$\log_{10}A$
2	13.8±0.6
4	13.6±0.5
6	13.8±0.6
8	12.6±0.7
10	14.5±0.9
12	14.1±0.7
14	14.1±1.1

Chapter 3

Isomers of Anionic Gold Oxide Clusters, $Au_nO_2^-$, Investigated by Thermal Desorption Spectrometry

Anionic gold oxide clusters, $Au_nO_2^-$ ($n = 2-5$), were prepared by sequential O atom transfer reactions from N_2O to Au_n^-. Response of the clusters to heat was investigated by gas phase thermal desorption spectrometry and compared with the behavior of $Au_nO_2^-$ prepared by the reaction of Au_n^- with O_2. No desorption of O_2 was observed from $Au_4O_2^-$ prepared with N_2O until 1000 K, but O_2 desorbed from $Au_4O_2^-$ prepared with O_2 at 500 K, indicating the formation of structural isomers. Theoretical calculations show that the most stable form of $Au_4O_2^-$, which contains dissociated O atoms, is produced by oxidation with N_2O and that the third most stable form of $Au_4O_2^-$, which contains molecular O_2, is produced by oxidation with O_2. The desorption energy of O_2 from $Au_5O_2^-$, in which O_2 is dissociatively chemisorbed on Au_5^-, was estimated from the temperature dependence of the cluster signal intensities. The experimentally determined desorption energies were consistent with the values obtained by theoretical calculation.

3.1. Introduction

Gold clusters are known to exhibit catalytic activity for CO oxidation in the presence of oxygen at low temperature.[1] Oxygen activation by the clusters is key to this process. The interaction between gold clusters and oxygen has been investigated experimentally and theoretically for more than two decades. Cox and coworkers first elucidated the chemical reactions of neutral, cationic, and anionic Au_n clusters with O_2.[2] Reactivity is strongly dependent on the size and charge state. Anionic clusters with an even value of n are reactive toward O_2 and form $Au_nO_2^-$, whereas neutral and cationic clusters except Au_{10}^+ are not reactive. The structures of $Au_nO_2^-$ moieties with even n have been investigated by infrared multiple photon desorption spectroscopy using free electron laser (FELIX).[3] Fielicke and coworkers obtained the vibrational spectra of $Au_nO_2^-$ (n = 4, 6, 8, 10, 12, 14, 18, and 20) and concluded on the basis of density functional theory (DFT) calculations that O_2 is adsorbed molecularly on Au_n^-. For $Au_nO_2^-$ with odd n, Wang and coworkers prepared $Au_5O_2^-$ and $Au_7O_2^-$ in a molecular beam and determined from photoelectron spectroscopy that O_2 is weakly physisorbed on Au_5^- and Au_7^-.[4] These spectroscopic findings are consistent with the pioneering work of Cox and coworkers.[2]

Although O_2 molecularly adsorbed on Au_n^- has been investigated extensively, theoretical calculations suggest that O_2 dissociatively adsorbed on $Au_4O_2^-$ is the most stable structure.[5] $Au_nO_2^-$ with molecularly adsorbed O_2 is found in all cases except $Au_3O_2^-$, in which the clusters are prepared by reaction of Au_n^- with O_2, owing to the energy barrier between molecularly and dissociatively adsorbed forms. We seek to learn if the most stable $Au_nO_2^-$ isomer with dissociatively adsorbed O_2 can be found experimentally. Wang and coworkers produced $Au_3O_2^-$ using N_2O as an oxidant, which supplies oxygen atom by atom.[4] $Au_3O_2^-$ with dissociatively adsorbed O_2 was also formed using O_2 as oxidant. We explored the formation of stable isomers of $Au_nO_2^-$ ($n \geq 2$) using N_2O as the oxidant and examined them by thermal desorption spectrometry (TDS). Key parameters in the activation of O_2 in $Au_nO_2^-$ clusters are its binding and desorption energies. We previously determined the energy of O_2 desorption from $Au_nO_2^-$ (n = 2, 4, 6, 8, 10, 12, and 14) prepared by reaction of Au_n^- with O_2.[6] The $Au_nO_2^-$ cluster anions were heated inside a temperature-controlled copper tube, and the Au_n^- produced by desorption of O_2 was observed as a function of temperature. The temperature dependence of the $Au_nO_2^-$ and Au_n^- intensities was analyzed using the Arrhenius equation to estimate the energy of O_2 desorption from $Au_nO_2^-$.[7–10]

In this study, we prepared $Au_nO_m^-$ (m = 0, 1, 2, 3, ...) clusters by collisional O-atom transfer between Au_n^- and N_2O. The interaction of oxygen with Au_n^- was investigated by gas-phase TDS. Comparison of the TDS curves of $Au_nO_m^-$ prepared using N_2O as oxidant with those using O_2 as oxidant reveal totally different thermal responses. The experimental results are discussed in light of accompanying theoretical calculations.

3.2. Experimental Section

Gas-phase anionic gold oxide clusters, $Au_nO_2^-$ (n = 1, 2, 3, ...), were prepared by reaction of Au_n^- with N_2O and characterized using mass spectrometry in combination with thermal desorption spectrometry.[7–10] The Au_n^- clusters were generated using pulsed laser ablation inside a cluster source. A gold metal rod was vaporized by the focused second harmonic of a Nd:YAG pulsed laser. The cluster ions were produced in a He atmosphere with N_2O gas as oxidant from a pulsed valve at a stagnation pressure of 0.8 MPa. The N_2O concentration in the valve was carefully adjusted between 0 and 1.4% using mass flow and pressure controllers.

The $Au_nO_2^-$ clusters were introduced into a copper extension tube before mass analysis. The 120-mm long by 6-mm inner diameter tube was heated to 300–1000 K using a resistive heater. The temperature inside the tube was monitored with a thermocouple. The residence time of the cluster ions and the density of He gas in the tube were estimated to be ~100 μs and ~10^{18} molecules cm^{-3}, respectively. The clusters were considered to achieve thermal equilibrium by collisions with the He carrier gas. The temperature of the tube was raised or lowered at a rate of 5 K min^{-1} using an electric feedback circuit. The cluster ion intensities were measured as a function of temperature using mass spectrometry to obtain the TDS curves.

After exiting the extension tube, the cluster ions were accelerated by a pulsed electric field to a kinetic energy of 3.5 keV for mass analysis with a time-of-flight spectrometer. After passing through a 1-m field-free flight tube, the ions were detected with a Hamamatsu double-microchannel plate detector. Signals were amplified with a preamplifier and digitized using an oscilloscope. The mass resolution was sufficiently high (>1000 at m / z = 1000) to distinguish Au and O atoms in the mass spectra.

31

3.3. Computational Section

To determine the stable geometries of Au_n^- and $Au_nO_2^-$, quantum chemical calculations were performed using Gaussian 09.[11] Calculations of gold oxide clusters using density functional theory (DFT) have been performed by a number of researchers.[5,12–20] Becke's three-parameter hybrid density functional with the Lee-Yang-Parr correlation functional (B3LYP) provides reasonable binding energies for many clusters with a small calculation cost. According to the calculation of electron density differences by Metiu *et al.*, it is thought that electron transfer occurs upon adsorption of O_2 onto gold clusters.[14] As shown by the recent work of Kim and coworkers,[5] the second order Moller-Plesset method (MP2) describes electron transfer well, and we have therefore adopted this method. The MWB60 effective core potential (ECP) and basis set were used to describe the Au atoms, whereas the 6-311+G(d) basis set was used for O.

The reported stable geometries of $Au_n^{0/+/-}$ obtained by B3LYP calculations were used for the initial Au_n^- geometries and were re-optimized using MP2.[20] All stable geometries were planar for $n = 3–5$. Initial $Au_nO_2^-$ geometries were established by randomly placing O atoms in the Au_n^- plane. To assure completeness of calculation, DFT calculations of $Au_nO_2^-$ were also performed using B3LYP, and the resulting structures were re-optimized at the MP2 level. Basis set superposition error (BSSE) corrections were not used. All calculations were performed for the first and second lowest spin multiplicities.

3.4. Results and Discussion

3.4.1. Formation of Anionic Gold Oxide Clusters by Reaction with N_2O

Anionic gold oxide clusters, $Au_nO_m^-$ ($n = 1–12$; $m = 0, 1, 2, …$), were produced by reaction of Au_n^- with N_2O. Figure 3.1 shows typical mass spectra of the anionic clusters at different N_2O concentrations, in which ions assignable to $Au_nO_m^-$ ($n = 2–9$; $m = 0, 1, 2, …$) are observed. The number of oxygen atoms in $Au_nO_m^-$ appears to increase with increasing N_2O concentration, which indicates that O atoms are transferred sequentially from N_2O to $Au_nO_m^-$ by gas phase collisions in the reaction cell:

$$Au_n^- + N_2O \rightarrow Au_nO^- + N_2 \qquad (3.1)$$

$$Au_nO^- + N_2O \rightarrow Au_nO_2^- + N_2 \qquad (3.2)$$

$$Au_nO_2^- + N_2O \rightarrow Au_nO_3^- + N_2. \qquad (3.3)$$

In addition, trace amounts of adsorbed N_2O species, $Au_nO_m(N_2O)^-$, are observed in the mass spectra. The appearance of $Au_nO_m(N_2O)^-$ suggests formation of $Au_nO_{m+1}^-$ by a mechanism that begins with N_2O attachment to $Au_nO_m^-$, as $Au_nO_m(N_2O)^-$ can be a reaction intermediate. N_2O is considered to bind to $Au_nO_m^-$ through one of its terminal N atom. Thus, the linear N_2O molecule must bend so that the O atom can approach a Au atom to accomplish atom transfer. This distortion will create an energy barrier to the reaction. If the barrier is low and easily crossed, only $Au_nO_m^-$ will be observed, whereas only $Au_nO_m(N_2O)^-$ will be formed if the barrier is high. For $n = 3$, Au_3O^- is produced without forming $Au_3(N_2O)^-$, which suggests that the reaction barrier is low. In contrast, $Au_3O(N_2O)^-$ is formed in addition to $Au_3O_2^-$, which suggests that the barrier is large enough to retain some of the intermediate species before reaction.

Anionic gold oxide clusters, $Au_nO_2^-$, have been produced primarily by reaction of Au_n^- with O_2. Au_n^- clusters with even values of n adsorb an oxygen molecule to form $Au_nO_2^-$, whereas Au_n^- clusters with odd values of n scarcely adsorb O_2. These findings are consistent with previous results.[2] Because a neutral Au atom possesses an odd number of electrons, even-numbered Au_n^- clusters possess an odd number of electrons. By accepting one electron from Au_n^-, an O_2 molecule can form a stable $Au_nO_2^-$ adduct upon adsorption. Spectroscopic studies and DFT calculations of the structure of $Au_nO_2^-$ indicate that O_2 adsorbs in molecular form.[3]

However, $Au_nO_2^-$ clusters with odd values of n have been produced experimentally by reaction of Au_n^- with O_2 and have been characterized by photoelectron spectroscopy.[5] The photoelectron spectra of $Au_5O_2^-$ and $Au_7O_2^-$ are similar to those of Au_5^- and Au_7^-, respectively, which indicates that the interaction between Au_n^- ($n = 5$ and 7) and O_2 is weak. Formation of $Au_nO_2^-$ with odd values of n by reaction of Au_n^- with O_2 at room temperature is hardly favorable. However, $Au_3O_2^-$ has also been produced by reaction with O_2 and with N_2O. In contrast to $Au_5O_2^-$ and $Au_7O_2^-$, $Au_3O_2^-$ containing either two dissociated O atoms or physisorbed molecular O_2 has been suggested as the major and minor structures, respectively.[5]

In the present study, $Au_nO_2^-$ ($n = 1-12$) species have been prepared using N_2O as oxidant. Considering that odd-numbered $Au_nO_2^-$ forms containing molecular O_2 are not electronically stable, it is very likely that the geometry of $Au_nO_2^-$ prepared with N_2O differs from that prepared with O_2. In addition, because N_2O can supply oxygen atoms to Au_n^- sequentially, two O atoms can adsorb on Au_n^- without forming an O–O bond. In other words, structural isomers of $Au_nO_2^-$ are likely to exist depending on the method of preparation.

3.4.2. Thermal Desorption Spectrometry of Anionic Gold Oxide Clusters

Possible structural isomers of $Au_nO_2^-$ ($n = 2-5$) prepared using N_2O were investigated by thermal desorption spectrometry. The mass spectra changed as the clusters produced in this manner were heated in the extension tube. The intensity distribution of the ions after heating was obtained from the integrated peak areas of the mass spectra and was plotted as a function of temperature (Figure 3.2). As shown in panel (d), the intensity of $Au_5O_2^-$ is constant below 700 K and begins to decrease above this temperature. In contrast, the intensity of Au_5^- gradually increases above 700 K. The concomitant change in the $Au_5O_2^-$ and Au_5^- intensities is caused by desorption of O_2 from the cluster as shown

$$Au_5O_2^- \rightarrow Au_5^- + O_2. \tag{3.4}$$

For $n = 4$, the intensities of $Au_4O_m^-$ ($m = 0-4$) do not change over the entire temperature range indicating that these clusters are thermally stable and persist as $Au_4O_m^-$ without fragmentation. The energy of O_2 desorption from $Au_4O_2^-$ is estimated to be > 1.5 eV on the basis of the Arrhenius equation and a pre-exponential factor of $A = 6.1 \times 10^{13}$ s^{-1}, which is the average value obtained in our previous study.[6] In contrast, the intensity of $Au_4O_2^-$ prepared using O_2 as oxidant decreased above 400 K, and the intensity of the Au_4^- signal exhibited a corresponding increase at this temperature.[6] The energy of O_2 desorption from this form of $Au_4O_2^-$ was estimated from the Arrhenius equation to be 0.56 ± 0.05 eV. Thus, the thermal desorption spectrometry response of $Au_4O_2^-$ prepared by reaction of Au_4^- with N_2O differs from that prepared by reaction of Au_4^- with O_2, which indicates the existence of structural isomers.

3.4.3. Structures of $Au_4O_2^-$

Kim and coworkers proposed a geometrical structure of $Au_4O_2^-$ prepared with molecular O_2 and demonstrated that the structure is consistent with the results from photoelectron and IR multiple photon dissociation spectroscopy.[5] As shown in Figure 3.3, one stable isomer has O_2 adsorbed to one arm of a Y-shaped Au_4^- unit. The O_2 binding energy, ΔE_n, defined as

$$\Delta E_n^{\text{mol or diss}} = E(Au_n^-) + E(O_2) - E(Au_nO_2^-) \tag{3.5}$$

was calculated to be $\Delta E_4^{\text{mol}} = 0.66$ eV for $n = 4$ at the MP2 level, where E represents the formation energy of the species in parentheses. We adopted the stable Y-shaped geometry of Au_4^- and assumed that its structure did not change significantly upon release of O_2. The

activation energy for desorption nearly equals the binding energy because O_2 can be released without significant structural deformation. Hence, the calculated value is consistent with the desorption energy estimated in our previous study (0.56 ± 0.05 eV) confirming that $Au_4O_2^-$ prepared from O_2 can be assigned the calculated structure.[6]

Theoretical calculations also suggest that the most stable structure of $Au_4O_2^-$ binds O_2 in its dissociated form (Figure 3.3). The binding energy of the dissociative form, ΔE_4^{diss}, is calculated to be 0.84 eV. The stable rhombus geometry of Au_4^- was used for this calculation. The cluster must deform significantly upon O_2 desorption, because the two separated O atoms must approach one another to form a chemical bond, and the resulting transition state makes the desorption energy greater than the binding energy. The desorption energy of O_2 from $Au_4O_2^-$ is expected to be greater than 1.5 eV on the basis of the Arrhenius equation. Thus, the thermal stability of $Au_4O_2^-$ prepared from N_2O derives from the high energy of this transition state.

According to the DFT calculations using B3LYP, the most stable form of Au_4^- is bent with the rhombus structure being +0.32 eV higher than the bent structure. The most stable form of $Au_4O_2^-$ contains O_2 adsorbed at one arm of Y-shaped Au_4^-. The binding energy of O_2 to Au_4^- is calculated to be $\Delta E_4^{mol} = 0.80$ eV. The stable form of the Au_4^- rhombus with two isolated O atoms lies 0.61 eV above the most stable form. The advantage of MP2 over B3LPY is not confirmed by the difference between the binding and desorption energies. However, it is likely that B3LYP does not accurately calculate the energy of clusters with dissociatively adsorbed O_2.

If the isomers coexist in the cluster beam, the intensity of the $Au_4O_2^-$ signal would decrease at 400 K in proportion to the isomeric ratio. The absence of such a decrease in the TDS curves suggests that each isomer is prepared selectively by use of either O_2 or N_2O as the oxidant. The energy barrier for the structural transition from molecularly to dissociatively adsorbed O_2 in $Au_4O_2^-$ is calculated to be 2.06 eV at the CCSD(T) level.[5] Hence, no structural transition is expected under the experimental conditions.

3.4.4. Structures of $Au_5O_2^-$

In the present study, $Au_5O_2^-$, which is minimally produced with O_2 as the oxidant, was formed when N_2O was used for this purpose. The TDS curves in Figure 3.2 indicate that O_2 was released from $Au_5O_2^-$ to form Au_5^- above 800 K:

$$Au_5O_2^- \rightarrow Au_5^- + O_2. \tag{3.6}$$

The thermal response suggests that O_2 is strongly chemisorbed rather than physisorbed on Au_5^-. The desorption energy is estimated to be 1.07 ± 0.04 eV from the TDS curve and the Arrhenius equation. All stable geometries obtained by calculation involve two dissociated O atoms as shown in Figure 3.4. This suggests that clusters with molecularly adsorbed O_2 do not have sufficient energetic stability. The most stable geometry is a W-shaped Au cluster with bridging O atoms. Assuming that Au_5^- retains the shape of the cluster in $Au_5O_2^-$ after release of O_2, the O_2 binding energy is calculated to be $\Delta E_5^{diss} = 1.48$ eV. Considering that $Au_5O_2^-$ must deform for the O atoms to approach one another, ΔE_5^{diss} is likely overestimated by calculation.

3.4.5. Other Anionic Gold Oxide Clusters

The TDS curves of $Au_3O_2^-$ and Au_3^- are unchanged throughout the entire temperature range suggesting that oxygen is strongly bound to Au_3^-. Photoelectron spectroscopy shows that the major structure of $Au_3O_2^-$ prepared using N_2O as oxidant possesses two separate O atoms strongly bound to Au_3^-.[4] Assuming that Au_3^- retains the shape of the Au cluster in $Au_3O_2^-$ after O_2 is released, the binding energy of dioxygen is calculated to be $\Delta E_3^{diss} = 0.55$ eV (Figure 3.5). In addition, $Au_3O(N_2O)^-$ releases N_2O to form Au_3O^-, and $Au_3O_3(N_2O)^-$ releases N_2O to form $Au_3O_3^-$ below 400 K suggesting that the N_2O molecules are weakly bound to the clusters.

The TDS curve for $Au_2O_2^-$ decreases above 850 K without an accompanying increase in intensity of an ionic counterpart. Instead, the intensity of AuO_2^- increases at this temperature (data not shown), which suggests fragmentation of $Au_2O_2^-$ into AuO_2^- and Au without desorption of O_2. The intensity of $Au_2O_2^-$ prepared using O_2 as the oxidant decreases above 750 K, and the intensity of Au_2^- increases at this temperature. The energy of O_2 desorption from $Au_2O_2^-$ is estimated to be 0.90 ± 0.10 eV. Hence, the different thermal responses of $Au_2O_2^-$ prepared by reaction of Au_2^- with O_2 or N_2O indicates that structural isomers are produced.

3.4.6. Reactions of Cationic Gold Oxide Clusters

It is known that no oxide clusters are formed when cationic gold clusters, Au_n^+, react with O_2 except for $n = 10$.[2] By analogy with the anionic clusters, an electron must be transferred from gold to O_2 for O_2 to be adsorbed. An electron deficient cationic cluster cannot provide an electron to O_2. Therefore, no cationic gold oxide clusters are formed.

To determine if N_2O can oxidize Au_n^+, we investigated the possibility of such reactions by mass spectrometry in combination with gas-phase TDS. Reaction of Au_n^+ with N_2O in He carrier gas at room temperature produced $Au_n(N_2O)_k^+$ ($n = 1-5$; $k = 1-4$) adducts. Minor amounts of $Au_nO(N_2O)_k^+$ cluster ions also were detected, probably because O atoms generated by decomposition of N_2O in the laser plasma adsorbed on the clusters. No $Au_nO(N_2O)_k^+$ species were detected when N_2O was reacted with the clusters after preparation. To elucidate the reaction at higher temperature, thermal responses were observed as the N_2O adducts were heated in the extension tube. Figure 3.6 shows the TDS plots for $Au_4(N_2O)_k^+$. The intensity of $Au_4(N_2O)_3^+$ decreases and that of $Au_4(N_2O)_2^+$ increases as the temperature is increased above room temperature. The intensity of $Au_4(N_2O)^+$ then decreases and that of bare Au_4^+ becomes dominant above 700 K. These findings suggest that N_2O molecules are released from $Au_4(N_2O)_3^+$ in a stepwise manner:

$$Au_4(N_2O)_3^+ \rightarrow Au_4(N_2O)_2^+ + N_2O \rightarrow Au_4(N_2O)^+ + 2N_2O \rightarrow Au_4^+ + 3N_2O \qquad (3.7)$$
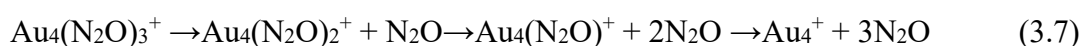
The sequential desorption energies of N_2O from the cluster were estimated to be 0.32, 0.27, and 0.23 eV. Kim and coworkers showed that electron transfer from Au_n^- to N_2O in anionic gold oxide clusters causes the O atom to dissociate from N_2O, because the dissociated state is lower in energy than the undissociated one.[5] The weak interaction between cationic Au_n^+ clusters and O does not compensate for 1.67 eV N–O bond dissociation energy of N_2O.

3.5. Conclusion

Anionic gold oxide clusters, $Au_nO_2^-$ ($n = 1-12$), were prepared by collisional O atom transfer reactions from N_2O to Au_n^-. In contrast to the established fact that only $Au_nO_2^-$ clusters with even values of n are formed by reaction of Au_n^- with O_2, $Au_nO_2^-$ with even and odd values of n were formed using N_2O as oxidant. The desorption of O_2 from $Au_nO_2^-$ upon heating was studied for $n = 2-5$ using gas-phase thermal desorption spectrometry. For $n = 2$ and 4, no desorption of O_2 was observed from species prepared with N_2O below 1000 K. However, desorption of O_2 from $Au_2O_2^-$ and $Au_4O_2^-$ occurred at 750 and 500 K, respectively, for clusters prepared by reaction of Au_2^- and Au_4^- with O_2. Theoretical calculations indicate that the most stable form of $Au_4O_2^-$, which contains dissociated O atoms on $Au_4O_2^-$, is formed using N_2O as oxidant and that the third most stable form, which contains molecular O_2 on $Au_4O_2^-$, is formed using O_2 as oxidant. For odd values of n, no desorption of O_2 was observed from $Au_3O_2^-$, whereas O_2 desorbed from $Au_5O_2^-$ at 820 K. The desorption energy estimated by TDS was 1.07

± 0.04 eV. Theoretical calculations indicate that the most stable form of $Au_5O_2^-$, which contains dissociated O atoms on the cluster, was formed using N_2O as oxidant. Thus, $Au_nO_2^-$ clusters with molecularly adsorbed O_2 were selectively formed using O_2 as oxidant, whereas $Au_nO_2^-$ clusters with dissociatively adsorbed O_2 were selectively formed using N_2O as oxidant. The individual O atoms in $Au_nO_2^-$ were more strongly bound to Au_n^- than the O_2 molecule. No oxide clusters were formed by reaction of cationic Au_n^+ species with N_2O.

3.6. References

(1)   Haruta, M. Size- and Support-Dependency in the Catalysis of Gold. *Catal. Today* **1997**, *36* (1), 153–166, https://doi.org/10.1016/S0920-5861(96)00208-8.

(2)   Cox, D. M.; Brickman, R.; Creegan, K.; Kaldor, A. Gold Clusters: Reactions and Deuterium Uptake. *Zeitschrift für Phys. D Atoms, Mol. Clust.* **1991**, *19* (1–4), 353–355, https://doi.org/10.1007/BF01448327.

(3)   Woodham, A. P.; Meijer, G.; Fielicke, A. Activation of Molecular Oxygen by Anionic Gold Clusters. *Angew. Chemie - Int. Ed.* **2012**, *51* (18), 4444–4447, https://doi.org/10.1002/anie.201108958.

(4)   Huang, W.; Zhai, H.-J.; Wang, L.-S. Probing the Interactions of O_2 with Small Gold Cluster Anions (Au_n^-, $n = 1-7$): Chemisorption vs Physisorption. *J. Am. Chem. Soc.* **2010**, *132* (12), 4344–4351, https://doi.org/10.1021/ja910401x.

(5)   Lee, H. M.; Lee, K. H.; Lee, G.; Kim, K. S. Geometrical and Electronic Characteristics of $Au_nO_2^-$ ($n = 2-7$). *J. Phys. Chem. C* **2015**, *119* (25), 14383–14391, https://doi.org/10.1021/acs.jpcc.5b03051.

(6)   Yamaguchi, M.; Miyajima, K.; Mafuné, F. Desorption Energy of Oxygen Molecule from Anionic Gold Oxide Clusters, $Au_nO_2^-$, Using Thermal Desorption Spectrometry. *J. Phys. Chem. C* **2016**, *120* (40), 23069–23073, https://doi.org/10.1021/acs.jpcc.6b08139.

(7)   Mafuné, F.; Takenouchi, M.; Miyajima, K.; Kudoh, S. Rhodium Oxide Cluster Ions Studied by Thermal Desorption Spectrometry. *J. Phys. Chem. A* **2016**, *120* (3), 356–363, https://doi.org/10.1021/acs.jpca.5b09531.

(8)   Nagata, T.; Miyajima, K.; Mafuné, F. Stable Stoichiometry of Gas-Phase Cerium Oxide Cluster Ions and Their Reactions with CO. *J. Phys. Chem. A* **2015**, *119* (10), 1813–1819, https://doi.org/10.1021/jp509592a.

(9)   Nagata, T.; Miyajima, K.; Mafuné, F. Oxidation of Nitric Oxide on Gas-Phase Cerium Oxide Clusters via Reactant Adsorption and Product Desorption Processes. *J. Phys. Chem. A* **2015**, *119* (41), 10255–10263, https://doi.org/10.1021/acs.jpca.5b07749.

(10)   Koyama, K.; Kudoh, S.; Miyajima, K.; Mafuné, F. Dissociation Energy for O_2 Release from Gas-Phase Iron Oxide Clusters Measured by Temperature-Programmed Desorption Experiments. *Chem. Phys. Lett.* **2015**, *625*, 104–109, https://doi.org/10.1016/j.cplett.2015.02.038.

(11)   Frisch, M. J.; Trucks, G. W.; Schlegel, H. B.; Scuseria, G. E.; Robb, M. A.; Cheeseman, J. R.; Scalmani, G.; Barone, V.; Mennucci, B.; Petersson, G. A.; Nakatsuji, H.; CT, W.; et al. Gaussian 09, Revision E.01. Gaussian 09 2013.

(12)   Häkkinen, H.; Yoon, B.; Landman, U.; Li, X.; Zhai, H.-J.; Wang, L.-S. On the Electronic and Atomic Structures of Small Au_N^- (N = 4−14) Clusters: A Photoelectron Spectroscopy and Density-Functional Study. *J. Phys. Chem. A* **2003**, *107*, 6168–6175, https://doi.org/10.1021/JP035437I.

(13)   Yoon, B.; Häkkinen, H.; Landman, U. Interaction of O_2 with Gold Clusters: Molecular and Dissociative Adsorption. *J. Phys. Chem. A* **2003**, *107*, 4066–4071, https://doi.org/10.1021/JP027596S.

(14)   Mills, G.; Gordon, M. S.; Metiu, H. The Adsorption of Molecular Oxygen on Neutral and Negative Au_n Clusters (n = 2−5). *Chem. Phys. Lett.* **2002**, *359* (5–6), 493–499, https://doi.org/10.1016/S0009-2614(02)00746-7.

(15)   Varganov, S. A.; Olson, R. M.; Gordon, M. S.; Metiu, H. The Interaction of Oxygen with Small Gold Clusters. *J. Chem. Phys.* **2003**, *119* (5), 2531–2537, https://doi.org/10.1063/1.1587115.

(16)   Okumura, M.; Kitagawa, Y.; Haruta, M.; Yamaguchi, K. DFT Studies of Interaction between O_2 and Au Clusters. The Role of Anionic Surface Au Atoms on Au Clusters for Catalyzed Oxygenation. *Chem. Phys. Lett.* **2001**, *346* (1–2), 163–168, https://doi.org/10.1016/S0009-2614(01)00957-5.

(17)   Liao, M.-S.; Watts, J. D.; Huang, M.-J. Theoretical Comparative Study of Oxygen Adsorption on Neutral and Anionic Ag_n and Au_n Clusters (n = 2–25). *J. Phys. Chem. C* **2014**, *118* (38), 21911–21927, https://doi.org/10.1021/jp501701f.

(18)   Ding, X.; Li, Z.; Yang, J.; Hou, J. G.; Zhu, Q. Adsorption Energies of Molecular
        Oxygen on Au Clusters. *J. Chem. Phys.* **2004**, *120* (20), 9594–9600,
        https://doi.org/10.1063/1.1665323.

(19)   Wallace, W. T.; Wyrwas, R. B.; Whetten, R. L.; Mitrić, R.; Bonačić-Koutecký, V.
        Oxygen Adsorption on Hydrated Gold Cluster Anions: Experiment and Theory. *J. Am.*
        Chem. Soc. **2003**, *125*, 8408–8414, https://doi.org/10.1021/JA034905Z.

(20)   Ding, X.-L.; Liao, H.-L.; Zhang, Y.; Chen, Y.-M.; Wang, D.; Wang, Y.-Y.; Zhang, H.-
        Y. Geometric and Electronic Properties of Gold Clusters Doped with a Single Oxygen
        Atom. *Phys. Chem. Chem. Phys.* **2016**, *18*, 28960–28972,
        https://doi.org/10.1039/C6CP05595H.
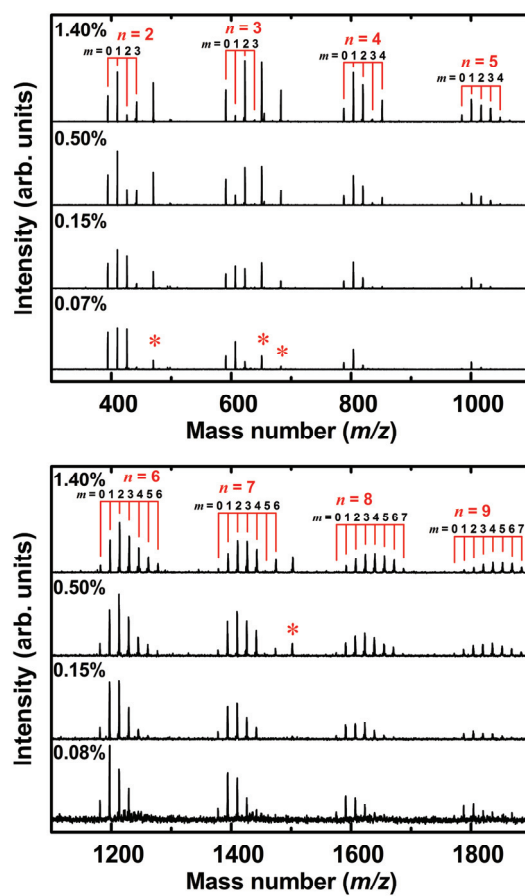
Figures

Figure 3.1. Mass spectra of anionic clusters $Au_nO_m^-$ ($n = 2-5$; $m = 0, 1, 2, \ldots$) and $Au_nO_m^-$ ($n = 6-9$; $m = 0, 1, 2, \ldots$) prepared at different N_2O concentrations in He. Asterisks (*) indicate adsorbed N_2O.
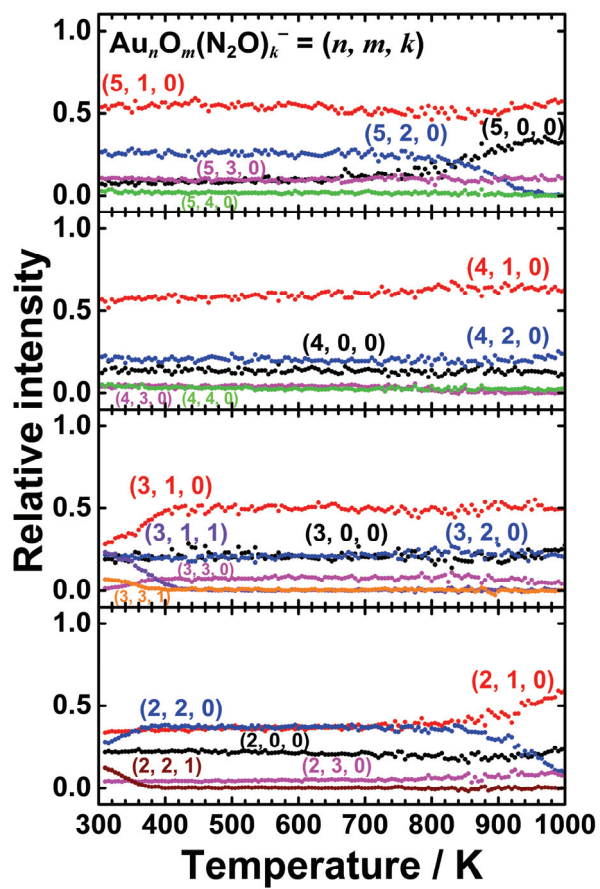
Figure 3.2. TDS curves for $Au_nO_m^-$ ($n = 2-5$) at temperatures of $300-1000$ K.
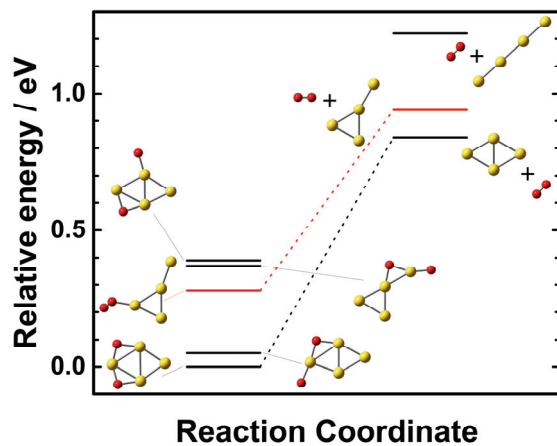
Figure 3.3. Stable geometries of Au$_4^-$ and Au$_4$O$_2^-$ calculated at the MP2 level.
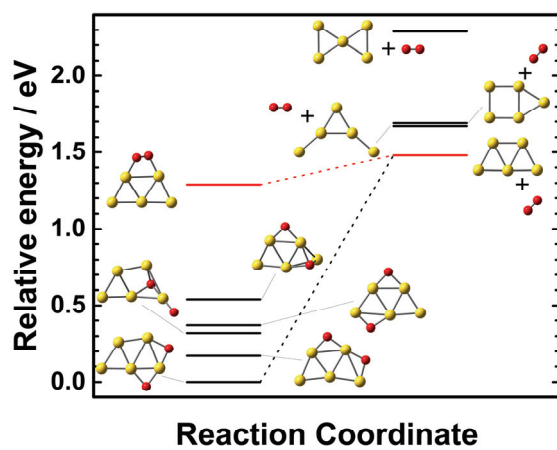
Figure 3.4. Stable geometries of Au$_5^-$ and Au$_5$O$_2^-$ calculated at the MP2 level.
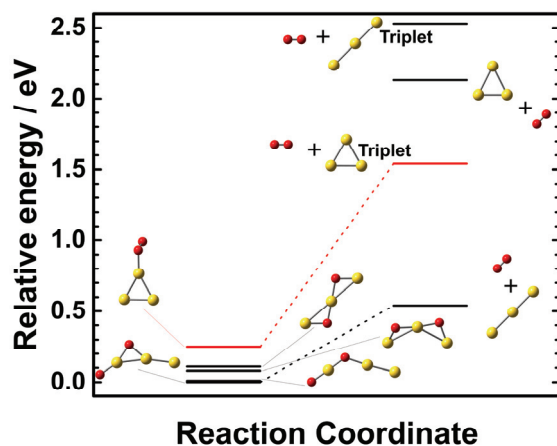
Figure 3.5. Stable geometries of Au_3^- and $Au_3O_2^-$ calculated at the MP2 level.
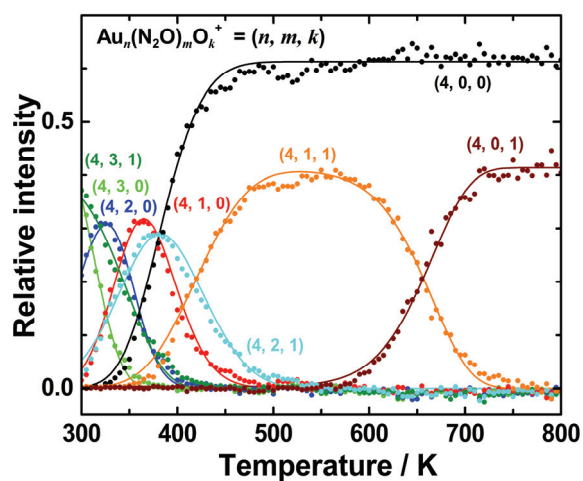
Figure 3.6. TDS curves for $Au_4(N_2O)_k^+$ at temperatures of 300−800 K.

Chapter 4

Adsorption and Desorption of NO and NO$_2$ Molecules on Gold Cluster Anions Observed by Thermal Desorption Spectrometry

The adsorption and thermal desorption of NO and NO$_2$ molecules on gold cluster anions, Au$_4^-$, were experimentally observed using gas-phase thermal desorption spectrometry. Multiple collisions of NO molecules with Au$_4^-$ at 300 K generated Au$_4$(NO)$_k^-$ ($k = 1-3$). The NO molecules desorbed from the clusters in a stepwise manner when the clusters were heated, and finally Au$_4^-$ was regenerated above 600 K. For NO$_2$, Au$_4$N$_2$O$_4^-$ was found to be thermally unstable. Hence, two NO$_2$ molecules were sequentially released from Au$_4$N$_3$O$_6^-$, when Au$_4$N$_3$O$_6^-$ was heated at 500−800 K, forming Au$_4$NO$_2^-$. A gold oxide cluster, Au$_4$O$_2^-$, was produced as a result of the decomposition of NO$_2$ to NO and O on Au$_4^-$, and the NO molecules were released above 900 K.

4.1. Introduction

With the increasing demand of fossil fuels, the reduction of NO_x, emitted upon the usage of fossil fuels, is becoming an important issue in the field of catalysis. Three-way catalysts based on the platinum group elements have been used for exhaust gases containing NO_x, CO and hydrocarbons to render them harmless. Nevertheless, there is still much interest in further elucidating reaction mechanisms for decomposition of NO and NO_2 to develop a more effective catalysis to achieve sustainable development goals (SDGs).

Small metal nanoparticles and clusters potentially bring not only higher catalytic efficiency but also new reactions. Before Haruta reported clear evidence of CO oxidation by nano-sized gold at low temperatures, it was believed that gold was inert.[1] Since this breakthrough, many studies on CO oxidation have been conducted experimentally and computationally for more than three decades.[2] CO oxidation after the co-adsorption of CO and O_2 gases on gold clusters was reported based on experiments and theories.[3–8] The CO oxidation potential was revealed for Au_2^- and Au_6^- clusters by Bernhardt and Whetten separately.[3,4] Wang and coworkers conducted photoelectron spectroscopy (PES) for CO-attached Au_6^- and reported the stabilization of the HOMO state caused by CO adsorption.[5] Recently, He and coworkers elucidated the promotion of the CO oxidation reactivity of TiO_2^- clusters by doping a gold atom.[6] In their report, gold atom plays the role of a CO trapper and an electron acceptor to assist in the oxidation.

Cox and coworkers comprehensively reported the O_2 reactivity of Au clusters and illustrated the nature of the strong size dependence of the anionic gold cluster:[9] An O_2 molecule adsorbs on Au cluster anions with even number of Au atoms. Whetten and coworkers proposed that the propensity of O_2 adsorption can be explained by the nature of the gold cluster to maintain the electron pair.[10] This reaction was also discussed using quantum calculations from the point of view of binding energies and electronic states.[11–16] Metiu and coworkers reported calculation results and concluded that this reaction was caused by electron back-donation, which is consistent with the experiments by Whetten.[10,12] Moreover, the determination of the geometries is also important, and PES and IR spectroscopy are effective tools for the characterization of gold clusters.[17–22] We also reported the interaction of O atoms with gold clusters using a combination of thermal desorption spectrometry (TDS) and quantum calculations.[23,24] The existence of isomers of $Au_nO_m^-$ clusters with different thermal stabilities

was implied, and different oxidants such as O_2 and N_2O were shown to generate molecularly and dissociatively O_2-attached clusters, respectively.

For the NO reaction, Zhu and coworkers studied NO-attached Au_n ($n = 1-6$) anionic, neutral, and cationic clusters.[25] IR spectroscopy was conducted by Rayner and coworkers using the free-electron laser for infrared experiments (FELIX).[26,27] They revealed the even-odd alternating reactivity toward NO for the Au cationic cluster, which is quite similar to the reactions of anionic Au cluster with O_2. However, reaction with NO_x, which may lead to the development of a new effective reduction catalyst, is not fully understood. Especially, binding nature and energy of NO_x on anionic Au cluster have not been provided by experiments yet, which would be helpful to understand reaction mechanism. In the present study, we report the thermal stability of products generated by the reaction of Au_4^- with NO and NO_2, as this species is the simplest reactive cluster (anion with even size) with NO that can take 3D geometry. Concentration dependence was determined and TDS was performed using NO and NO_2 gases in the gas phase. It was found that NO molecular desorption occurred one-by-one when NO gas was used. The obtained activation energy relating to NO desorption was compared and supported with calculations. For NO_2, we found the decomposition of NO_2 at high temperatures.

4.2. Experimental Methods

The adsorption and desorption of NO and NO_2 molecules on a gas-phase gold cluster anion (Au_4^-) were investigated using mass spectrometry in combination with TDS. The experimental apparatus and methods are similar to those used in previous studies; hence, only the experimental details relevant to this study are described here.[28-31]

The Au_4^- cluster was prepared inside a cluster source using pulsed laser ablation. A gold metal rod was vaporized by the focused second harmonic of the Nd:YAG pulsed laser at 532 nm. The cluster ions were generated in He gas from a pulsed valve at a stagnation pressure of 0.8 MPa. After generation, Au_4^- entered the reaction gas cell, where a reactant gas seeded in He gas was introduced from another pulsed valve at a stagnation pressure of 0.1 MPa. For NO, it is known that there are non-negligible amounts of impurity gases originating from NO in a high-pressure NO gas cylinder. The impurity gases were removed before entering the pulsed valve by using an in-line alkaline gas filter (Ascarite II adsorbents; Thomas®) and a cold trap chilled at ~160 K by frozen ethanol. Acidic gases such as NO_2 were removed by the alkaline gas filter, and high melting-point (m.p.) gases such as N_2O (m.p. 182 K) and NO_2 (m.p. 263

K as N_2O_4) were separated from NO (m.p. 109 K) by the cold trap.[32] The gases inside the vacuum chamber, introduced through the pulsed valves, were monitored by a residual gas analyzer. However, the partial pressures of NO and NO_2 were not able to be measured precisely, as the conversion of NO or NO_2 to other nitrogen oxides occurs significantly in the residual gas analyzer.

The clusters then moved into a copper extension tube before expansion into a vacuum chamber. The tube was heated to 300–1000 K using a resistive heater, and the temperatures inside and outside the tube were monitored using multiple thermocouples attached to the extension tube. The clusters were considered to achieve thermal equilibrium upon collision with the He carrier gas in the tube.

After expansion into the vacuum through a skimmer, the cluster ions were accelerated by a pulsed electric field to obtain a kinetic energy of 3.5 keV for mass analysis by time-of-flight mass spectrometry. The ions were reflected at the reflectron after passing through a 1-m field-free flight tube and were detected using a Hamamatsu double-microchannel plate detector. The signals were amplified with a 350-MHz preamplifier (Stanford Research Systems, SR445A) and were digitized using an oscilloscope (LeCroy LT374). The intensities of the cluster ions were monitored as a function of temperature using mass spectrometry, and TDS plots were obtained.

4.3. Computational Methods

The stable geometries of Au_4^-, Au_4NO^-, $Au_4N_2O_2^-$, and $Au_4NO_2^-$ were obtained by quantum chemical calculations using Gaussian 09.[33] According to the calculations by Zhu and coworkers, electron transfer occurs upon the adsorption of NO onto gold clusters.[25] Hence, we have adopted the second-order Møller-Plesset method (MP2) as it describes electron transfer well.[15,34–38] The MWB60 effective core potential (ECP) and the basis set were used to describe the Au atoms, while the 6-311G+(d) basis set was used to describe the N and O atoms.[39,40]

Before running MP2 calculations using the larger basis sets, low energy geometries of the clusters were obtained from more than 1000 randomly set initial geometries with conceivable multiplicities at reduced computational costs by using the B3LYP and the LanL2DZ basis set for Au atoms and the D95 or 6-31G(d) basis set for N and O atoms.[41–44] Geometries with energies up to +1.0 eV from the most stable were re-optimized at the MP2 level. Basis set superposition error corrections were not used. All calculations were performed

for the first, second, and third lowest spin multiplicities. Many spin isomers with nearly the same geometry and different spin states were obtained in the calculations (Figure 4.1). In such a case, we adopted the most stable isomer out of the multiple spin isomers.

4.4. Results and Discussion

4.4.1. Adsorption and Desorption of NO on Au_4^-

Figure 4.2 shows the mass spectra of Au_4^- with and without reactant NO gas after passing through the extension tube set at the indicated temperatures. Without the reactant gas, bare Au_4^- cluster is formed by the laser ablation of a gold metal rod in a He carrier gas. By introducing the reactant NO gas in the reaction gas cell, product species such as Au_4NO^-, $Au_4NO_2^-$, $Au_4N_2O_2^-$, $Au_4N_2O_3^-$, and $Au_4N_3O_3^-$ appear in the mass spectrum, and may be expressed as $Au_4(NO)_m^-$ ($m = 1-3$) and $Au_4NO_2(NO)_m^-$ ($m = 0, 1$). When the clusters are heated to 450 K in the extension tube, all the species disappear except for Au_4NO^- and $Au_4NO_2^-$, which then disappear at 1000 K, leaving Au_4^-. Thus, it is evident that multiple NO molecules adsorb onto Au_4^- at 300 K and desorb from Au_4^- at high temperatures. Appearance of $Au_4NO_2^-$ is discussed below.

To examine the desorption mechanism, intensities of the clusters were measured as a function of the temperature of the extension tube. Figure 4.3(a) shows a TDS plot: The intensity of $Au_4N_3O_3^-$ decreases, while the intensity of $Au_4N_2O_2^-$ increases with the rise in temperature at 300−350 K. Then, the intensity of $Au_4N_2O_2^-$ decreases, and the intensity of Au_4NO^- increases with temperature at 350−450 K. A similar intensity change continues until Au_4^- is formed at 600 K. Figure 4.3(b) shows the TDS curves in a differential form by temperature: A pair of peaks appearing on the positive side and the negative side in the identical temperature range indicates that the species on the positive side is formed as a result of the elimination of the species on the negative side.[45] From a visual pairwise changes, it is evident that the NO molecules are released from $Au_4N_nO_m^-$ ($n = m = 1-3$) in a stepwise manner as

$$Au_4N_3O_3^- \rightarrow Au_4N_2O_2^- + NO \qquad\qquad (4.1)$$

$$Au_4N_2O_2^- \rightarrow Au_4NO^- + NO \qquad\qquad (4.2)$$

$$Au_4NO^- \rightarrow Au_4^- + NO. \qquad\qquad (4.3)$$

In the present experiment, $Au_4N_nO_m^-$ ($n = m = 1-3$) dissociates unimolecularly inside the heated tube. Hence, the intensity of the cluster, $I(T)$, changes with temperature, T, as

$$\frac{I(T)}{I_0} = \exp(-At\exp(-\frac{E_a}{k_B T}))$$ (4.4)

where I_0, A, t, E_a, and k_B refer to the initial intensity of the cluster before entering the extension tube, pre-exponential factor, reaction time, activation energy, and Boltzmann constant, respectively. The activation energy, E_a, was obtained by fitting the experimental TDS curve in Figure 4.3(a) with Eq. (4.4), in which At and E_a were set as variable parameters. The fitting curve reproduced the experimental data reasonably well (see Figure 4.4). The activation energies thus obtained are listed in Table 4.1, which shows that the energy gradually decreases with the number of NO molecules. The trend suggests that the second and third NO molecules are more weakly bound to Au_4^- than the first one, which is similar to the case of the adsorption of O_2. Indeed, for oxygen, only one O_2 molecule adsorbs on Au_4^- and no clusters with more than two O_2 molecule were found to be produced at 300 K.[17–22] The activation energy for the desorption of one O_2 molecule from $Au_4O_2^-$ is 0.56 ± 0.05 eV, which is almost the same as Au_4NO^-.[23] Highly likely, the difference between NO and O_2 lies in the polarity of the molecules with their dipole moment, the second and third NO molecules can attach to the charged Au_4^-.

4.4.2. Desorption Energy of NO from Au_4^-

According to the DFT calculations by Ding and coworkers, Au_4NO^- optimized with the B3LYP functional (LANL2DZ and RECP basis set for Au and 6-311+G(3df) basis set for N and O atoms) takes on a Y-shaped geometry with molecular NO.[25] The charge transfer from the gold cluster to the NO molecule is an essential factor in determining the NO adsorption behavior. As a result, the π^* antibonding orbital of NO is filled by more electrons, weakening and elongating the N-O bond.

Other spin and geometrical isomers were extensively explored with MP2 (MWB60 basis set for Au atom and 6-311+G(d) basis set for N and O atoms) in the present study. The most stable structure of Au_4NO^-, 411-A, is in a singlet spin state, which comprises a NO molecule adsorbing onto the bridge site of bent Au_4 (see Figure 4.5). A geometrical isomer comprising Y-shaped Au_4 and molecular NO, 411-B, exists, the formation energy of which is +0.14 eV higher than the most stable form. In addition, another isomer composed of rhombus Au_4 and molecular NO, 411-C, is +0.22 eV higher than the most stable form. Thus, although several different geometries of Au_4^- were found, there are characteristic features for NO in the

stable isomers that the NO molecule adsorbs onto Au_4^- in molecular form from the N end. No stable isomers containing separated N and O atoms were found within +2.0 eV from the most stable one by the B3LYP screening. Hence, the desorption of the NO molecule from Au_4NO^- may not require significant recombination of chemical bonds in Au_4NO^-. Indeed, the release of the NO molecule from the isomer 411-C is accomplished only by the elongation of the bond between N and Au atoms, as the rhombus geometry is known for the most stable Au_4^- (Figure 4.5 and Figure 4.6). Similarly, NO desorption from 411-A, forming 4-C, and desorption from 411-B, forming 4-B, are expected to proceed without significant deformation. In such cases, the desorption energy, defined as the difference in the formation energies between Au_4NO^- and Au_4^- plus NO, would be close to the activation energy for desorption. Table 4.2 shows the obtained desorption energy based on the MP2 calculations. As neither geometrical structure of nascent Au_4NO^- nor Au_4^- produced from Au_4NO^- by thermal desorption is fully known, it is difficult to uniquely determine the desorption energy. Nevertheless, it is worth mentioning that the desorption energy from 411-C to 4-A is +0.57 eV, which is close to the activation energy estimated in the present study.

For $Au_4N_2O_2^-$, stable geometries obtained by the calculations were found to involve a N_2 unit (see Figure 4.7), probably because N-N bond formation stabilizes the clusters and lowers the formation energies. However, in our TDS experiments, no N_2 release was observed from $Au_4N_2O_2^-$. If the N_2 unit actually existed in the cluster, the N_2 molecule would be released at moderate temperatures, as N_2 is considered to be weakly bound to the cluster. Indeed, the theoretical calculation shows that the desorption energy of the N_2 unit is +1.18 eV (see Figure 4.8). In addition, the desorption energy of NO from the isomer would exceed 2.91 eV, which is much higher than the estimated activation energy. Hence, the experimental and computational results lead to the consideration that there is no N_2 unit in the cluster. It is highly likely that the activation barrier of the NO bond rupture is so high that the NO molecule is kinetically trapped in the metastable states.

Based on this inference, we calculated isomers with two molecular NO (see Figure 4.5). Among them, the most stable isomer, 422-A, comprises 411-B and a NO molecule attached to the first NO molecule. Another stable isomer, 422-C, comprises 411-C and a NO molecule attached to the first NO. Isomers with rhombus Au_4^- and two NO molecules adsorbed on different Au atoms was 0.37 eV higher in the formation energy than the most stable geometry (422-A). Also Y-shaped one with two NO attached on different Au atoms is 0.38 eV higher

than most stable one (see Figure 4.5 and Figure 4.7). The desorption energies of the second NO molecule for these isomers are shown in Table 4.3.

4.4.3. Adsorption and Desorption of NO_2 on Au_4^-

For NO_2, the production of $Au_4NO_2^-$, $Au_4N_2O_4^-$, $Au_4N_3O_6^-$, and $Au_4N_3O_7^-$ occurs via the reaction of Au_4^- with NO_2 molecules at 300 K. Most species may be expressed as $Au_4(NO_2)_m^-$ (m = 1-3). Figure 4.9 shows the NO_2 concentration dependence of the intensities of the cluster ions. At first, the intensity of Au_4^- decreases, and the intensities of $Au_4NO_2^-$ and $Au_4N_2O_4^-$ increase with increase in the NO_2 concentration. The intensities of $Au_4NO_2^-$ and $Au_4N_2O_4^-$ remain stable and then decrease, whereas the intensity of $AuN_3O_6^-$ continues to increase with further increase in the concentration. The concentration dependencies can be explained in terms of the sequential adsorption and desorption of NO_2,

$$Au_4^- + NO_2 \rightleftarrows AuNO_2^- \tag{4.5}$$

$$Au_4NO_2^- + NO_2 \rightleftarrows AuN_2O_4^- \tag{4.6}$$

$$Au_4N_2O_4^- + NO_2 \rightleftarrows AuN_3O_6^- \tag{4.7}$$
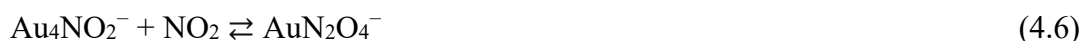
where the backward reaction in Eq. (4.6) is significant, and the reaction rate is equivalent to that of the forward reaction. Meanwhile, the rate of the forward reaction in Eq. (4.7) is much higher than that of Eq. (4.6) (see Table 4.4). The reaction rates suggest that the second NO_2 molecule in $AuN_2O_4^-$ is weakly bound, whereas $AuN_3O_6^-$ becomes quite stable on account of the presence of the third NO_2 molecule.

To investigate the thermal stability, the TDS curves were measured (see Figure 4.10). The curves for NO_2 appear more complicated than those for NO, suggesting that multiple reactions proceed in a parallel fashion. The changes in intensity can be interpreted as that $Au_4N_3O_6^-$ dissociates into $Au_4NO_2^-$ by releasing N_2O_4 in the temperature range of 500−800 K, $Au_4N_2O_4^-$ dissociates into $Au_4NO_2^-$ by releasing NO_2 at 500 K, and $Au_4NO_2^-$ dissociates into Au_4^- by releasing NO_2 at > 900 K. Thus, $Au_4N_2O_4^-$ dissociates at lower temperatures than the other compounds, indicating that the NO_2 molecule in $AuN_2O_4^-$ is weakly bound, which is consistent with the inference based on the NO_2 concentration dependence.

It is not clear if N_2O_4 or two separate NO_2 molecules are released from $Au_4N_3O_6^-$. It is assumed that once $AuN_2O_4^-$ is formed by releasing one NO_2 molecule from $Au_4N_3O_6^-$ above

500 K, $AuN_2O_4^-$ rapidly releases another NO_2 molecule to form $Au_4NO_2^-$ such that $Au_4N_2O_4^-$ cannot be detected, according to our result from the TDS experiment.

4.4.4. Decomposition of NO_2 on Au_4^-

Figure 4.10 also shows that oxygen-rich species, having more O atoms than suggested by N:O = 1:2 stoichiometry, tends to be generated at high temperatures: $Au_4NO_3^-$ is formed from $Au_4N_3O_6^-$ at > 800 K, while $Au_4O_2^-$ is formed from $Au_4NO_3^-$ at > 900 K. Based on the compositions, the N_2O_3 fragment is released in the former reaction, while NO is released in the latter reaction. The reactions can be expressed as

$$Au_4^- + 3NO_2 \rightarrow Au_4N_3O_6^- \tag{4.8}$$

$$Au_4N_3O_6^- \rightarrow Au_4NO_3^- + N_2O_3 \tag{4.9}$$

$$Au_4NO_3^- \rightarrow Au_4O_2^- + NO \tag{4.10}$$

N_2O_3 is known to decompose into NO_2 and NO at 200−300 K in the gas phase, with an activation energy of 0.42 eV.[46] Hence, the overall reaction is expressed as $2NO_2 \rightarrow 2NO + O_2$, where O_2 remains on Au_4^-. According to our previous studies, molecularly adsorbed O_2 on Au_4^- desorbs from the cluster at 400−600 K, whereas two atomically adsorbed O atoms on Au_4^- do not desorb from the cluster below 1000 K.[23,24] Hence, O_2 in the product of reaction (4.10), $Au_4O_2^-$, exists as two O atoms on Au_4^-. Considering that Au_4^- catalyzes the decomposition of NO_2, the highest activation barrier would correspond to the migration of the two O atoms on Au_4^- to encounter each other.

The formation of oxygen-rich clusters was observed for other sized Au_2^- and Au_3^- clusters, such as Au_2O^-, $Au_2NO_4^-$, $Au_2N_2O_6^-$, $Au_3O_2^-$, $Au_3NO_4^-$, and $Au_3N_2O_5^-$. In all cases, NO_2 is considered to decompose into NO and O on the cluster at high temperatures, and NO is released leaving the counter O atom in the cluster. The decomposition of NO_2 into NO and O is endothermic. Hence, the reaction has been observed in the gas phase at higher temperatures (1350−2100 K), and its activation energy was estimated to be +2.6 eV.[47] The observation of the oxygen-rich clusters below 1000 K suggests that the decomposition is accelerated on Au_4^-.

Although the decomposition of NO_2 at high temperatures is discussed above, oxygen-rich $Au_4N_3O_7^-$ was also produced as a nascent cluster, probably because the reaction with NO_2 in the gas phase is mostly adiabatic. As the result, the adsorption of multiple NO_2 molecules on Au_4^- causes the internal energy of the cluster to be high, effectively leading the cluster to a

high-temperature state. Note that the adsorption energy of one NO_2 molecule on Au_4^- is 2.51 eV according to the calculations. Stable structures obtained by quantum calculation are displayed in Figure 4.5 and Figure 4.11. Y-shaped and rhombus Au_4^- were found, which have a NO_2 molecule via center N atom, whereas third most stable isomer has NO_2 through an edge O atom. The internal energy of the clusters is to be relaxed gradually after the reaction by collision with He atoms, which are in good thermal equilibrium with the reaction gas cell.

4.4.5. Possibility of Disproportionation of NO on Au_4^-

Xing and coworkers reported the disproportionation of NO on Au_6^- at 150 K.[48] When a NO molecule collides with $Au_6N_2O_2^-$, in which two NO molecules form a precursor on Au_6^-, NO abstracts one of the N atoms from the precursor to be N_2O, leaving NO_2 on Au_6^-. For Au_4^-, we also observed $Au_4NO_2^-$ after the reactant NO gas was introduced into the reaction gas cell, which could be a product of the disproportionation reaction at 300 K. Indeed, the TDS curves in Figure 4.3 show that the intensity of $Au_4NO_2^-$ decreases while the intensity of Au_4^- increases above 900 K, indicating that NO_2 is evidently released into the gas phase as

$$Au_4NO_2^- \rightarrow Au_4^- + NO_2 \qquad (4.11)$$

It should be emphasized that $Au_4NO_2^-$, prepared by the reaction of Au_4^- and NO_2, also exhibits the release of NO_2 at the identical temperature range, as shown in Figure 4.10. The consistency of the desorbing species (NO_2) and the desorption temperature may suggest that the same species could be formed by the reaction involving NO.

However, we did not obtain clear evidence for the disproportionation reaction on Au_4^-. Although $Au_4NO_2^-$ appears in the mass spectrum after the reaction with the reactant gas (see Figure 4.2), the concentration dependence of the ion intensities on NO did not suggest that $Au_4NO_2^-$ was formed solely by a similar disproportionation reaction as Au_6^- (Figure 4.12). The ion intensity of $Au_4NO_2^-$ increases with an increase in the reactant gas concentration, but the intensities of Au_4NO^- and $Au_4N_2O_2^-$ do not change significantly. Hence, the changes in intensity do not lead to the straightforward conclusion that $Au_4NO_2^-$ is generated by the reaction of $Au_4N_2O_2^-$ with NO. We are not able to rule out the possibility that NO_2 still remains in the reactant gas after passing through the gas filter and cold trap, to adsorb onto Au_4^-. For Au_6^-, clusters Au_6NO^- and $Au_6N_2O_2^-$ decrease, while $Au_6NO_2^-$ increases in their intensities with NO

concentration; thus, the disproportionation of NO is considered to occur on Au_6^-.[48] It is highly likely that there is a size dependence for the disproportionation reaction.

4.5. Conclusion

For NO and NO_2 molecules, adsorption onto Au_4^- and thermal desorption from Au_4^-, as well as the decomposition of NO_2 on Au_4^- were investigated by experiment and quantum chemical calculations.

Multiple collisions of NO molecules with Au_4^- at 300 K generated $Au_4N_nO_m^-$ ($n = m = 1-3$), observed by mass spectrometry. When the clusters were heated, NO molecules desorbed from the clusters in a stepwise manner until Au_4^- was regenerated above 600 K. Comparison with the activation energies for desorption and the desorption energies obtained from the MP2 calculations suggest that NO molecules are molecularly adsorbed onto Au_4^- as $Au_4(NO)_k^-$ ($k = 1-3$).

For NO_2, the production of $Au_4NO_2^-$, $Au_4N_2O_4^-$, $Au_4N_3O_6^-$, and $Au_4N_3O_7^-$ occurred via the reaction of Au_4^- with multiple NO_2 molecules at 300 K. The concentration dependence of the ion intensities and the desorption temperatures of NO_2 suggest that $Au_4N_2O_4^-$ is thermally unstable. Hence, two NO_2 molecules were sequentially released from $Au_4N_3O_6^-$ when it was heated to 500−800 K.

Oxygen-rich clusters, having more O atoms than suggested by N:O = 1:2 stoichiometry, were found to be generated at high temperatures as a result of the decomposition of NO_2 to NO and O on Au_4^- and release of the NO molecules. Compared with the gas-phase decomposition reaction proceeding at higher temperatures (1350−2100 K), decomposition is considered to be accelerated on Au_4^-.

4.6. References

(1)   Haruta, M.; Kobayashi, T.; Sano, H.; Yamada, N. Novel Gold Catalysts for the Oxidation of Carbon Monoxide at a Temperature Far Below 0 °C. *Chem. Lett.* **1987**, *16* (2), 405–408, https://doi.org/10.1246/cl.1987.405.

(2)   Pattrick, G.; Lingen, E. van der; Corti, C. W.; Holliday, R. J.; Thompson, D. T. The Potential for Use of Gold in Automotive Pollution Control Technologies: A Short Review. *Top. Catal.* **2004**, *30/31* (1–4), 273–279, https://doi.org/10.1023/B:TOCA.0000029762.14168.d8.

(3)   Socaciu, L. D.; Hagen, J.; Bernhardt, T. M.; Wöste, L.; Heiz, U.; Häkkinen, H.; Landman, U. Catalytic CO Oxidation by Free Au_2^- Experiment and Theory. *J. Am. Chem. Soc.* **2003**, *125*, 10437–10445, https://doi.org/10.1021/ja027926m.

(4)   Wallace, W. T.; Whetten, R. L. Coadsorption of CO and O_2 on Selected Gold Clusters: Evidence for Efficient Room-Temperature CO_2 Generation. *J. Am. Chem. Soc.* **2002**, *124*, 7499–7505, https://doi.org/10.1021/JA0175439.

(5)   Zhai, H.-J.; Kiran, B.; Dai, B.; Jun Li, A.; Wang, L.-S. Unique CO Chemisorption Properties of Gold Hexamer: $Au_6(CO)_n^-$ ($n = 0-3$). *J. Am. Chem. Soc.* **2005**, *127*, 12098–12108, https://doi.org/10.1021/JA052618K.

(6)   Li, X.-N.; Yuan, Z.; He, S.-G. CO Oxidation Promoted by Gold Atoms Supported on Titanium Oxide Cluster Anions. *J. Am. Chem. Soc.* **2014**, *136* (9), 3617–3623, https://doi.org/10.1021/ja412608b.

(7)   Wallace, W. T.; Whetten, R. L. Carbon Monoxide Adsorption on Selected Gold Clusters: Highly Size-Dependent Activity and Saturation Compositions. *J. Phys. Chem. B* **2000**, *104* (47), 10964–10968, https://doi.org/10.1021/jp002889b.

(8)   Bernhardt, T. M.; Hagen, J.; Lang, S. M.; Popolan, D. M.; Socaciu-Siebert, L. D.; Wöste, L. Binding Energies of O_2 and CO to Small Gold, Silver, and Binary Silver-Gold Cluster Anions from Temperature Dependent Reaction Kinetics Measurements. *J. Phys. Chem. A* **2009**, *113* (12), 2724–2733, https://doi.org/10.1021/jp810055q.

(9)   Cox, D. M.; Brickman, R.; Creegan, K.; Kaldor, A. Gold Clusters: Reactions and Deuterium Uptake. *Zeitschrift für Phys. D Atoms, Mol. Clust.* **1991**, *19* (1–4), 353–355, https://doi.org/10.1007/BF01448327.

(10)   Salisbury, B. E.; Wallace, W. T.; Whetten, R. L. Low-Temperature Activation of Molecular Oxygen by Gold Clusters: A Stoichometric Process Correlated to Electron Affinity. *Chem. Phys.* **2000**, *262* (1), 131–141, https://doi.org/10.1016/S0301-0104(00)00272-X.

(11)   Okumura, M.; Kitagawa, Y.; Haruta, M.; Yamaguchi, K. DFT Studies of Interaction between O_2 and Au Clusters. The Role of Anionic Surface Au Atoms on Au Clusters for Catalyzed Oxygenation. *Chem. Phys. Lett.* **2001**, *346* (1–2), 163–168, https://doi.org/10.1016/S0009-2614(01)00957-5.

(12) Mills, G.; Gordon, M. S.; Metiu, H. The Adsorption of Molecular Oxygen on Neutral and Negative Au$_n$ Clusters (n = 2−5). *Chem. Phys. Lett.* **2002**, *359* (5–6), 493–499, https://doi.org/10.1016/S0009-2614(02)00746-7.

(13) Varganov, S. A.; Olson, R. M.; Gordon, M. S.; Metiu, H. The Interaction of Oxygen with Small Gold Clusters. *J. Chem. Phys.* **2003**, *119* (5), 2531–2537, https://doi.org/10.1063/1.1587115.

(14) Liao, M.-S.; Watts, J. D.; Huang, M.-J. Theoretical Comparative Study of Oxygen Adsorption on Neutral and Anionic Ag$_n$ and Au$_n$ Clusters (n = 2–25). *J. Phys. Chem. C* **2014**, *118* (38), 21911–21927, https://doi.org/10.1021/jp501701f.

(15) Lee, H. M.; Lee, K. H.; Lee, G.; Kim, K. S. Geometrical and Electronic Characteristics of Au$_n$O$_2^-$ (n = 2−7). *J. Phys. Chem. C* **2015**, *119* (25), 14383–14391, https://doi.org/10.1021/acs.jpcc.5b03051.

(16) Shi, H. X.; Sun, W. G.; Kuang, X. Y.; Lu, C.; Xia, X. X.; Chen, B. Le; Hermann, A. Probing the Interactions of O$_2$ with Small Gold Cluster Au$_n^Q$ (n = 2−10, Q = 0, −1): A Neutral Chemisorbed Complex Au$_5$O$_2$ Cluster Predicted. *J. Phys. Chem. C* **2017**, *121* (44), 24886–24893, https://doi.org/10.1021/acs.jpcc.7b09022.

(17) Stolcic, D.; Fischer, M.; Ganteför, G.; Kim, Y. D.; Sun, Q.; Jena, P. Direct Observation of Key Reaction Intermediates on Gold Clusters. *J. Am. Chem. Soc.* **2003**, *125* (10), 2848–2849, https://doi.org/10.1021/ja0293406.

(18) Häkkinen, H.; Yoon, B.; Landman, U.; Li, X.; Zhai, H.-J.; Wang, L.-S. On the Electronic and Atomic Structures of Small Au$_N^-$ (N = 4−14) Clusters: A Photoelectron Spectroscopy and Density-Functional Study. *J. Phys. Chem. A* **2003**, *107*, 6168–6175, https://doi.org/10.1021/JP035437I.

(19) Yoon, B.; Häkkinen, H.; Landman, U. Interaction of O$_2$ with Gold Clusters: Molecular and Dissociative Adsorption. *J. Phys. Chem. A* **2003**, *107*, 4066–4071, https://doi.org/10.1021/JP027596S.

(20) Sun, Q.; Jena, P.; Kim, Y. D.; Fischer, M.; Ganteför, G. Interactions of Au Cluster Anions with Oxygen. *J. Chem. Phys.* **2004**, *120* (14), 6510–6515, https://doi.org/10.1063/1.1666009.

(21) Huang, W.; Zhai, H.-J.; Wang, L.-S. Probing the Interactions of O$_2$ with Small Gold Cluster Anions (Au$_n^-$, n = 1−7): Chemisorption vs Physisorption. *J. Am. Chem. Soc.* **2010**, *132* (12), 4344–4351, https://doi.org/10.1021/ja910401x.

(22)   Pal, R.; Wang, L.-M.; Pei, Y.; Wang, L.-S.; Zeng, X. C. Unraveling the Mechanisms of O2 Activation by Size-Selected Gold Clusters: Transition from Superoxo to Peroxo Chemisorption. *J. Am. Chem. Soc.* **2012**, *134* (22), 9438–9445, https://doi.org/10.1021/ja302902p.

(23)   Yamaguchi, M.; Miyajima, K.; Mafuné, F. Desorption Energy of Oxygen Molecule from Anionic Gold Oxide Clusters, $Au_nO_2^-$, Using Thermal Desorption Spectrometry. *J. Phys. Chem. C* **2016**, *120* (40), 23069–23073, https://doi.org/10.1021/acs.jpcc.6b08139.

(24)   Yamaguchi, M.; Mafuné, F. Isomers of Anionic Gold Oxide Clusters, $Au_nO_2^-$, Investigated by Thermal Desorption Spectrometry. *J. Phys. Chem. C* **2017**, *121* (15), 8498–8503, https://doi.org/10.1021/acs.jpcc.7b01963.

(25)   Ding, X.; Li, Z.; Yang, J.; Hou, J. G.; Zhu, Q. Theoretical Study of Nitric Oxide Adsorption on Au Clusters. *J. Chem. Phys.* **2004**, *121* (6), 2558–2562, https://doi.org/10.1063/1.1769359.

(26)   Oepts, D.; Van Der Meer, A. F. G.; Van Amersfoort, P. W. The Free-Electron-Laser User Facility FELIX. *Infrared Phys. Technol.* **1995**, *36* (1), 297–308, https://doi.org/10.1016/1350-4495(94)00074-U.

(27)   Fielicke, A.; Helden, G. Von; Meijer, G.; Simard, B.; Rayner, D. M. Direct Observation of Size Dependent Activation of NO on Gold Clusters. *Phys. Chem. Chem. Phys.* **2005**, *7* (23), 3906–3909, https://doi.org/10.1039/b511710k.

(28)   Tawaraya, Y.; Kudoh, S.; Miyajima, K.; Mafuné, F. Thermal Desorption and Reaction of NO Adsorbed on Rhodium Cluster Ions Studied by Thermal Desorption Spectroscopy. *J. Phys. Chem. A* **2015**, *119* (31), 8461–8468, https://doi.org/10.1021/acs.jpca.5b04224.

(29)   Mafuné, F.; Takenouchi, M.; Miyajima, K.; Kudoh, S. Rhodium Oxide Cluster Ions Studied by Thermal Desorption Spectrometry. *J. Phys. Chem. A* **2016**, *120* (3), 356–363, https://doi.org/10.1021/acs.jpca.5b09531.

(30)   Kurokawa, H.; Mafuné, F. Thermal Desorption of Oxygen from Near-Stoichiometric Cationic Vanadium Oxide Clusters. *Chem. Phys. Lett.* **2016**, *651*, 24–27, https://doi.org/10.1016/J.CPLETT.2016.02.072.

(31)   Masuzaki, D.; Nagata, T.; Mafuné, F. Desorption of Oxygen from Cationic Niobium Oxide Clusters Revealed by Gas Phase Thermal Desorption Spectrometry and Density

Functional Theory Calculations. *J. Phys. Chem. A* **2017**, *121* (10), 2079–2085, https://doi.org/10.1021/acs.jpca.6b12645.

(32) *CRC Handbook of Chemistry and Physics*, 99th ed.; Rumble, J. R., Ed.; CRC Press, 2018.

(33) Frisch, M. J.; Trucks, G. W.; Schlegel, H. B.; Scuseria, G. E.; Robb, M. A.; Cheeseman, J. R.; Scalmani, G.; Barone, V.; Mennucci, B.; Petersson, G. A.; Nakatsuji, H.; CT, W.; et al. Gaussian 09, Revision E.01. Gaussian 09 2013.

(34) Head-Gordon, M.; Pople, J. A.; Frisch, M. J. MP2 Energy Evaluation by Direct Methods. *Chem. Phys. Lett.* **1988**, *153* (6), 503–506, https://doi.org/10.1016/0009-2614(88)85250-3.

(35) Frisch, M. J.; Head-Gordon, M.; Pople, J. A. A Direct MP2 Gradient Method. *Chem. Phys. Lett.* **1990**, *166* (3), 275–280, https://doi.org/10.1016/0009-2614(90)80029-D.

(36) Frisch, M. J.; Head-Gordon, M.; Pople, J. A. Semi-Direct Algorithms for the MP2 Energy and Gradient. *Chem. Phys. Lett.* **1990**, *166* (3), 281–289, https://doi.org/10.1016/0009-2614(90)80030-H.

(37) Head-Gordon, M.; Head-Gordon, T. Analytic MP2 Frequencies Without Fifth-Order Storage. Theory and Application to Bifurcated Hydrogen Bonds in the Water Hexamer. *Chem. Phys. Lett.* **1994**, *220* (1–2), 122–128, https://doi.org/10.1016/0009-2614(94)00116-2.

(38) Sæbø, S.; Almlöf, J. Avoiding the Integral Storage Bottleneck in LCAO Calculations of Electron Correlation. *Chem. Phys. Lett.* **1989**, *154* (1), 83–89, https://doi.org/10.1016/0009-2614(89)87442-1.

(39) Andrae, D.; Häußermann, U.; Dolg, M.; Stoll, H.; Preuß, H. Energy-Adjusted Ab Initio Pseudopotentials for the Second and Third Row Transition Elements. *Theor. Chim. Acta* **1990**, *77* (2), 123–141, https://doi.org/10.1007/BF01114537.

(40) Krishnan, R.; Binkley, J. S.; Seeger, R.; Pople, J. A. Self-Consistent Molecular Orbital Methods. XX. A Basis Set for Correlated Wave Functions. *J. Chem. Phys.* **1980**, *72* (1), 650–654, https://doi.org/10.1063/1.438955.

(41) Becke, A. D. Density-Functional Thermochemistry. III. The Role of Exact Exchange. *J. Chem. Phys.* **1993**, *98* (7), 5648–5652, https://doi.org/10.1063/1.464913.

(42)   Lee, C.; Yang, W.; Parr, R. G. Development of the Colle-Salvetti Correlation-Energy Formula into a Functional of the Electron Density. *Phys. Rev. B* **1988**, *37* (2), 785–789, https://doi.org/10.1103/PhysRevB.37.785.

(43)   Hay, P. J.; Wadt, W. R. Ab Initio Effective Core Potentials for Molecular Calculations. Potentials for K to Au Including the Outermost Core Orbitals. *J. Chem. Phys.* **1985**, *82* (1), 299–310, https://doi.org/10.1063/1.448975.

(44)   Dunning, T. H.; Hay, P. J. No Title. In *Modern Theoretical Chemistry*; Schaefer, H. F. I., Ed.; Plenum: New York, 1976; pp 1–28.

(45)   Nagata, T.; Miyajima, K.; Mafuné, F. Oxidation of Nitric Oxide on Gas-Phase Cerium Oxide Clusters via Reactant Adsorption and Product Desorption Processes. *J. Phys. Chem. A* **2015**, *119* (41), 10255–10263, https://doi.org/10.1021/acs.jpca.5b07749.

(46)   Atkinson, R.; Baulch, D. L.; Cox, R. A.; Crowley, J. N.; Hampson, R. F.; Hynes, R. G.; Jenkin, M. E.; Rossi, M. J.; Troe, J. Evaluated Kinetic and Photochemical Data for Atmospheric Chemistry: Volume I - Gas Phase Reactions of O_x, HO_x, NO_x and SO_x Species. *Atmos. Chem. Phys.* **2004**, *4* (6), 1461–1738, https://doi.org/10.5194/acp-4-1461-2004.

(47)   Röhrig, M.; Petersen, E. L.; Davidson, D. F.; Hanson, R. K. A Shock Tube Study of the Pyrolysis of NO_2. *Int. J. Chem. Kinet.* **1997**, *29* (7), 483–493, https://doi.org/10.1002/(SICI)1097-4601(1997)29:7<483::AID-KIN2>3.0.CO;2-Q.

(48)   Ma, J.; Cao, X.; Chen, M.; Yin, B.; Xing, X.; Wang, X. Low-Temperature Disproportionation Reaction of NO on Au_6^-: A Mechanism Involving Three NO Molecules Promoted by the Negative Charge. *J. Phys. Chem. A* **2016**, *120* (46), 9131–9137, https://doi.org/10.1021/acs.jpca.6b09129.

Figures

(a) singlet
0 eV

411-A

(b) triplet
+0.14 eV

411-B

(c) singlet
+0.18 eV

411-B'

(d) singlet
+0.22 eV

411-C

(e) triplet
+0.34 eV

411-C'

(f) triplet
+0.45 eV
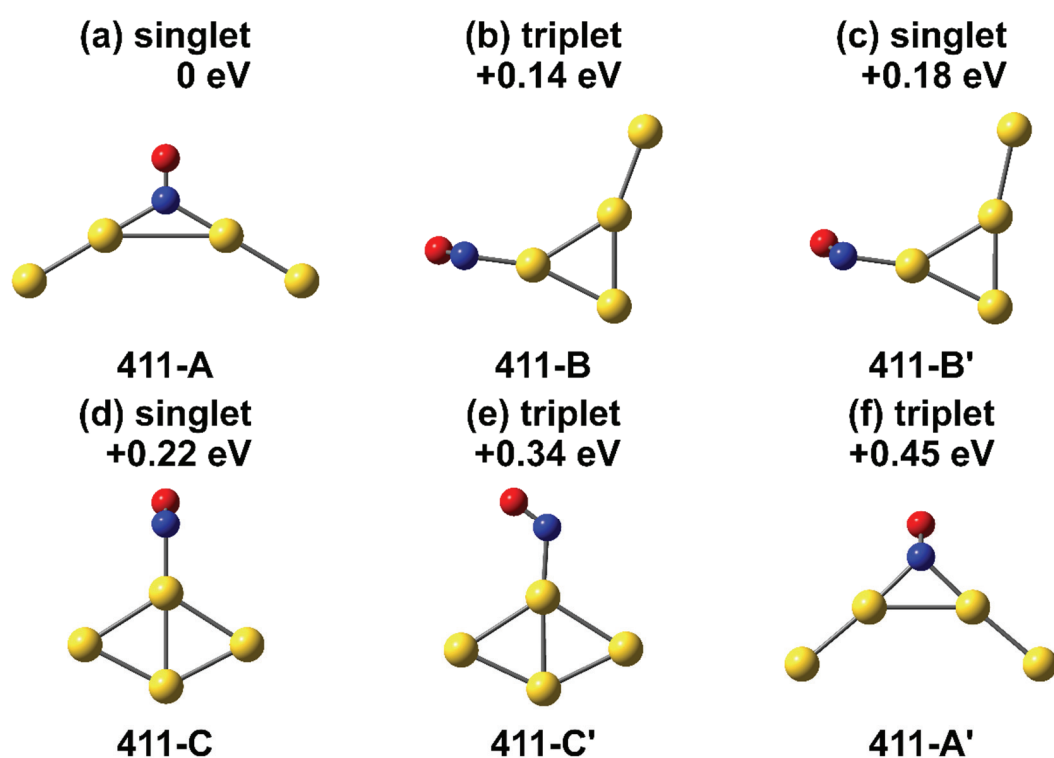
411-A'

Figure 4.1. Stable isomers of Au_4NO^- obtained by quantum chemical calculations using MP2. Spin state and energy difference from the most stable isomer, 411-A, are shown. Spin isomers with almost the same geometry and a different spin state are categorized using the same label and the prime symbol.
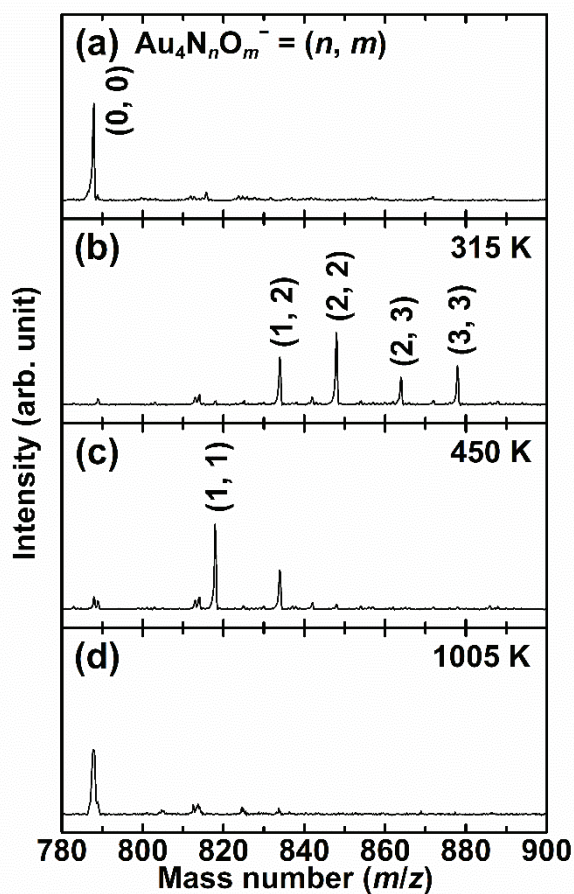
Figure 4.2. (a) Mass spectrum of nascent Au₄⁻ produced by the laser ablation of a Au rod in He gas. (b) Mass spectrum of product clusters after reaction with the reactant NO gas in the reaction gas cell. Mass spectra of clusters after passing through the extension tube heated at (c) 450 K and (d) 1000 K.
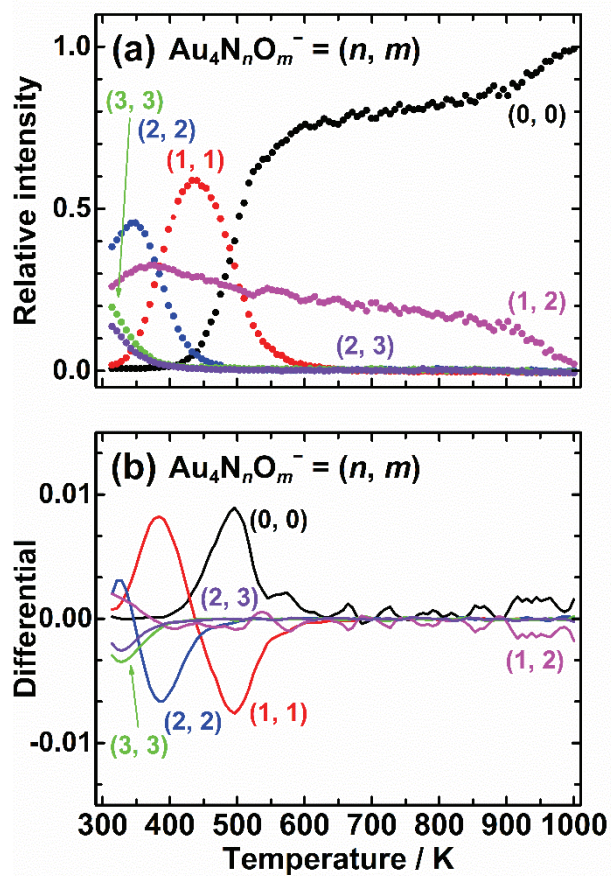
Figure 4.3. (a) A TDS plot of Au4N*n*O*m*⁻ produced by the reaction of Au4⁻ with reactant NO gas. (b) TDS curves of (a) in differential form with respect to temperature.
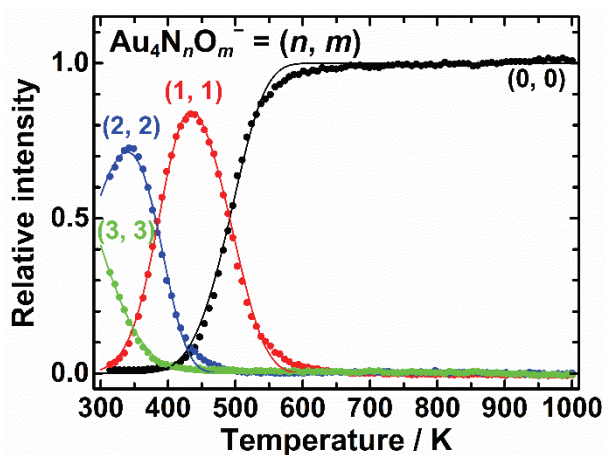
Figure 4.4. TDS curves of Au4N*n*O*m*⁻ (*n* = *m* = 0−3) and fitting curves using eq. (4.4).
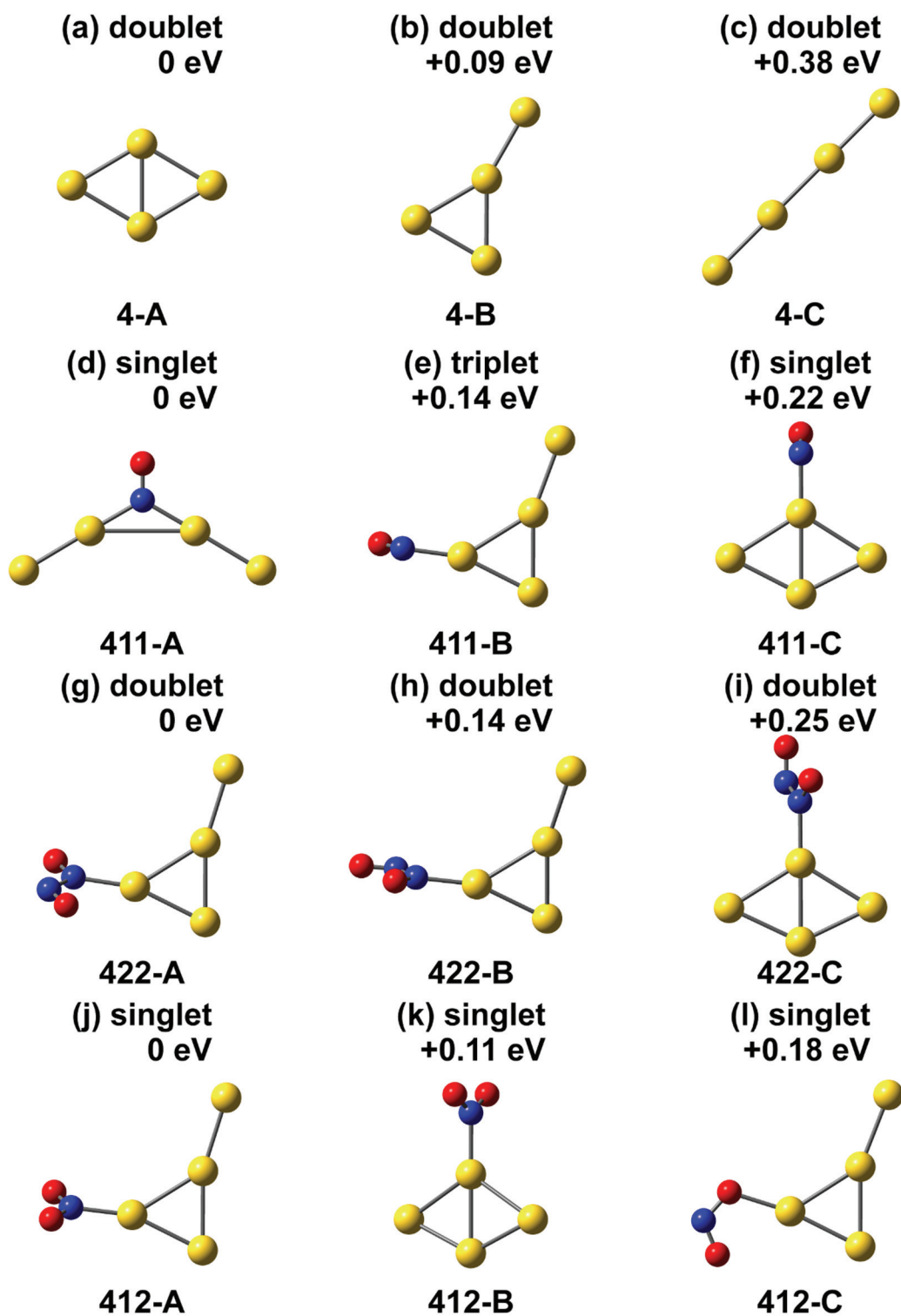
Figure 4.5. Stable isomers of Au_4^-, Au_4NO^-, $Au_4N_2O_2^-$ and $Au_4NO_2^-$ obtained by quantum chemical calculations using MP2. Spin state and energy difference from the most stable isomer are shown.
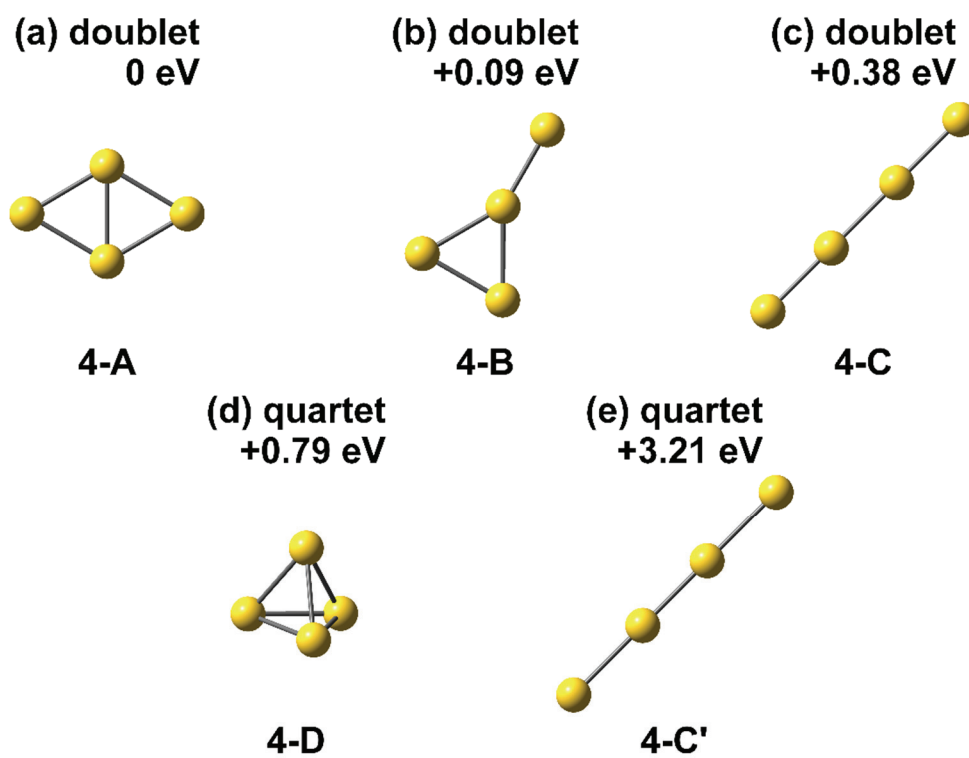
Figure 4.6. Stable isomers of Au$_4^-$ obtained by the theoretical calculations. Spin state and energy difference from the most stable isomer, 4-A, are shown.
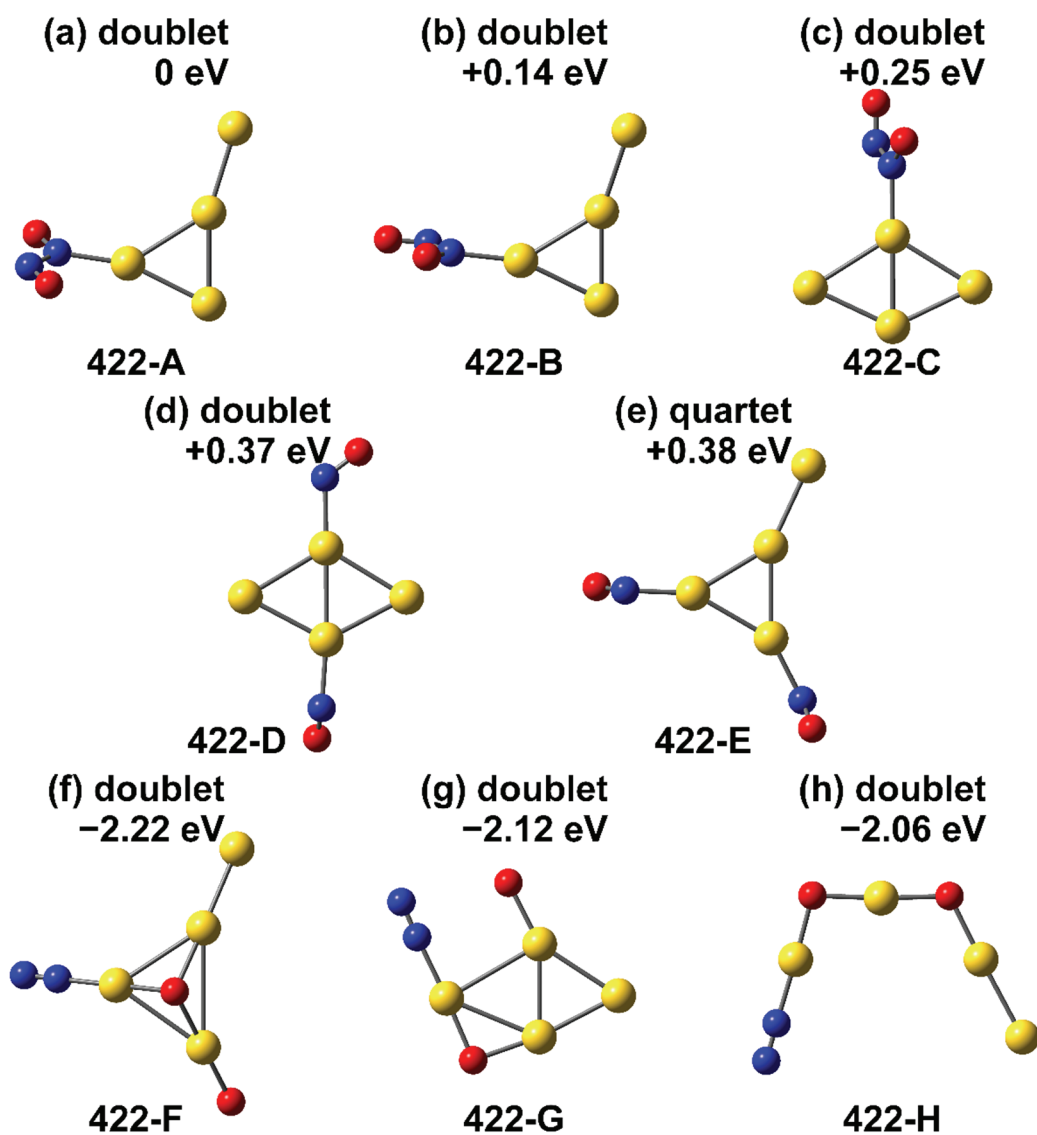
Figure 4.7. Stable isomers of $Au_4N_2O_2^-$ obtained by the MP2 calculations. Spin state and energy difference from the most stable isomer are shown. Stable geometries were found to involve an N_2 unit.
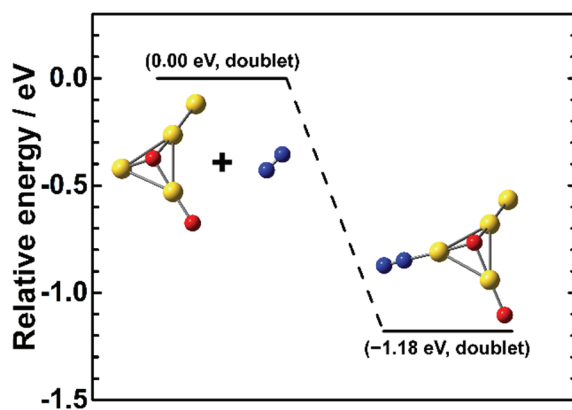
Figure 4.8. Desorption energy required to release N_2 from $Au_4N_2O_2^-$.
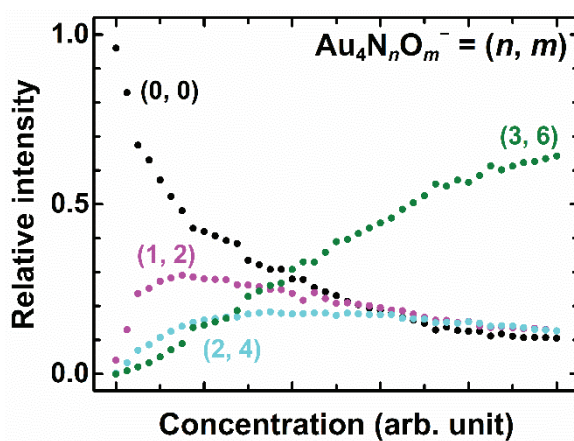
Figure 4.9. NO_2 concentration dependence of the intensities of the cluster ions produced by the reaction of Au_4^- with the reactant NO_2 gas.
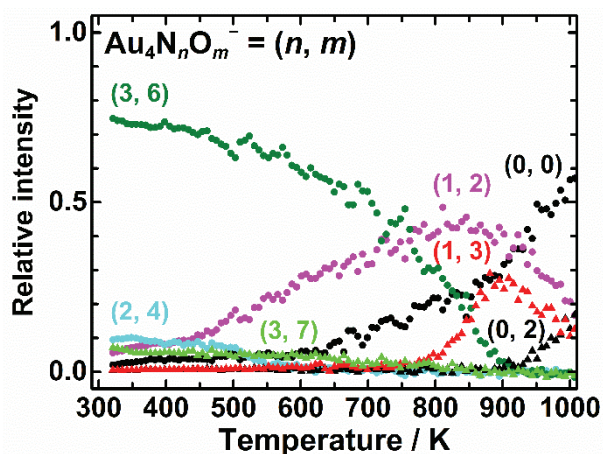
Figure 4.10. (a) TDS plot of $Au_4N_nO_m^-$ produced by the reaction of Au_4^- with reactant NO_2 gas.
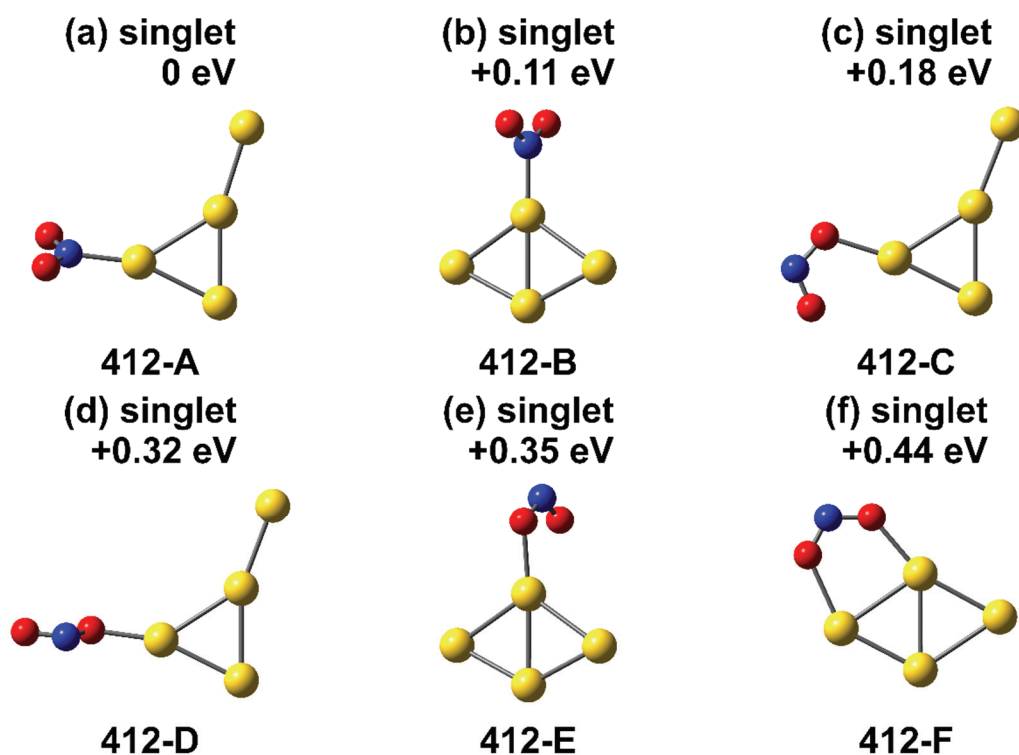
Figure 4.11. Stable isomers of $Au_4NO_2^-$ obtained by the MP2 calculations. Spin state and energy difference from the most stable isomer are shown.
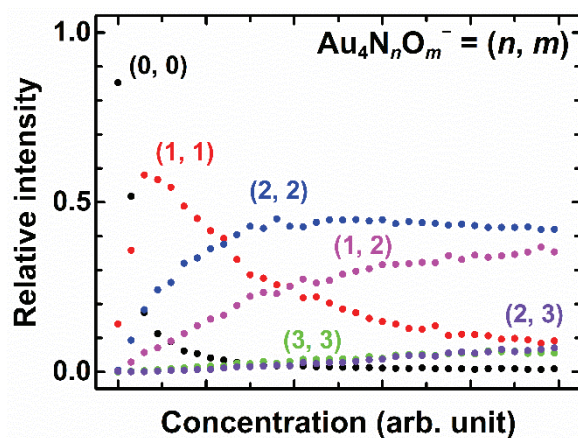
Figure 4.12. NO concentration dependence of the intensities of the cluster ions produced by the reaction of Au_4^- with the reactant NO gas.

Table 4.1. Experimentally estimated activation energy, E_a, for the desorption of a NO molecule in eV.

Reaction	E_a
$Au_4NO^- \rightarrow Au_4^- + NO$	0.55 ± 0.06
$Au_4N_2O_2^- \rightarrow Au_4NO^- + NO$	0.34 ± 0.06
$Au_4N_3O_3^- \rightarrow Au_4N_2O_2^- + NO$	0.07 ± 0.03

Table 4.2. Energy, ΔE, for the desorption of a NO molecule in eV

	4-A	4-B	4-C
411-A	0.79	0.88	1.16
411-B	0.65	0.74	1.03
411-C	0.57	0.66	0.94

Table 4.3. Energy, ΔE, for the desorption of the second NO molecule in eV.

	411-A	411-B	411-C
422-A	0.69	0.83	0.91
422-B	0.55	0.69	0.77
422-C	0.43	0.57	0.66

Table 4.4. Relative rate constant, k, for the adsorption and desorption of NO_2.

clusters	adsorption	desorption
Au_4^-	1.00	-
$Au_4NO_2^-$	1.08	0.84
$Au_4N_2O_4^-$	0.92	0.74
$Au_4N_3O_6^-$	-	0.13

Chapter 5

Structural Determination of Nitrogen Oxides Attached Gold Anionic Clusters by Infrared Multiple Photon Dissociation Spectroscopy

The adsorption forms of NO and NO_2 on the anionic Au_4^- cluster were investigated by a combination of IRMPD experiments and DFT calculations. From the results, we conclude that in all three species investigated (Au_4NO^-, $Au_4N_2O_2^-$ and $Au_4NO_2^-$) Au_4^- forms a triangle-shaped Au_3 with one Au atom sticking out, on which NO and NO_2 molecules adsorb molecularly . Disproportionation of NO by Au_4^- is discussed on the basis of the found geometries of the intermediate species. Geometries and their energy levels suggeste that the catalytic reaction of NO decomposition can occur on the Au_4^- cluster.

5.1. Introduction

NO decomposition is one of the most attracting subject in the catalytic research, and has been extensively and intensively investigated over few decades. As the background, there are increasing demands for the fossil fuel with the development of the society. Hence, designing state of the art catalysis is urgent task in the society to reduce NO emission. For example, three-way catalytic converter containing the platinum group elements has been used to redox the pollutants of automobile's exhaust into the harmless gases by the after-treatment methods. One reaction in which NO can be converted into more harmless chemical substances is the disproportionation reaction, where 3 NO molecules are converted into N_2O and NO_2.

The reactivity of nano-sized catalysis, containing nanoparticles or clusters can be altered drastically by tuning the size or the composition. Indeed, gold is a famous inert metal in the bulk size, and had been believed inert in any forms. Since gold was found to have pronounced reactivity of CO oxidation even under the low temperature, gold has been investigated intensively over two decades, as emerging new catalytic material.[1]

For gold nanoparticles, CO oxidation reactions were reported with metal oxides support, such as TiO_2, Fe_2O_3 and MgO.[2,3] In this context, gas phase Au clusters, regarded as the catalytic active center of this reaction, were studied by several researchers experimentally and computationally.[4-7] Bernhardt and coworkers demonstrated a CO oxidation reaction cycle on the anionic Au_2^- cluster with the O_2 coadsorption, whereas Whetten and coworkers demonstrated on the Au_6^- respectively.[5,6] He and coworkers elucidated the enhancement of the CO oxidation reaction on the TiO_2 by doping of one gold atom in the presence of O_2.[7] In their speculation, the added gold plays the role of CO trapper and electron acceptor, thus combination with the supporter material is also behave as the efficient catalysis.

Reactions with NO on gold clusters were also investigated by many researchers.[8-11] Zhu and coworkers reported calculated geometrical structures of NO attached to small Au_n^q (n = 1-6, q = ±1, 0) clusters.[8] IR vibrational spectroscopy was conducted by Rayner, Fielicke, and coworkers who discovered a pronounced oscillation of the vibrational frequency of NO attached to Au_n^+ (n = 2-20), whereas CO attachment did not show any variation of the frequency.[10] It is thus highly likely that the electron distribution is an important factor in determining the nature of adsorption for NO. Because of the curiosity on this system, we conducted thermal desorption spectrometry (TDS) experiments to estimate the activation

energies for the release of adsorbed NO and NO_2.[11] A combination of the observed data with the theoretical calculation, led us to conclude that all nitrogen oxides were adsorbed intact.

Recently, the adsorption of multiple NO molecules onto Au_n^- (n = 4, 6, 8) clusters was studied by Xing and coworkers,[9] who mass-spectrometrically observed the formation of $Au_n^- \cdot NO_2$. Their concomitant DFT calculations suggested that two NO molecules adsorb on the apex of the triangular cluster, forming an O-N_2-O species. When the third NO molecules adsorbed to this O-N_2-O, one of the O atoms is transferred to NO, resulting in the formation and release of N_2O, leaving NO_2 behind on the gold cluster.

In the present work, we investigated geometrical structures of the gold clusters associated to the disproportionation reaction. The products formed upon reacting anionic Au_4^- clusters with NO and NO_2, $Au_4N_nO_m^-$, were characterized using Infrared multiple photon dissociation (IRMPD) spectroscopy, which can provide direct structural information on the basis of the vibrational bands. As a result, it was found that all examined structures possess contain intact NO, NO_2 and $(NO)_2$. Especially $Au_4(NO)_2^-$ can be regard as the precursor of the NO disproportionation reaction.

5.2. Experimental Methods

We conducted experiments investigating the adsorption of NO to anionic Au_n^- clusters in the gas phase via IR spectroscopy using the free-electron laser for infrared experiment (FELICE) in the Radboud University, the Netherlands.[12,13] We employed similar experimental methods as the ones reported in our previous studies, and hence we described mainly on preparation of clusters and a FELIX setup for infrared multiple photon dissociation spectroscopy relevant to the present study.[14–18]

Anionic Au_4 clusters were generated in a vacuum chamber through laser ablation. Either a 0.1 mm thick gold foil, spot welded to a stainless steel rod, or a solid gold rod (Furuya Metal Co., Ltd.; 99.95%) was vaporized by the second harmonic of a pulsed Nd:YAG laser (532 nm, 20Hz) in the presence of a He carrier gas. Generated clusters were reacted with NO molecules in a reactant mixture gas composed of He and NO (20% NO/He) to form NO-attached gold clusters, $Au_4N_nO_m^-$. Carrier and reactant gases were injected by pulsed valves (General Valve, Parker, 20Hz, typical opening time 200 μs) with stagnation pressures of 0.8 MPa and 0.1 MPa, respectively. The mixture of clusters, cluster-NO complexes and helium subsequently expanded into the vacuum chamber forming a molecular beam.

The molecular beam entered a higher vacuum chamber through a 2-mm diameter skimmer and a 0.45 mm slit aperture, to reach the two extraction plate electrodes of a reflectron time-of-flight mass spectrometer, where the clusters were irradiated with the IR laser. Sequential absorption of IR photons by $Au_4N_nO_m^-$ resulted in dissociation of the clusters, which was probed by mass spectrometry. The IRMPD spectra were obtained by scanning the wavelength of the IR laser in steps of 5.0 or 2.5 cm^{-1}. The free-electron laser was operated at 10 Hz, whereas the ablation laser emitted light at 20 Hz. We recorded mass spectra with IR on and off alternatively to reduce fluctuations caused by experimental conditions.

Note that in the present study, NO was used from a gas cylinder was used at room temperature, without the use of a liquid nitrogen trap to remove contaminant molecules other than NO. As it is known that NO_2 can get formed in NO cylinders, we cannot rule out that $Au_4NO_2^-$ formed in the experiment results from impurities. Indeed, a control experiment using pure NO_2 gas has shown the same response to the thermal reaction by TDS experiment.[11] Formation of NO_2 by the disproportionation reaction in the gas phase clusters was proposed by Xing and coworkers, where NO_2 is generated under the low-temperature condition by decomposing three NO molecules on the even sized gold cluster anion, not only Au_6^- but also Au_4^- and Au_8^-.[9] However, we found that the reaction rate is much smaller for Au_4^- than Au_6^-.[11]

5.3. Computational Methods

We conducted DFT calculations to obtain stable geometries of the clusters using Gaussian 09 program.[19] Computational steps were almost the same as those adopted in the previous studies.[17,18] For Au_4NO^-, $Au_4N_2O_2^-$, and $Au_4NO_2^-$, we conducted full calculations: First, we prepared more than ten thousand initial geometries by positioning randomly the constituent atoms in space and by setting the spin state in conceivable spin states. All the geometries were optimized by B3LYP functional using LanL2DZ basis sets with effective core potential (ECP) for Au and 6-31+G(d) basis sets for N and O.[20–24] Second, to ensure the first screening, over 20 low-energy geometries were selected from each spin state, and they were optimized again for different conceivable spin states by using the same basis sets, thus we obtained ensemble of possible geometries. Finally, the geometries were re-optimized using larger basis sets, MWB60 basis set with ECP for Au, and 6-311+G(d) for N and O before vibrational frequencies were calculated.[25–27]

We also employed other methods than B3LYP such as PBE, and PBE1. Essentially same low-lying geometries were obtained by these methods, although relative energies varied with the methods (Figure 5.1). We limit ourselves to discussing all results obtained using B3LYP, as they can adequately explain the present results. All results obtained with the PBE and PBE1 are included in the Supporting Information.

The computational results obtained in the present study are consistent with those presented in our previous study, where Møller-Plesset 2 (MP2) method was used.[11] However, stability represented by the formation energy was not exactly same and the energy sequence of isomers has been swapped. This finding implies that variation of the calculational methods leads to the different results in geometries and energetic orders, which is not negligible for Au clusters.

Vibrational spectra are presented by convoluting the (unscaled) harmonic frequencies and intensities using a Gaussian line shape function with a 20 cm^{-1} fwhm bandwidth above 300 cm^{-1} and with a 5 cm^{-1} fwhm bandwidth below. Zero-point energies are included in relative energies in parentheses.

5.4. Results and Discussion

5.4.1. Au_4NO^-

Figure 5.2 shows the experimental and computational results for Au_4NO^-. Panel (a) shows the IRMPD spectrum, which was recorded in 2.5 cm^{-1} steps for the 150-330 cm^{-1} spectral range and in 5 cm^{-1} steps for higher frequencies, respectively. Four bands are observed at 192.5, 485, 750, and 1485 cm^{-1}, with both the 485 cm^{-1} and 1485 cm^{-1} bands appearing to have a low-frequency shoulder. It can also be seen that between 750 cm^{-1} and 1485 cm^{-1} bands a pronounced slope is observed. In a spectrum recorded with lower IR intensity, the baseline is flat, and no slope is visible. We attribute this seeming non-resonant excitation to the high intensities provided by the FELICE IR laser, which could for instance allow the excitation of overtones and/or combination bands. This was previously seen in IRMPD spectra for the coronene cation.[28]

The most stable isomers obtained in the DFT calculations are shown in Figure 5.2(b-e). It is well known that metal clusters tend to form stable isomers that differ slightly in their geometries and spin states. Hence, several energetically stable isomers are shown, in order to investigate which structure(s) are actually formed in this study. Isomer 11-A, triplet spin state,

has a triangular Au skeleton with the fourth Au atom on one of the apices giving the cluster a Y-shape. NO is molecularly attached to another apex of the triangle with N binding to the gold. The same structure in singlet spin configuration, isomer 11-B, was found near-isoenergetic at 0.02 eV (panel (d)). In a third isomer at 0.02 eV, 11-C (singlet) the tetramer cluster adopts a bent Au-Au-Au-Au chain shape, with NO adsorbed symmetrically on a bridge site, which gives the impression as if the tetramer is split into two dimers by the NO molecule. The fourth isomer discuees here, 11-D in panel (e), has a rhombus Au structure in a singlet spin state, with NO adsorbed molecularly with N attached to the gold. Several further energetically low-lying structures are shown in the Supporting Information (Figure 5.1). Note that, isomer 11-D is not fourth most stable geometry in present calculations. However, the rhombus and Y shapes are well known geometries for the gold tetramer, and the energetic order depends on the chosen exchange-correlation functional.[29] Thus, all energetically stable structures have an intact NO molecule bound by the N. Clusters with an intact NO bound by the O were found at energies above +0.59 eV, and clusters with dissociatively adsorbed NO were found above +2.3 eV higher in energy compared with global minimum, isomer 11-A (see Figure 5.3).

All stable isomers of Au_4NO^- show an intense band in 1500-1600 cm^{-1}, due to a lightly activated NO stretching vibration. It is of interest to note that the 1495 cm^{-1} frequency of the IRMPD band, undoubtedly assigned to the NO stretching vibration, is slightly lower than the stretching vibration of intact NO on a crystalline gold surface, Au(111), which can be caused by electron transfer from Au_4^- to the anti-bonding π^* orbital of NO.[10,30]

Bands in all lower-frequency regions are due to vibrations including Au atoms. As the IRMPD spectrum shows no peaks in the range between 900 and 1300 cm^{-1}, where modes involving terminal Au-N or Au-O groups would appear, we conclude that NO stays intact on Au_4^-.

For the low wavenumber peaks, isomers 11-A to 11-D possess two or three bands with relatively high IR intensities below 300 cm^{-1}. The most stable spin isomers 11-A and 11-B both have three prominent peaks, at 128, 168 and 225 cm^{-1} (for 11-A), and at 118, 170 and 252 cm^{-1} (11-B), respectively. Isomer 11-C has prominent peaks at 148, 249 and 278 cm^{-1}. Nevertheless, the experimental results show only one band in this region, at 192.5 cm^{-1}, making the assignment of this spectrum in this region not possible. Hence, the bands at 485 cm^{-1} and 750 cm^{-1} are key to determine the structure. As no structure has any band predicted near 750 cm^{-1}, we attribute this band to be due to the NO stretch vibration (experimentally observed at 1495

cm^{-1}), excited by a small, but observable contribution of the 2nd harmonic present in the FEL cavity, estimated to be on the order of 1% of the fundamental. Given the calculated strength of the NO stretch vibration, which exceeds 2000 km/mol the appearance of a 2nd harmonic induced absorption is not unreasonable, given that the calculated intensity of the next strongest band is only 15 km/mol (376 cm^{-1} band, 11-A).

Compared with the calculated bands at 376, 447, and 351/614 cm^{-1} for isomers 11-A, B and C respectively, assignment of the 485 cm^{-1} band to isomer 11-B appears most straightforward. This would then mean the 192.5 cm^{-1} is then either due to the predicted band at 252 cm^{-1}, which appears maybe too far away, or to the band predicted at 170 cm^{-1}. We lean to the latter interpretation, which implies that the band at 252 cm^{-1} is too weak to detect in the non-linear IRMPD process, as the 170 cm^{-1} is not only closer in frequency, but its proximity to the 168 cm^{-1} band of 11-A allows to ascribe the low-frequency shoulder of the 485 cm-1 band to the calculated vibrational mode at 376 cm^{-1} of 11-A.

In our previous study employing TDS, we observed NO desorption from Au$_4$NO$^-$ and established the activation energy for this proces.[11] Computationally, we found several stable candidate isomers within 1 eV of the formation energy. In the present study, we conclude that isomer 11-A and 11-B, with structures of a triangular Au skeleton with N-end intact NO attached motif, coexist as the Au$_4$NO$^-$ cluster according to the vibrational frequencies and relative energies, which is consistent to our previous study.

5.4.2. Au$_4$N$_2$O$_2^-$

The experimental and computational results on Au$_4$N$_2$O$_2^-$ are shown in Figure 5.4. In the experimental IRMPD spectrum in panel (a), two intense broad bands appear around 1530 and 1660 cm^{-1} accompanied by a weaker band at 620 cm^{-1} on an elevated baseline. The bands at 1530 and 1660 cm^{-1} indicate that either an intact NO or NO$_2$ molecule should exist in the cluster. However, screening of stable isomers of Au$_4$N$_2$O$_2^-$ by DFT calculation indicated that stable structures tend to have two separate O atoms and N$_2$ molecule such as isomer 22-D. The stability of this motif is yielded by the N-N bond formation. Highly likely, there exists high energy barrier for the formation of isomer 22-D, since two NO bonds should be ruptured. Hence, we focus tentatively the isomers with intact NO and set isomer 22-A as reference of relative

energies for simplicity. It was found that almost all the stable isomers are in the doublet spin state even for NO separated cluster such as isomer 22-D (see Figure 5.5).

The isomer D includes a N_2 molecule, which should exhibit a N_2 vibration around 2300 cm^{-1}. In the present study, IR laser was tuned in the spectral range of 150-1800 cm^{-1}, so that the specific band has not been probed. As isomer 22-D shows no bands in 800-2000 cm^{-1}, which is different from our observation, we consider that the isomer 22-D should not dominantly contribute in $Au_4N_2O_2^-$. Moreover, in our previous study on $Au_4N_2O_2^-$, we observed that two NO molecules desorbed one by one from $Au_4N_2O_2^-$ when heated in the thermal desorption spectrometry: Activation energy of NO desorption from $Au_4N_2O_2^-$ was ~0.34 eV.[11] The low activation energy suggests that NO adsorbs molecularly, not dissociatively, on Au_4NO^-. Hence, we can consider that the cluster contains one molecular NO at least (Figure 5.5).

The stable geometry, isomer 22-A, has two molecular NO and the geometry resembles the isomer 11-A and 11-B of Au_4NO^- as shown in Figure 5.2. The second NO attaches on nitrogen of first NO as N-end. Isomer 22-B has a similar geometry with isomer 22-A except for the orientation of the second NO molecule. In addition, isomer 22-C takes two NO molecules separately on triangular shaped Au skeleton. Isomer 22-A and B have similar vibrational features: For isomer 22-A, peaks appearing at 1451, 1364, 932, 646 and 540 cm^{-1} whereas isomer 22-B shows peaks at 1481, 1387, 939, 632 and 381 cm^{-1}, originate from the NO molecule. However, these vibrational features are also observed in other geometrical isomer which has rhombus shape as Au frame (Figure 5.5(h)), indicating that vibrational features in this region do not vary with the skeleton structure of Au_4. These vibrational peaks were due to ON-NO moiety. In contrast, isomer 22-C, which has two NO at different sites respectively, has no vibrational peak from 400 to 1400 cm^{-1}. Considering that the experimental result showed peak at 620 cm^{-1} and the isomer 22-C is energetically 0.32 eV unstable than the isomer 22-A, isomer 22-A and/or B contribute mainly for $Au_4N_2O_2^-$. The relative intensities of the bands in IRMPD spectrum appears to be reproduced more by the vibrational IR intensities of the isomer 22-B. Upon adsorption of the second NO molecule, it adsorbs simply on the isomer 11-A or B of Au_4NO^-, while maintaining the shape of core Au cluster.

In isomer 22-A and B, two NO molecules adsorbed at the same site with different binding angles to the first NO molecule. Hyponitrite, -O-N=N-O-, is known to have the cis- and trans- structures, and indeed, for the Ar matrix-isolated hyponitrite, it has been suggested to rearrange geometry from the cis-from to the trans-form by annealing.[31]

5.4.3. Au$_4$NO$_2^-$

The IRMPD spectrum of Au$_4$NO$_2^-$ and vibrational spectra of the stable isomers were displayed on Figure 5.6. The IRMPD spectrum exhibits four peaks at least, that is, two broad bands at 1415 and 1325 cm^{-1}, and relatively sharp bands at 825 and 345 cm^{-1}. The former two peaks are undoubtedly assignable to the vibration of small molecule, presumably by NO$_2$. In addition, two tiny bumps around 1035 or 965 cm^{-1} were also appeared.

The DFT results indicate that the molecular adsorption of NO$_2$ on the triangular Au frame are more stable (b, c and e). In isomer 12-A, NO$_2$ molecule attaches via its central nitrogen atom, while isomers 12-B and D have O-end NO$_2$ adsorption. These adsorption forms are well known in the coordination chemistry, where NO$_2$ is known as an ambident ligand. On the other hand, isomer 12-C has NO$_2$ molecule between Au atoms. For Au$_4$NO$_2^-$, only singlet spin state was stable. Stable structure comprising rhombic Au skeleton in the singlet state is >0.38 eV higher than the isomer 12-A in the formation energy (Figure 5.7). The energy difference between N bound isomer A and O bound isomer 12-B was quite small (0.05 eV).

The calculated isomer 12-A has six peaks in 1800-200 cm^{-1}, namely 1488, 1360, 828, 247 and 174 cm^{-1}, accompanied by a relatively small peak of 438 cm^{-1}. The former three bands are mainly due to vibrations of NO$_2$ molecule and are antisymmetric, symmetric and in-plane bending vibrations, respectively. Bending vibration was coupled with symmetric vibration whereas asymmetric vibration has no coupling. These values are quite similar to the vibration of isolated NO$_2$, 1617, 1318 and 750 cm^{-1} which also correspond to antisymmetric, symmetric and bending vibration respectively.[32] A scaling factor for the vibrational wavenumbers can be calculated by comparing the vibrations of the free NO$_2$, and it is 0.95. Hence, the scaled vibrational wavenumbers of isomer 12-A are 1415, 1293 and 788 cm^{-1}. Former two vibrations are redshifted compared with free NO$_2$, probably because electron transfer from gold atoms to the N-O anti-bonding orbital(s) elongates the bond length of N-O (Table 5.1). In contrast the latter bending vibration became blueshifted from that of free NO$_2$ because of coupling with symmetric vibration. The vibrational spectrum of isomer 12-A shows good agreement with the IRMPD spectrum in terms of the band positions at 1488, 1360 and 828 cm^{-1}, although a peak at 438 cm^{-1} is away from the experimental band of 345cm^{-1} by 90 cm^{-1}. Moreover, intensity ratio between 1488 and 1360 cm^{-1} was reversed compared with that of experimental result.

These facts suggesting that $Au_4NO_2^-$ can be composed of not only one isomer 12-A, but also other geometrical isomer(s).

Isomer 12-B to D showed vibrations at significantly different wavenumbers from free NO_2 resulting from asymmetric adsorption forms. Two vibrational peaks appeared between 1000-1600 cm^{-1} for each geometry: 1468 and 1152 cm^{-1} for isomer B, 1502 and 1245 cm^{-1} for isomer C, 1545 and 1041 cm^{-1} for isomer 12-D. Each vibration at the higher wavenumber of each isomer corresponds to the N-O stretching with free O atom, whereas that at the lower wavenumber corresponds to NO vibration with adsorbed O atom on Au. As the result, isomer 12-B could cover the lack of peak assignment by isomer 12-A using its 1468 and 306 cm^{-1} peaks. One of the bump around 1000 cm^{-1} in the experimental result, that is, 1035 or 965 cm^{-1} could be assigned as the secondary peak of isomer B (1152 cm^{-1}). Applying of scaling factor (0.95) decrease this error into 60 cm^{-1}. Hence, isomer 12-A and B are most acceptable geometries in this study.

Most stable geometry of $Au_4NO_2^-$ which has NO_2 dissociatively is shown in Supporting Information (Figure 5.8). This geometry has 1.86 eV higher energy compared to isomer 12-A, and showed intense IR peak at 1597 cm^{-1} due to the NO molecule on bridge site (μ_2).

5.4.4. NO Disproportionation Reaction

Xing and coworkers have suggested that $Au_6(NO)_2^-$ which has two intact NO as the trans-form on same adsorption site of planner Au_6^- exists as the precursor of disproportionation reaction forming $Au_6NO_2^-$.[9] This reaction was observed not only $n = 6$, but also $n = 4$ and 8 in Au_n^-. Hence, an even number of the Au atoms, that is, an odd number of the electrons as anion seems to be important. Even-odd alternation of the vibrational frequency has also been observed for Au_nNO cationic clusters by Rayner and coworkers in which Au_nNO^+ with even number n showed redshifted vibrational frequency than that of odd numbers.[10] This variation is known to be caused by electron transfer into anti-bonding π^* orbital of NO. In the present study, we also observed redshifted NO and NO_2 vibrations compared with free NO and NO_2 for Au_4^- and transfer of electron density from Au_4^- as we discussed in previous section.

We like to discuss disproportionation reaction based on our findings. Geometries determined in each section are depicted in Figure 5.9 in the reaction coordinate. All of the attachment processes are exothermic. First and second NO attachment,

$$Au_4^- + NO \rightarrow Au_4NO^- \qquad\qquad \Delta E = -0.79 \text{ eV} \qquad\qquad (5.1)$$

$$Au_4NO^- + NO \rightarrow Au_4N_2O_2^- \qquad\qquad \Delta E = -0.87 \text{ eV} \qquad\qquad (5.2)$$

occur sequentially without significant reaction barrier. In addition, NO_2 attachment to Au_4^-

$$Au_4^- + NO_2 \rightarrow Au_4NO_2^- \qquad\qquad \Delta E = -2.09 \text{ eV} \qquad\qquad (5.3)$$

is also exothermic. Association of the third NO molecule to $Au_4N_2O_2^-$ results in disproportionation reaction forming $Au_4NO_2^-$ and N_2O as

$$Au_4N_2O_2^- + NO \rightarrow Au_4NO_2^- + N_2O \qquad \Delta E = -2.00 \text{ eV} \qquad\qquad (5.4)$$

This reaction may require activation barrier because the ON-NO bond of $Au_4N_2O_2^-$ ought to be recombined into N- and/or O-end NO_2 of $Au_4NO_2^-$. Once the activation barrier is overcome, disproportionation reaction proceeds forming $Au_4NO_2^-$ followed by NO_2 desorption from $Au_4NO_2^-$. The reaction scheme suggests that reaction condition, presumably, temperature is crucial and under the specific temperature, they could behave as heterogeneous catalyst.

5.5. References

(1)　Haruta, M.; Kobayashi, T.; Sano, H.; Yamada, N. Novel Gold Catalysts for the Oxidation of Carbon Monoxide at a Temperature Far Below 0 °C. *Chem. Lett.* **1987**, *16* (2), 405–408.

(2)　Haruta, M. Gold as a Novel Catalyst in the 21st Century: Preparation, Working Mechanism and Applications. *Gold Bull.* **2004**, *37* (1–2), 27–36.

(3)　Yoon, B.; Häkkinen, H.; Landman, U.; Wörz, A. S.; Antonietti, J.-M.; Abbet, S.; Judai, K.; Heiz, U. Charging Effects on Bonding and Catalyzed Oxidation of CO on Au8 Clusters on MgO. *Science (80-.).* **2005**, *307* (5708), 403–407.

(4)　Lang, S. M.; Bernhardt, T. M. Gas Phase Metal Cluster Model Systems for Heterogeneous Catalysis. *Phys. Chem. Chem. Phys.* **2012**, *14* (26), 9255–9269.

(5)　Socaciu, L. D.; Hagen, J.; Bernhardt, T. M.; Wöste, L.; Heiz, U.; Häkkinen, H.; Landman, U. Catalytic CO Oxidation by Free Au_2^- Experiment and Theory. *J. Am. Chem. Soc.* **2003**, *125*, 10437–10445.

(6)　Wallace, W. T.; Whetten, R. L. Coadsorption of CO and O_2 on Selected Gold Clusters: Evidence for Efficient Room-Temperature CO_2 Generation. *J. Am. Chem. Soc.* **2002**, *124*, 7499–7505.

(7)　Li, X.-N.; Yuan, Z.; He, S.-G. CO Oxidation Promoted by Gold Atoms Supported on Titanium Oxide Cluster Anions. *J. Am. Chem. Soc.* **2014**, *136* (9), 3617–3623.

(8)   Ding, X.; Li, Z.; Yang, J.; Hou, J. G.; Zhu, Q. Theoretical Study of Nitric Oxide Adsorption on Au Clusters. *J. Chem. Phys.* **2004**, *121* (6), 2558–2562.

(9)   Ma, J.; Cao, X.; Chen, M.; Yin, B.; Xing, X.; Wang, X. Low-Temperature Disproportionation Reaction of NO on Au_6^-: A Mechanism Involving Three NO Molecules Promoted by the Negative Charge. *J. Phys. Chem. A* **2016**, *120* (46), 9131–9137.

(10)   Fielicke, A.; Helden, G. Von; Meijer, G.; Simard, B.; Rayner, D. M. Direct Observation of Size Dependent Activation of NO on Gold Clusters. *Phys. Chem. Chem. Phys.* **2005**, *7* (23), 3906–3909.

(11)   Yamaguchi, M.; Mafuné, F. Adsorption and Desorption of NO and NO_2 Molecules on Gold Cluster Anions Observed by Thermal Desorption Spectrometry. *J. Phys. Chem. C* **2019**, *123* (25), 15575–15581.

(12)   Bakker, J. M.; Lapoutre, V. J. F.; Redlich, B.; Oomens, J.; Sartakov, B. G.; Fielicke, A.; von Helden, G.; Meijer, G.; van der Meer, A. F. G. Intensity-Resolved IR Multiple Photon Ionization and Fragmentation of C_{60}. *J. Chem. Phys.* **2010**, *132* (7), 074305.

(13)   Haertelt, M.; J. F. Lapoutre, V.; M. Bakker, J.; Redlich, B.; J. Harding, D.; Fielicke, A.; Meijer, G. Structure Determination of Anionic Metal Clusters via Infrared Resonance Enhanced Multiple Photon Electron Detachment Spectroscopy. *J. Phys. Chem. Lett.* **2011**, *2* (14), 1720–1724.

(14)   Koyama, K.; Nagata, T.; Kudoh, S.; Miyajima, K.; Huitema, D. M. M.; Chernyy, V.; Bakker, J. M.; Mafuné, F. Geometrical Structures of Partially Oxidized Rhodium Cluster Cations, $Rh_6O_m^+$ (*m* = 4, 5, 6), Revealed by Infrared Multiple Photon Dissociation Spectroscopy. *J. Phys. Chem. A* **2016**, *120* (43), 8599–8605.

(15)   Nagata, T.; Kudoh, S.; Miyajima, K.; Bakker, J. M.; Mafuné, F. Adsorption of Multiple NO Molecules on Rh_n^+ (*n* = 6, 7) Investigated by Infrared Multiple Photon Dissociation Spectroscopy. *J. Phys. Chem. C* **2018**, *122* (40), 22884–22891.

(16)   Mafuné, F.; Koyama, K.; Nagata, T.; Kudoh, S.; Yasuike, T.; Miyajima, K.; Huitema, D. M. M.; Chernyy, V.; Bakker, J. M. Structures of Rhodium Oxide Cluster Cations $Rh_7O_m^+$ (*m* = 4–7, 12, 14) Revealed by Infrared Multiple Photon Dissociation Spectroscopy. *J. Phys. Chem. C* **2019**, *123* (10), 5964–5971.

(17) Yamaguchi, M.; Kudoh, S.; Miyajima, K.; Lushchikova, O. V.; Bakker, J. M.; Mafuné, F. Tuning the Dissociative Action of Cationic Rh Clusters Toward NO by Substituting a Single Ta Atom. *J. Phys. Chem. C* **2019**, *123* (6), 3476–3481.

(18) Yamaguchi, M.; Zhang, Y.; Kudoh, S.; Koyama, K.; Lushchikova, O. V.; Bakker, J. M.; Mafuné, F. Oxophilicity as a Descriptor for NO Cleavage Efficiency over Group IX Metal Clusters. *J. Phys. Chem. Lett.* **2020**, *11* (11), 4408–4412.

(19) Frisch, M. J.; Trucks, G. W.; Schlegel, H. B.; Scuseria, G. E.; Robb, M. A.; Cheeseman, J. R.; Scalmani, G.; Barone, V.; Mennucci, B.; Petersson, G. A.; et al. Gaussian 09, Revision E.01. Gaussian 09 2013.

(20) Becke, A. D. Density-Functional Thermochemistry. III. The Role of Exact Exchange. *J. Chem. Phys.* **1993**, *98* (7), 5648–5652.

(21) Lee, C.; Yang, W.; Parr, R. G. Development of the Colle-Salvetti Correlation-Energy Formula into a Functional of the Electron Density. *Phys. Rev. B* **1988**, *37* (2), 785–789.

(22) Hay, P. J.; Wadt, W. R. Ab Initio Effective Core Potentials for Molecular Calculations. Potentials for K to Au Including the Outermost Core Orbitals. *J. Chem. Phys.* **1985**, *82* (1), 299–310.

(23) Ditchfield, R.; Hehre, W. J.; Pople, J. A. Self-Consistent Molecular-Orbital Methods. IX. An Extended Gaussian-Type Basis for Molecular-Orbital Studies of Organic Molecules. *J. Chem. Phys.* **1971**, *54* (2), 724–728.

(24) Hehre, W. J.; Ditchfield, R.; Pople, J. A. Self—Consistent Molecular Orbital Methods. XII. Further Extensions of Gaussian—Type Basis Sets for Use in Molecular Orbital Studies of Organic Molecules. *J. Chem. Phys.* **1972**, *56* (5), 2257–2261.

(25) Andrae, D.; Häußermann, U.; Dolg, M.; Stoll, H.; Preuß, H. Energy-Adjusted Ab Initio Pseudopotentials for the Second and Third Row Transition Elements. *Theor. Chim. Acta* **1990**, *77* (2), 123–141.

(26) McLean, A. D.; Chandler, G. S. Contracted Gaussian Basis Sets for Molecular Calculations. I. Second Row Atoms, Z=11-18. *J. Chem. Phys.* **1980**, *72* (10), 5639–5648.

(27) Krishnan, R.; Binkley, J. S.; Seeger, R.; Pople, J. A. Self-Consistent Molecular Orbital Methods. XX. A Basis Set for Correlated Wave Functions. *J. Chem. Phys.* **1980**, *72* (1), 650–654.

(28)   Bakker, J. M.; Redlich, B.; Van Der Meer, A. F. G.; Oomens, J. Infrared Spectroscopy of Gas-Phase Polycyclic Aromatic Hydrocarbon Cations in the 1050 Mm Spectral Range. *Astrophys. J.* **2011**, *741* (2), 74.

(29)   Furche, F.; Ahlrichs, R.; Weis, P.; Jacob, C.; Gilb, S.; Bierweiler, T.; Kappes, M. M. The Structures of Small Gold Cluster Anions as Determined by a Combination of Ion Mobility Measurements and Density Functional Calculations. *J. Chem. Phys.* **2002**, *117* (15), 6982–6990.

(30)   Santiago-Rodríguez, Y.; Herron, J. A.; Curet-Arana, M. C.; Mavrikakis, M. Atomic and Molecular Adsorption on Au(111). *Surf. Sci.* **2014**, *627*, 57–69.

(31)   Andrews, L.; Zhou, M.; Willson, S. P.; Kushto, G. P.; Snis, A.; Panas, I. Infrared Spectra of Cis and Trans-$(NO)_2^-$ Anions in Solid Argon. *J. Chem. Phys.* **1998**, *109* (1), 177–185.

(32)   Shimanouchi, T. Tables of Molecular Vibrational Frequencies. Consolidated Volume II. *J. Phys. Chem. Ref. Data* **1977**, *6* (3), 993–1102.

Figures
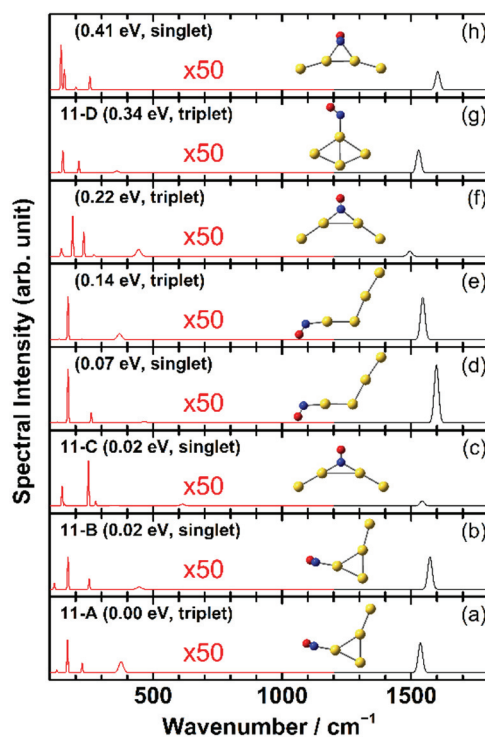
Results using B3LYP
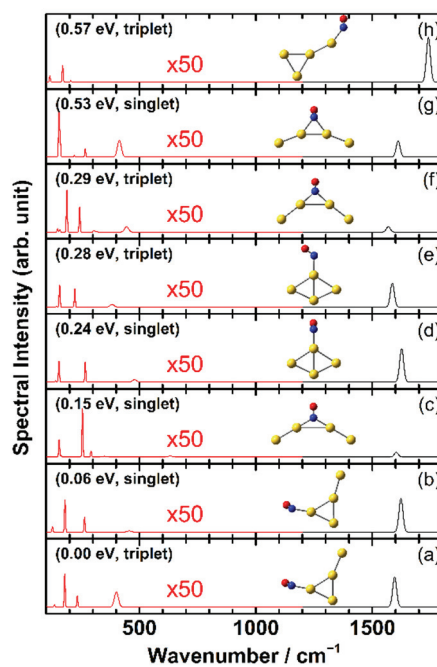
Results using PBE0
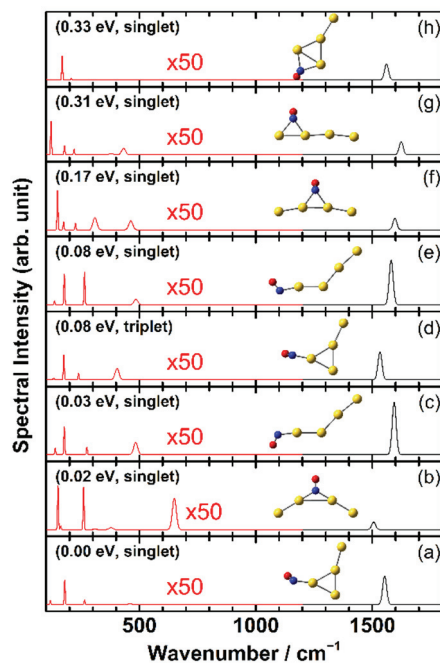
Results using PBE

Figure 5.1. (a−h) Stable isomers of Au_4NO^- and their vibrational spectra obtained by DFT calculations. B3LYP, PBE and PBE0 were used from top to bottom. All of the stable isomers have NO molecule on that geometries regardless of functionals.

86
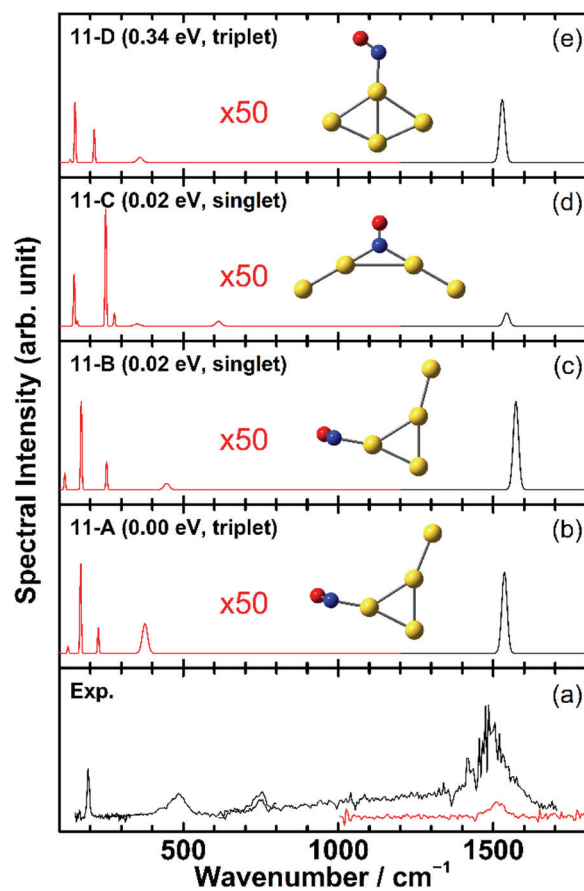
Figure 5.2. (a) IRMPD spectrum for Au_4NO^- and (b-e) DFT calculated spectra for several isomers, with relative energies and spin states shown in parentheses. Blue, red and gold spheres represent N, O, and Au atoms, respectively.
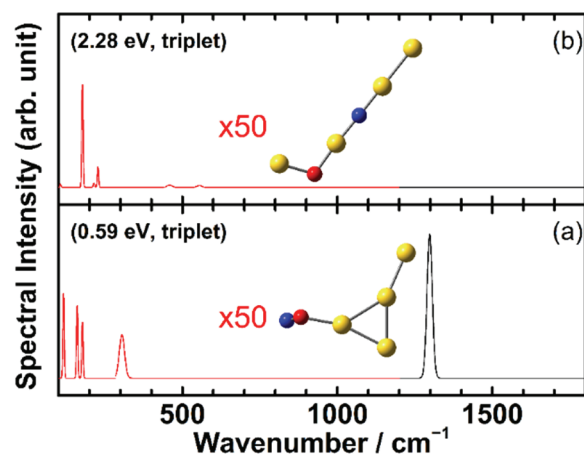
Figure 5.3. Geometrical isomers which have deferent form from stable isomers (Figure **5.1**) are shown. (a) Most stable O-end NO molecule attached and (b) most stable NO dissociated Au4NO⁻. (a) showed intense peak around 1300 cm⁻¹ while N-end geometries possess strong peak around 1500-1700 cm⁻¹. On the other hand, (b) showed no peak over 1000 cm⁻¹ because of absence of small molecule.
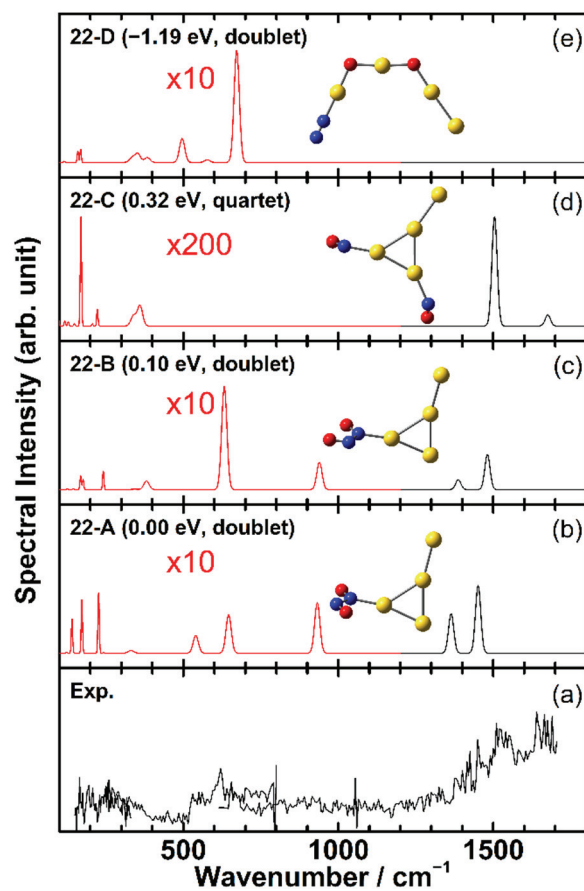
Figure 5.4. (a) IRMPD spectrum for $Au_4N_2O_2^-$ and (b-e) several isomers and its vibrational peaks obtained by DFT calculation were displayed. Relative energy and spin state were shown in the parentheses next to the name label. Blue, red and gold balls represent N, O and Au respectively. Scaling factor was not applied to calculational results.
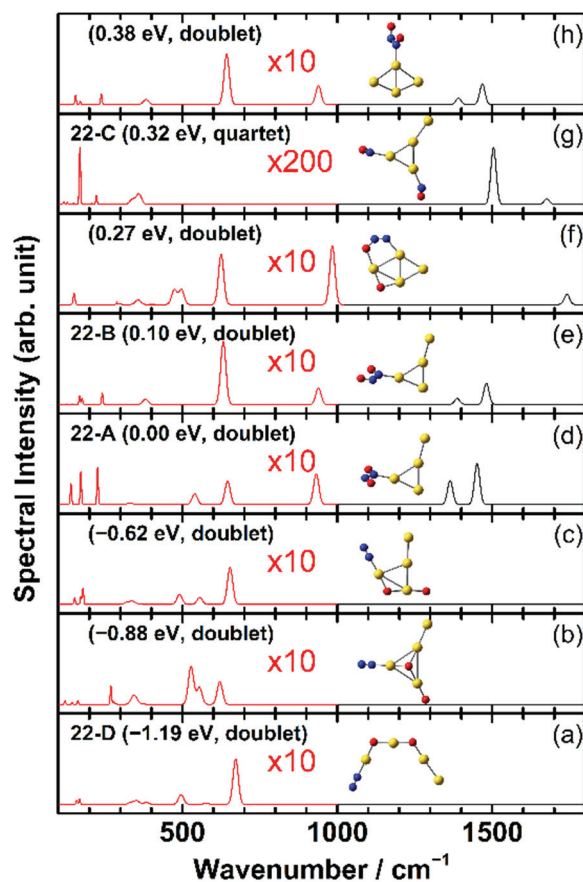
Figure 5.5. (a−h) Stable isomers of $Au_4N_2O_2^-$ and their vibrational spectra obtained by DFT calculations. B3LYP with MWB60 basis set and ECP for Au, and 6-311+G(d) basis set for N and O were employed. Almost all geometries were doublet except for isomer C (g) which has two NO molecules separately. The range of 1300-1600 cm^{-1}, there is no vibrational peak if cluster have no NO molecule.
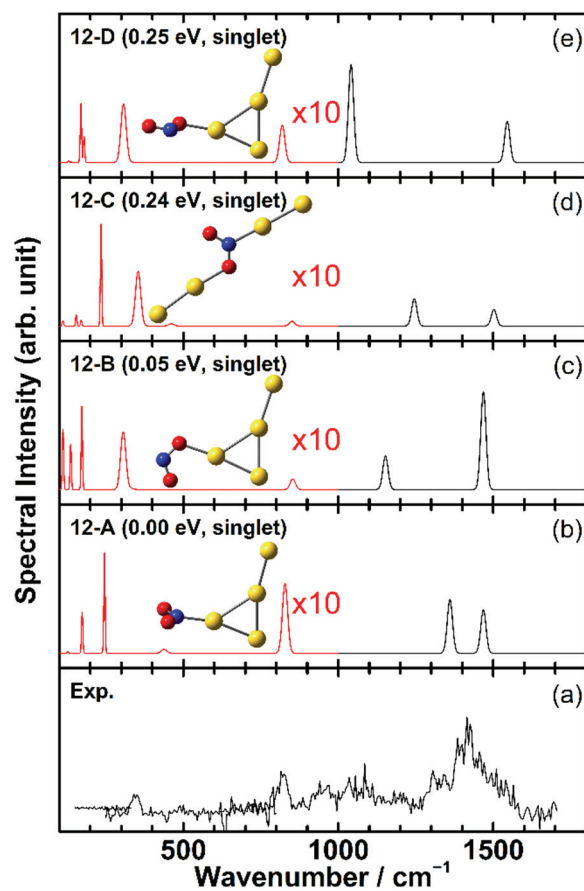
Figure 5.6. (a) IRMPD spectrum for $Au_4NO_2^-$ and (b-e) several isomers and its vibrational peaks obtained by DFT calculation were displayed. Relative energy and spin state were shown in the parentheses next to the name label. Blue, red and gold balls represent N, O and Au respectively. Scaling factor was not applied to calculational results.
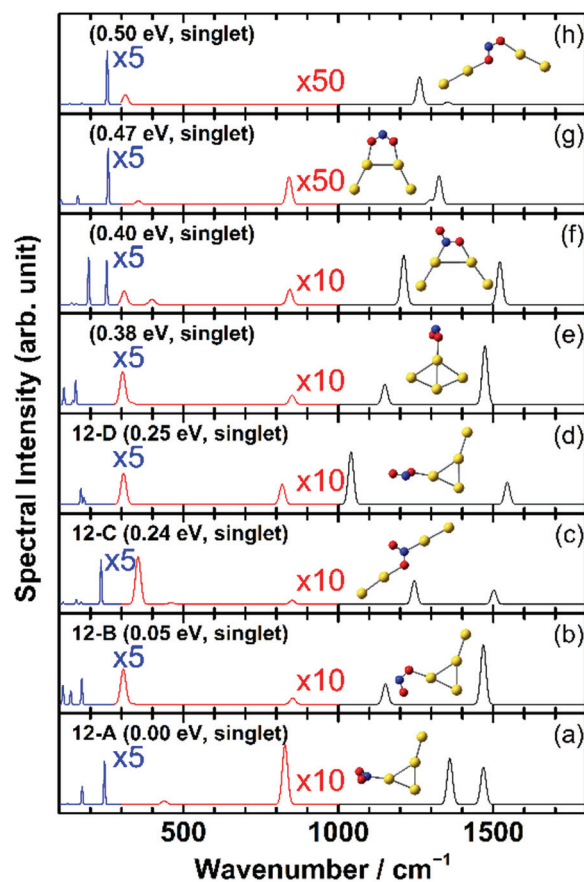
Figure 5.7. (a−h) Stable isomers of $Au_4NO_2^-$ and their vibrational spectra obtained by DFT calculations. B3LYP with MWB60 basis set and ECP for Au, and 6-311+G(d) basis set for N and O were employed. All geometries were singlet. The range of 1000-1600 cm^{-1}, variety of peaks were appeared depending on NO_2 moiety.
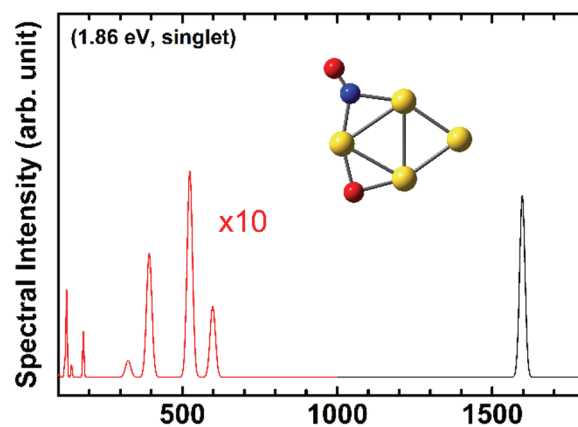
Figure 5.8. Vibrational peaks of geometrical isomer of $AuNO_2^-$ which has dissociated NO_2 and its shape are shown in here. NO_2 was separated in NO molecule and O atom. This energetically unstable isomer possesses NO vibration at $1600cm^{-1}$.
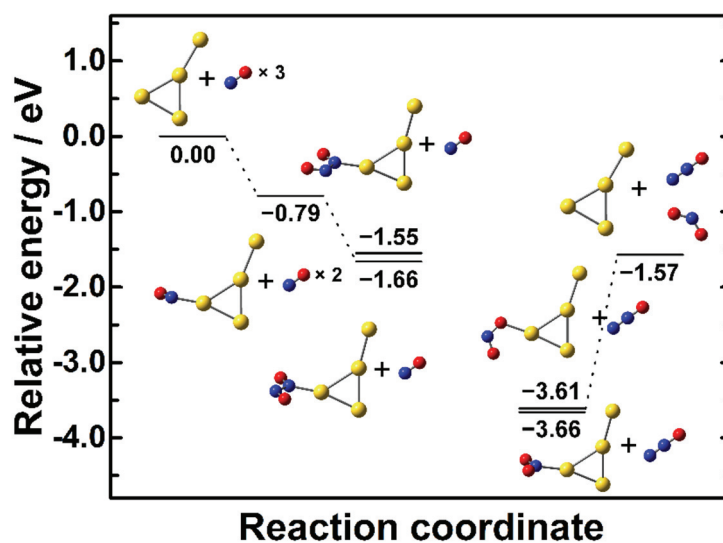
Figure 5.9. Reaction pathway for NO attaching to Au_4^-. Geometries which suggested by present work were displayed with relative energy in eV.

Table 5.1. Wiberg bond index and natural charge on $Au_4NO_2^-$ isomers.

Wiberg bond index and natural charges (unit: *e*) for relevant clusters, isomer 12-A and B are shown.

Isomer 12-A

Wiberg bond index

		1	2	3	4	5	6	7
Au	1	0.00	0.75	0.15	0.05	0.00	0.00	0.00
Au	2	0.75	0.00	0.42	0.28	0.02	0.01	0.01
Au	3	0.15	0.42	0.00	0.48	0.07	0.02	0.02
Au	4	0.05	0.28	0.48	0.00	0.45	0.13	0.13
N	5	0.00	0.02	0.07	0.45	0.00	1.54	1.54
O	6	0.00	0.01	0.02	0.13	1.54	0.00	0.37
O	7	0.00	0.01	0.02	0.13	1.54	0.37	0.00

		Natural charge (e)
Au	1	−0.29
Au	2	−0.13
Au	3	−0.12
Au	4	0.11
N	5	0.29
O	6	−0.43
O	7	−0.43
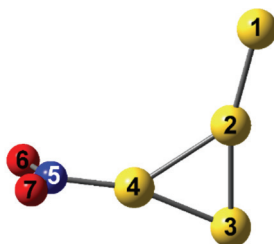
Isomer 12-B

Wiberg bond index

		1	2	3	4	5	6	7
Au	1	0.00	0.75	0.14	0.05	0.00	0.00	0.00
Au	2	0.75	0.00	0.41	0.29	0.01	0.01	0.01
Au	3	0.14	0.41	0.00	0.51	0.02	0.06	0.01
Au	4	0.05	0.29	0.51	0.00	0.14	0.33	0.12
N	5	0.00	0.01	0.02	0.14	0.00	1.38	1.66
O	6	0.00	0.01	0.06	0.33	1.38	0.00	0.29
O	7	0.00	0.01	0.01	0.12	1.66	0.29	0.00

		Natural charge (e)
Au	1	−0.31
Au	2	−0.13
Au	3	−0.10
Au	4	0.14
N	5	0.33
O	6	−0.53
O	7	−0.42
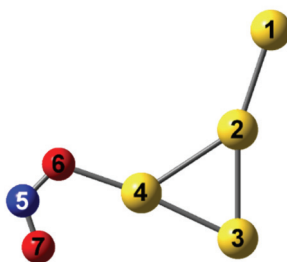
Chapter 6

Tuning the Dissociative Action of Cationic Rh Clusters Toward NO by Substituting a Single Ta Atom

Modification of Rh chemical activity for decomposition of NO by alloying with Ta was studied by vibrational spectroscopy of gas phase clusters, where one single Rh atom was substituted by Ta, with NO adsorbed. While NO adsorbs molecularly on pure Rh clusters, it was found to adsorb dissociatively on Rh_nTa^+ ($n = 2-8$) with the O bound to the Ta on-top site. A reaction path for NO decomposition obtained by DFT calculations for octahedral Rh_5Ta^+ and Rh_6^+ suggests that the Ta oxygen affinity strongly reduces the energy barrier right before bond cleavage, facilitating NO dissociation. The trend is consistent with the Bell–Evans–Polanyi principle. The addition of other less oxophilic dopant atoms could plausibly enhance catalytic reactivity of Rh.

6.1. Introduction

The continuous increase in emission of combustion products harmful to the human respiratory system or planet's heat balance poses a prime challenge for the natural sciences. Mitigation of such detrimental side-effects of economic growth can be promoted by the development of efficient catalysts that can convert harmful emission products into harmless omnipresent atmospheric molecules such as N_2 and O_2. The recent issue involving NO_x emission fraud in the automobile industry serves to underline the need for efficient catalysts for NO reduction.[1] Such catalysts can either be found using screening techniques, or through targeted development based on a thorough understanding of the underlying reaction mechanism, often obtained through careful, controlled reactivity experiments, complemented by quantum-chemical calculations to characterize the energetics of the reaction path. In this work, we present a combined experimental and theoretical study of the adsorption reaction of NO onto isolated clusters of rhodium that are modified through substitution of one single Rh atom by a Ta tom. The substitution dramatically reduces the activation barrier towards NO dissociation, possibly promising a route towards developing more efficient rhodium catalysts.

Rhodium is widely used in catalysts of the three-way converter of automobiles aftertreatment of engine exhaust to reduce NO to N_2.[2] The key step in this process is the dissociative adsorption of NO on the Rh surface, with an activation energy required for the NO bond rupture.[3] As a consequence, the catalysts are in practice used at temperatures exceeding 600 K. At lower temperatures, NO only adsorbs molecularly on the Rh surface.[4–7] An important topic of research is thus to find a method to enhance catalyst reactivity allowing it to function at lower temperature.

Gas phase clusters are a useful model system for nano-catalysts.[8] Reaction mechanisms can be elucidated on the atomic and molecular level, as the reactions can be examined with atomic resolution using mass spectrometry.[9] Three independent studies carried out under collision-free conditions found that, upon reacting two NO molecules with cationic rhodium clusters, N_2 is released, leaving $Rh_n^+O_2$ behind.[10–12] These observations were interpreted as resulting from the dissociative adsorption of NO, generating N atoms that can migrate on the surface of the cluster. However, under thermalized conditions at 300 K, no decomposition of NO was observed, and release of N_2 only takes place at higher temperatures (>700 K),[10] suggesting that the collision-free reaction was driven by heat generated upon NO adsorption;

under thermal reaction conditions, this heat is rapidly dissipated by collisions, and the reaction is throttled.

This throttling was confirmed in our recent study, where we recorded the vibrational spectra of Rh_n^+NO ($n = 6-16$) under near-thermal conditions at 223 K, using infrared multiple-photon dissociation (IRMPD) spectroscopy.[13] A vibrational spectrum is a fingerprint for a molecule or ion, and for Rh_n^+NO it can serve to identify the adsorption form of NO. All clusters studied exhibited intense vibrational bands around 1800 cm^{-1}, characteristic for molecularly adsorbed NO.[13] Concurrent density functional theory (DFT) calculations suggested that dissociation of NO on Rh_n^+ is energetically as stable as molecular adsorption, pointing to the presence of a substantial activation barrier for the NO molecule toward dissociation on Rh_n^+. From these experiments it was concluded that for all Rh clusters studied, the first NO molecule adsorbs in the molecular form at 223 K.

A possible route towards a more efficient catalyst is to tune its reactivity by tailoring its elemental composition to reduce this activation energy barrier. In an earlier work, we proposed the addition of Ta, as it has a strong affinity to both N and O.[14] To investigate the effect of Ta on the adsorption process, we recorded IRMPD spectra for Rh_nTa^+NO ($n = 2-8$) under the same conditions as the previous work on Rh_n^+NO where NO was observed to adsorb intact.[13]

6.2. Experimental Methods

We conducted IRMPD spectroscopic characterization of Rh_nTa^+NO in a molecular beam environment using the free-electron laser for infrared experiments (FELIX) to determine their geometrical structures. As the details of the molecular beam apparatus at FELIX have been described elsewhere,[15] we limit ourselves to the experimental conditions relevant to the present study.

Gas phase Rh_nTa^+-Ar clusters were produced by laser ablation at 532 nm of a 90:10 molar ratio Rh–Ta alloy metal rod (purity: 99.9%; manufactured by Rare Metallic Co., Ltd. upon request) in the presence of an Ar:He mixture (0.47–0.71% Ar) injected into a clustering channel through a pulsed valve (typical length: a few 100 μs) at a stagnation pressure of 0.8 MPa. Downstream from the ablation site, the clusters formed interacted with a NO:He mixture (0.64% NO) pulsed in at 0.1 MPa stagnation pressure through a second valve, forming the Rh_nTa^+NO-Ar product. In the present work, IRMPD spectra of Rh_nTa^+NO were recorded through photodissociation of Rh_nTa^+NO-Ar complexes, because the IR induced detachment of

Ar from $Rh_nTa^+NO–Ar$ is more facile than NO from Rh_nTa^+NO, reducing spectral broadening and other multiple photon effects. Furthermore, attachment of Ar atom does not change the original IR spectrum essentially (Figure 6.1). The $Rh_nTa^+NO−Ar$ complexes were formed in the expansion of the reactive mixture into vacuum, and were enhanced by cooling the clustering region to temperatures of ~200 K using liquid N_2. The clusters beam then passed a 2 mm diameter skimmer to enter a differentially pumped vacuum chamber and was then shaped by a 1 mm diameter aperture to ensure a full overlap with the FELIX IR laser beam. In the present experiment, FELIX was operated at a macropulse repetition rate of 10 Hz in the 100–1800 cm^{-1} spectral range. [15] Typical macropulse energies used here amounted up to 100 mJ, although they were attenuated to <10 mJ above 800 cm^{-1} to avoid spectral saturation. The experiment was operated at 20 Hz allowing for the reference mass spectra to be recorded in between successive FELIX macropulses. Pressures and concentrations of the gases were regulated by Bronkhorst pressure and mass flow controllers for tuning the optimized condition in the series of the experiments. A residual gas analyzer also monitored partial pressures of He, Ar, and NO gases inside the cluster source chamber.

6.3. Computational Methods

To elucidate geometrical structures of Rh_nTa^+NO (n = 2−8), DFT calculations were performed using the Gaussian09 program.[16] Computational steps were almost the same as the previous studies.[13] Every calculation was conducted at 0 K. For Rh_5Ta^+NO, more than one hundred initial geometries, prepared randomly, were calculated using Becke's three-parameter hybrid density functional with the Lee–Yang–Parr correlation functional (B3LYP) for conceivable spin states.[17,18] As basis set for the search, the LANL2DZ basis set and effective core potential (ECP) for Rh and Ta and 6-31G(d) basis sets for N and O atoms were used.[19,20] Selected obtained lower energy isomers were further re-optimized using Stuttgart/Dresden (SDD; MWB28, MWB60) basis sets and ECP for Rh and Ta, and 6-311+G(d) basis sets for N and O; at the same level, harmonic frequencies were calculated.[21]

Vibrational spectra were constructed by convoluting the (unscaled) harmonic frequencies and intensities with a Gaussian line shape functions. To reflect the changing bandwidth of the FEL, the spectral width (full width at half-maximum) was chosen as 5 cm^{-1} in the range 20−300 cm^{-1}. Values of vibrational wavenumbers and IR intensities of all calculated normal modes are available in Table 6.1. For the calculation of the reaction paths,

LANL2DZ for Rh and Ta and 6-31G(d) for N and O were applied. Transition states were calculated using the quadratic synchronous transit-guided quasi-Newton method.[22,23] The obtained intermediate and transition states were re-calculated at the triple zeta level. SDD basis sets and ECP for Rh and Ta and 6-311+G(d) basis sets for N and O were used for single point calculations. The natural bond orbital (NBO) analyses were also performed to evaluate the bond strength.[24,25] The obtained Wiberg bond index (WBI) was used as the bond order in this article.

Harding and coworkers used the Perdew, Burke, and Ernzerhof functional (PBE) with the SDD basis set with ECP for the Rh_6^+ clusters and LANL2DZ as the basis set and ECP for larger Rh_n^+ clusters.[26,27] We compared the vibrational spectra obtained using B3LYP and PBE0 (Figure 6.2, Figure 6.3, Figure 6.4 and Figure 6.5). Interestingly, the differences in the spectra calculated using the two methods are most pronounced for the bare clusters (Figure 6.6 and Figure 6.7); for the structures with NO adsorbed, we find that there are no significant differences depending on the functional (Figure 6.2, Figure 6.3, Figure 6.4 and Figure 6.5). We conclude that the current method is sufficient for structure determination of our systems of interest.

6.4. Results and Discussion

6.4.1. Adsorption of NO on Rh_5Ta^+

Figure 6.8 shows the IRMPD spectrum for Rh_5Ta^+NO-Ar. The spectrum shows several clear and well-resolved bands in the 100–300 cm^{-1} spectral range, and three further bands at 482.5, 710.0 and 940.0 cm^{-1}. Note that the spectrum above 800 cm^{-1} was recorded at substantially reduced laser intensity, to avoid saturation. Crucially, no band is observed in the region between 1600 and 1950 cm^{-1}, the spectral range indicative for intact NO, whether on-top, a bridge or hollow bound. This lack of a band is strong evidence for Rh_5Ta^+NO-Ar having the NO bound dissociatively.

DFT calculations confirm that finding an intact adsorbed NO is unlikely. Above the experimental spectrum, Figure 6.8 shows calculated vibrational spectra of stable isomers with their relative energies and spin multiplicities. Transition-metal clusters are well known to have many isomers which have slightly different shapes and spin states. Our goal is not to be exhaustive in isomeric phase space; rather we aim to understand the binding pattern of NO to a cluster. Hence, we selected several stable isomers with different number of bond(s) between N atom and Rh atom(s) for the comparison, while in each isomer the O atom is bound to the Ta

in on-top configuration. The isomers with 3, 2 and 1 bonds were named 51A (hollow), 51B (bridge) and 51C (terminal) respectively. Only one isomer displayed that, 51D has NO as an intact molecule, and its energy is an enormous 1.72 eV higher than the most stable dissociative complex (Figure 6.8e).

The experimental spectrum agrees quite well with the spectrum of 51A, which is calculated to be most stable (Figure 6.8b). The two bands at 635 and 703 cm^{-1} are associated to motions of the N atom parallel to the plane that three Rh atoms form, while the band at 478 cm^{-1} corresponds to the vibration where the N atom moves perpendicularly to the plane. The strong band at 938 cm^{-1} is due to the stretching vibration of the Ta–O bond. Finally, all bands below 300 cm^{-1} correspond to vibrations of the Rh$_5$Ta$^+$ skeleton. The match between the observed and calculated spectra, both in line positions and IR intensities, undoubtedly suggests that the spectrum recorded is that for an octahedral Rh$_5$Ta$^+$ cluster with the O atom adsorbed on the Ta on-top site and the N atom on one of the Rh hollow sites.

6.4.2. IR spectra of Rh$_n$Ta$^+$NO–Ar (n = 2−8)

To investigate if the dissociative adsorption of NO is common to Rh$_n$Ta$^+$, we examined the spectra of other Rh clusters containing a single Ta atom, Rh$_n$Ta$^+$ (n = 2−8) with one NO and one Ar adsorbed (Figure 6.9). Evidently, the spectra are quite similar to that for Rh$_5$Ta$^+$; no band appears above 1000 cm^{-1}, indicating that NO adsorbs dissociatively on all cluster sizes examined. Indeed, in each spectrum one intense band appears in the 950−1000 cm^{-1} range, which is assigned to the Ta–O stretch vibration (Figure 6.2, Figure 6.3, Figure 6.4, Figure 6.5 and Table 6.1). The appearance of this intense band is consistent with the dissociative adsorption of NO. Examining the size dependence closely, it was found that the band is slightly blueshifted by ~50 cm^{-1} going from n = 2 to 3, but remains essentially unchanged for $n \geq 3$ (Figure 6.10). The slight shift in frequency is due to a change in the Ta–O bond strength, manifested by the Wiberg bond index (1.97 and 1.86 for n = 2 and 3, respectively).

Bands related the Rh–N–Rh motion also appear around 635 cm^{-1} in the spectra, which are relatively stable in frequency for n = 2−4, but exhibit a redshift by 140 cm^{-1} going from n = 4 to n = 5, suggesting a possible structural change (see Figure 6.10). Comparison of DFT calculated spectra with the observed IRMPD spectra for n = 2−8 (Figure 6.2, Figure 6.3, Figure 6.4 and Figure 6.5) indicates that the O atom always adsorbs on the on-top site of Ta, and that

the N atom adsorbs on a bridge site between two Rh atoms for $n = 2$ and 3, and on a hollow site of Rh atoms for $n \geq 5$ (Figure 6.11). For $n = 4$, a transitional structure is found; based on the spectral wavenumber, the N atom is considered to adsorb on the bridge site; the bond length between N and three Rh atoms (1.89, 1.90 and 1.90 Å) and visual inspection suggest that it is approaching adsorption on the hollow site. Thus, the observed size dependence appears to indicate that the N atom favors a hollow site formed by three Rh atoms non-adjacent to the Ta atom. As no such hollow site exists below $n = 4$, the N atom adsorbs on the bridge site. DFT calculations for Rh_5Ta^+ further suggest that adsorption of the N atom on the bridge and on-top sites would be less favorable by +0.65 and +1.72 eV, respectively (see Figure 6.8). In our previous work, we also found a preference of the N atom for a hollow site on Rh_n^+ ($n = 6$, 8−10).[13]

6.4.3. Reaction Pathway for Dissociation of NO on Rh_5Ta^+

Rh_6^+ was previously found to have an octahedral geometry;[26] the current experimental spectrum suggests that Rh_5Ta^+ has the similar octahedral structure (see Figure 6.6 and Figure 6.7), with one of the Rh atoms replaced by a Ta atom. What makes Rh_5Ta^+ then more active than Rh_6^+? For this, we calculated possible reaction paths for the dissociation of NO on Rh_5Ta^+ and compared them to the same reaction over Rh_6^+ (Figure 6.12). For Rh_5Ta^+, all stable structures are in either triplet or quintet states except for IM1, which is 0.1 eV more stable on the septet surface than on the triplet surface. All species displayed in the reaction pathway are in the triplet state, although for species IM5 on Figure 6.12 and IM2 on Figure 6.13, the quintet state is lower in energy than the triplet state. In all cases, this difference is lower than 0.2 eV.

For Rh_5Ta^+, the NO molecule is considered to initially adsorb on the Ta on-top site of the cluster through the N atom because of higher binding energy (2.18 eV) compared with energy of NO adsorbing on Rh (1.93 eV). N-bound on-top adsorption at the Ta atom is calculated to be favored over O-bound adsorption (0.52 eV): The orientation is common to the adsorption of small, N-containing molecules on metal surfaces.[28–32] According to the natural charges of atoms in Table 6.2, the charge is mainly localized on the Ta atom (natural charge +0.97e) while Rh atoms are very slightly negatively charged except for the Rh atom, that is, located at the diametrical opposite side of the Ta atom (+0.15e). Upon adsorption of NO, all Rh atoms become positively charged and the N (−0.15e) and O (−0.10e) atoms are negatively

charged, suggesting that electron density is donated to the π* antibonding orbital of NO. Indeed, the NO bond is slightly elongated from 1.15 to 1.18 Å upon adsorption.

After adsorption, the NO molecule migrates to a hollow site (IM2) and subsequently to a bridge site (IM3). NO leans toward the Ta (TS3) until the O atom bounds to it (IM4). The NO bond is ruptured after passing TS4 with the energy barrier of 0.65 eV, forming separate O and N atoms. The energy of this transition state is 1.08 eV lower than that of the initial state. The activation energies in the reaction path are low enough that Rh_5Ta^+NO can readily overcome the barriers, with the energy obtained upon adsorption of NO. The final product is stabilized by 3.90 eV with respect to the reactants.

For Rh_6^+, a similar reaction path had previously been proposed (see Figure 6.12);[10] N-bound on-top adsorption on Rh_6^+ is exothermic by 1.72 eV. Subsequently, the NO molecule migrates to a bridge site, leaning toward a Rh atom until the O atom in NO binds to it. However, the transition state for bond cleavage is located quite high, forming a +2.16 eV energy barrier relative to the entrance complex. The energy of this transition state is 0.68 eV higher than that of the initial state, which prevents NO from dissociating.

In contrast, for all reaction paths found for Rh_5Ta^+ (Figure 6.12 and Figure 6.13), adsorption of the O atom on the Ta on-top site is exothermic by more than 3 eV with respect to the reactants. This is because of higher oxygen affinities of Ta-containing clusters. Dissociation energies of diatomic RhO^+ and TaO^+ are 3.02 and 7.01 eV respectively, measured by Armentrout and co-workers[33,34]. In the present work, the binding energy of the O atom to Rh_5Ta^+ on its on-top site of the Ta atom is higher by 3.00 eV than that to Rh_6^+ (see Figure 6.14). This strongly enhanced stabilization by the oxide binding lowers the activation barrier for dissociation of NO. This reaction thus forms a textbook example for the Bell–Evans–Polanyi principle,[35] predicting reduction of the activation energy with the decrease in the formation energy of the product species. The current work thus convincingly demonstrates that the targeted elemental tailoring of Rh catalyst material is possible by substituting oxophilic elements, as Ta can strongly reduce the barrier for NO dissociation. It can of course be expected that Ta is too oxophilic, leading to catalyst poisoning, and that other less oxophilic elements provide a better balance between reduction of the barrier toward dissociation and O binding strength. Further studies of doped Rh cluster systems to investigate such and other effects, eventually aimed at elucidating a full catalytic NO reduction cycle, are currently underway.

6.5. Conclusions

Adsorption forms of a single NO molecule on gas phase metal cluster cations, Rh_nTa^+ ($n = 2-8$), were investigated by IRMPD spectroscopy using an IR free-electron laser. Rh, commonly used as a reducing catalyst of NO in a three-way converter, is found to be activated for decomposition of NO by addition of a single Ta atom: while NO adsorbs molecularly on pure Rh clusters, it was found to adsorb dissociatively on Rh_nTa^+ ($n = 2-8$) with the O atom on the Ta atom in on-top configuration. The bands relating to motion of the N atom also appear in the spectra, indicating that the N atom adsorbs on a bridge site between two Rh atoms for $n = 2$ and 3, and on a hollow site of Rh atoms for $n \geq 5$.

Reaction pathways for NO decomposition were calculated for Rh_5Ta^+ and Rh_6^+ to understand what makes Rh_5Ta^+ more active than Rh_6^+. For Rh_6^+, the transition state for bond cleavage is located quite high, forming a +0.68 eV energy barrier relative to the initial state. This high activation barrier prevents NO from dissociating. In contrast, for Rh_5Ta^+NO, the activation energies in the reaction path are low enough that Rh_5Ta^+NO can readily overcome the barriers, with the energy gained upon adsorption of NO. Ta oxygen affinity strongly reduces the energy barrier right before bond cleavage, facilitating NO dissociation. The trend is consistent to the Bell–Evans–Polanyi principle. While tantalum's oxophilicity may overshoot its intended purpose and could arguably lead to rapid catalyst poisoning, the addition of other less oxophilic dopant atoms could plausibly enhance reactivity of Rh.

6.6. References

(1)   Schiermeier, Q. The Science behind the Volkswagen Emissions Scandal. *Nature* **2015**, https://doi.org/10.1038/nature.2015.18426.

(2)   Shimokawabe, M.; Umeda, N. Selective Catalytic Reduction of NO by CO over Supported Iridium and Rhodium Catalysts. *Chem. Lett.* **2004**, *33* (5), 534–535, https://doi.org/10.1246/cl.2004.534.

(3)   Hendershot, R. E.; Hansen, R. S. Reduction of Nitric Oxide with Carbon Monoxide on the Rh(100) Single-Crystal Surface. *J. Catal.* **1986**, *98* (1), 150–165, https://doi.org/10.1016/0021-9517(86)90305-2.

(4)   Castner, D. G.; Sexton, B. A.; Somorjai, G. A. LEED and Thermal Desorption Studies of Small Molecules (H_2, O_2, CO, CO_2, NO, C_2H_4, C_2H_2 and C) Chemisorbed on the Rhodium (111) and (100) Surfaces. *Surf. Sci.* **1979**, *83* (1), 60–82, https://doi.org/10.1016/0039-6028(79)90480-1.

(5)   Villarrubia, J. S.; Ho, W. Nitric Oxide Adsorption, Decomposition, and Desorption on Rh(100). *J. Chem. Phys.* **1987**, *87* (1), 750–764, https://doi.org/10.1063/1.453573.

(6)   Kao, C.-T.; Blackman, G. S.; Van Hove, M. A.; Somorjai, G. A.; Chan, C.-M. The Surface Structure and Chemical Reactivity of Rh(111)-(2 × 2)-3NO by HREELS and Dynamical LEED Analysis. *Surf. Sci.* **1989**, *224* (1–3), 77–96, https://doi.org/10.1016/0039-6028(89)90902-3.

(7)   Siokou, A.; van Hardeveld, R. M.; Niemantsverdriet, J. W. Surface Reactions of Nitrogen Oxide on Rhodium (100), Adsorption, Dissociation and Desorption. *Surf. Sci.* **1998**, *402–404*, 110–114, https://doi.org/10.1016/S0039-6028(97)00935-7.

(8)   Johnson, G. E.; Mitrić, R.; Bonačić-Koutecký, V.; Castleman, A. W. Clusters as Model Systems for Investigating Nanoscale Oxidation Catalysis. *Chem. Phys. Lett.* **2009**, *475* (1–3), 1–9, https://doi.org/10.1016/J.CPLETT.2009.04.003.

(9)   Lang, S. M.; Bernhardt, T. M. Gas Phase Metal Cluster Model Systems for Heterogeneous Catalysis. *Phys. Chem. Chem. Phys.* **2012**, *14* (26), 9255–9269, https://doi.org/10.1039/c2cp40660h.

(10)   Tawaraya, Y.; Kudoh, S.; Miyajima, K.; Mafuné, F. Thermal Desorption and Reaction of NO Adsorbed on Rhodium Cluster Ions Studied by Thermal Desorption Spectroscopy. *J. Phys. Chem. A* **2015**, *119* (31), 8461–8468, https://doi.org/10.1021/acs.jpca.5b04224.

(11)   Anderson, M. L.; Ford, M. S.; Derrick, P. J.; Drewello, T.; Woodruff, D. P.; Mackenzie, S. R. Nitric Oxide Decomposition on Small Rhodium Clusters, $Rh_n^{+/-}$. *J. Phys. Chem. A* **2006**, *110*, 10992–11000, https://doi.org/10.1021/JP062178Z.

(12)   Hirabayashi, S.; Ichihashi, M. Effects of Second-Metal (Al, V, Co) Doping on the NO Reactivity of Small Rhodium Cluster Cations. *J. Phys. Chem. A* **2017**, *121* (13), 2545–2551, https://doi.org/10.1021/acs.jpca.6b11613.

(13)   Nagata, T.; Koyama, K.; Kudoh, S.; Miyajima, K.; Bakker, J. M.; Mafune, F. Adsorption Forms of NO on Rh_n^+ ($n = 6−16$) Revealed by Infrared Multiple Photon Dissociation Spectroscopy. *J. Phys. Chem. C* **2017**, *121* (49), 27417–27426, https://doi.org/10.1021/acs.jpcc.7b08097.

(14)   Mafuné, F.; Tawaraya, Y.; Kudoh, S. Reactivity Control of Rhodium Cluster Ions by Alloying with Tantalum Atoms. *J. Phys. Chem. A* **2016**, *120* (6), 861–867, https://doi.org/10.1021/acs.jpca.5b11898.

(15)   Kiawi, D. M.; Bakker, J. M.; Oomens, J.; Buma, W. J.; Jamshidi, Z.; Visscher, L.; Waters, L. B. F. M. Water Adsorption on Free Cobalt Cluster Cations. *J. Phys. Chem. A* **2015**, *119* (44), 10828–10837, https://doi.org/10.1021/acs.jpca.5b07119.

(16)   Frisch, M. J.; Trucks, G. W.; Schlegel, H. B.; Scuseria, G. E.; Robb, M. A.; Cheeseman, J. R.; Scalmani, G.; Barone, V.; Mennucci, B.; Petersson, G. A.; Nakatsuji, H.; CT, W.; et al. Gaussian 09, Revision E.01. Gaussian 09 2013.

(17)   Becke, A. D. Density-Functional Thermochemistry. III. The Role of Exact Exchange. *J. Chem. Phys.* **1993**, *98* (7), 5648–5652, https://doi.org/10.1063/1.464913.

(18)   Lee, C.; Yang, W.; Parr, R. G. Development of the Colle-Salvetti Correlation-Energy Formula into a Functional of the Electron Density. *Phys. Rev. B* **1988**, *37* (2), 785–789, https://doi.org/10.1103/PhysRevB.37.785.

(19)   Hay, P. J.; Wadt, W. R. Ab Initio Effective Core Potentials for Molecular Calculations. Potentials for K to Au Including the Outermost Core Orbitals. *J. Chem. Phys.* **1985**, *82* (1), 299–310, https://doi.org/10.1063/1.448975.

(20)   Ditchfield, R.; Hehre, W. J.; Pople, J. A. Self-Consistent Molecular-Orbital Methods. IX. An Extended Gaussian-Type Basis for Molecular-Orbital Studies of Organic Molecules. *J. Chem. Phys.* **1971**, *54* (2), 724–728, https://doi.org/10.1063/1.1674902.

(21)   Andrae, D.; Häußermann, U.; Dolg, M.; Stoll, H.; Preuß, H. Energy-Adjusted Ab Initio Pseudopotentials for the Second and Third Row Transition Elements. *Theor. Chim. Acta* **1990**, *77* (2), 123–141, https://doi.org/10.1007/BF01114537.

(22)   Peng, C.; Bernhard Schlegel, H. Combining Synchronous Transit and Quasi-Newton Methods to Find Transition States. *Isr. J. Chem.* **1993**, *33* (4), 449–454, https://doi.org/10.1002/ijch.199300051.

(23)   Peng, C.; Ayala, P. Y.; Schlegel, H. B.; Frisch, M. J. Using Redundant Internal Coordinates to Optimize Equilibrium Geometries and Transition States. *J. Comput. Chem.* **1996**, *17* (1), 49–56, https://doi.org/10.1002/(SICI)1096-987X(19960115)17:1<49::AID-JCC5>3.0.CO;2-0.

(24)   Reed, A. E.; Weinstock, R. B.; Weinhold, F. Natural Population Analysis. *J. Chem. Phys.* **1985**, *83* (2), 735–746, https://doi.org/10.1063/1.449486.

(25)   Glendening, E. D.; Reed, A. E.; Carpenter, J. E.; Weinhold, F. NBO Version 3.1.

(26)   Harding, D. J.; Gruene, P.; Haertelt, M.; Meijer, G.; Fielicke, A.; Hamilton, S. M.; Hopkins, W. S.; Mackenzie, S. R.; Neville, S. P.; Walsh, T. R. Probing the Structures of Gas-Phase Rhodium Cluster Cations by Far-Infrared Spectroscopy. *J. Chem. Phys.* **2010**, *133* (21), 214304, https://doi.org/10.1063/1.3509778.

(27)   Perdew, J. P.; Ernzerhof, M.; Burke, K. Rationale for Mixing Exact Exchange with Density Functional Approximations. *J. Chem. Phys.* **1998**, *105* (22), 9982, https://doi.org/10.1063/1.472933.

(28)   Parry, I. S.; Kartouzian, A.; Hamilton, S. M.; Balaj, O. P.; Beyer, M. K.; Mackenzie, S. R. Collisional Activation of N_2O Decomposition and CO Oxidation Reactions on Isolated Rhodium Clusters. *J. Phys. Chem. A* **2013**, *117* (36), 8855–8863, https://doi.org/10.1021/jp405267p.

(29)   Zeigarnik, A. V. Adsorption and Reactions of N_2O on Transition Metal Surfaces. *Kinet. Catal.* **2003**, *44* (2), 233–246, https://doi.org/10.1023/A:1023308629868.

(30)   Hermes, A. C.; Hamilton, S. M.; Hopkins, W. S.; Harding, D. J.; Kerpal, C.; Meijer, G.; Fielicke, A.; Mackenzie, S. R. Effects of Coadsorbed Oxygen on the Infrared Driven Decomposition of N_2O on Isolated Rh_5^+ Clusters. *J. Phys. Chem. Lett.* **2011**, *2* (24), 3053–3057, https://doi.org/10.1021/jz2012963.

(31)   Hamilton, S. M.; Hopkins, W. S.; Harding, D. J.; Walsh, T. R.; Gruene, P.; Haertelt, M.; Fielicke, A.; Meijer, G.; Mackenzie, S. R. Infrared Induced Reactivity on the

Surface of Isolated Size-Selected Clusters: Dissociation of N₂O on Rhodium Clusters. *J. Am. Chem. Soc.* **2010**, *132* (5), 1448–1449, https://doi.org/10.1021/ja907496c.

(32) Watanabe, K.; Kokalj, A.; Horino, H.; Rzeznicka, I. I.; Takahashi, K.; Nishi, N.; Matsushima, T. Scanning-Tunneling Microscopy, Near-Edge X-Ray-Absorption Fine Structure, and Density-Functional Theory Studies of N₂O Orientation on Pd(110). *Jpn. J. Appl. Phys.* **2006**, *45* (3B), 2290–2294, https://doi.org/10.1143/JJAP.45.2290.

(33) Chen, Y.; Armentrout, P. B. Kinetic Energy Dependence of the Reactions of Ru⁺, Rh⁺, Pd⁺, and Ag⁺ with O₂. *J. Chem. Phys.* **1995**, *103* (2), 618–625, https://doi.org/10.1063/1.470095.

(34) Hinton, C. S.; Citir, M.; Manard, M.; Armentrout, P. B. Collision-Induced Dissociation of MO⁺ and MO₂⁺ (M = Ta and W): Metal Oxide and Dioxide Cation Bond Energies. *Int. J. Mass Spectrom.* **2011**, *308* (2–3), 265–274, https://doi.org/10.1016/J.IJMS.2011.06.011.

(35) Evans, M. G.; Polanyi, M. Inertia and Driving Force of Chemical Reactions. *Trans. Faraday Soc.* **1938**, *34*, 11–24, https://doi.org/10.1039/tf9383400011.
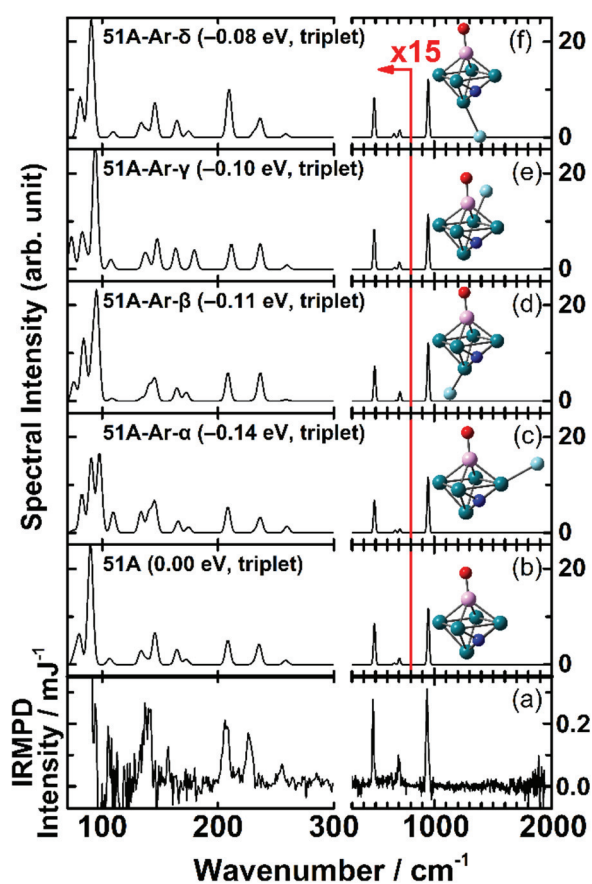
Figures

Figure 6.1. (a) IRMPD spectrum of $Rh_5Ta^+NO–Ar$. (b) Vibrational spectrum of Rh_5Ta^+NO and (c–f) vibrational spectra of $Rh_5Ta^+NO–Ar$. Attachment of an Ar atom doesn't affect IR spectrum significantly.
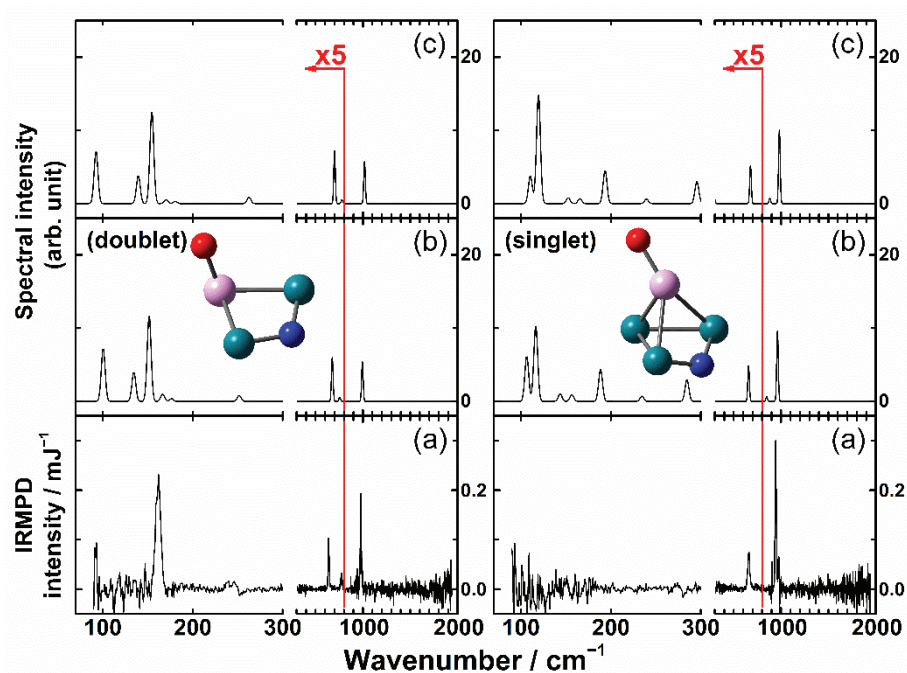
Figure 6.2. (a) IRMPD spectra of $Rh_2Ta^+NO–Ar$ and $Rh_3Ta^+NO–Ar$. Vibrational spectra of the lowest energy isomer found for Rh_2Ta^+NO and Rh_3Ta^+NO using (b) B3LYP and (c) PBE0 using the TZ level.
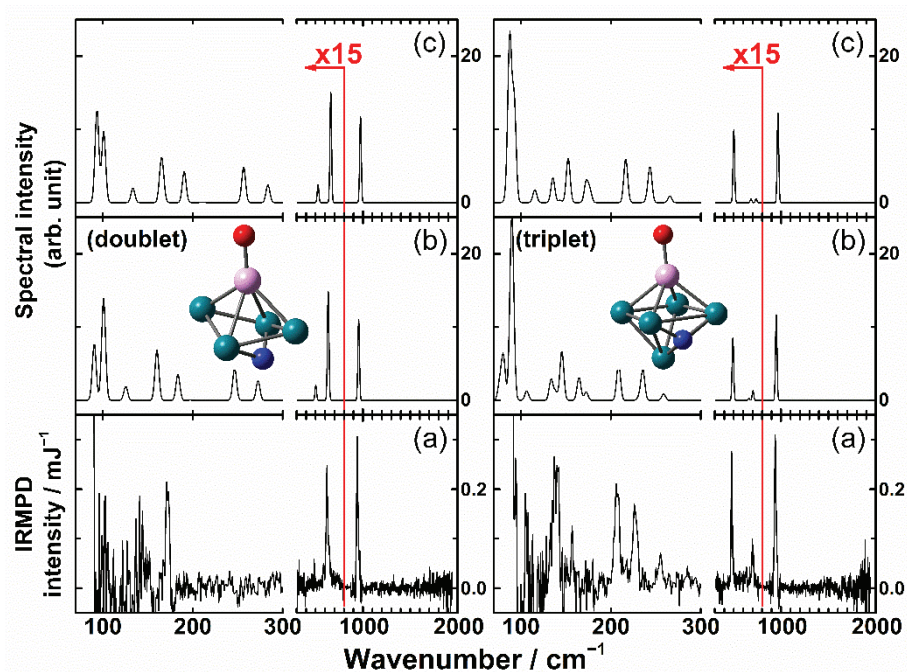
Figure 6.3. (a) IRMPD spectra of $Rh_4Ta^+NO–Ar$ and $Rh_5Ta^+NO–Ar$. Vibrational spectra of the lowest energy isomer found for Rh_4Ta^+NO and Rh_5Ta^+NO using (b) B3LYP and (c) PBE0.

111
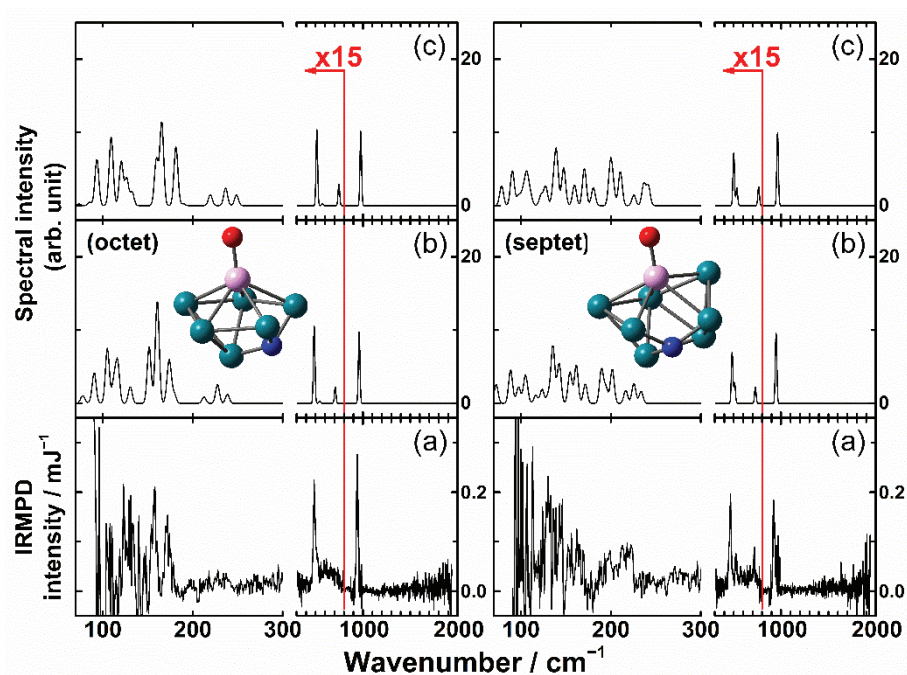
Figure 6.4. (a) IRMPD spectra of $Rh_6Ta^+NO–Ar$ and $Rh_7Ta^+NO–Ar$. Vibrational spectra of the lowest energy isomer found for Rh_6Ta^+NO and Rh_7Ta^+NO using (b) B3LYP and (c) PBE0.
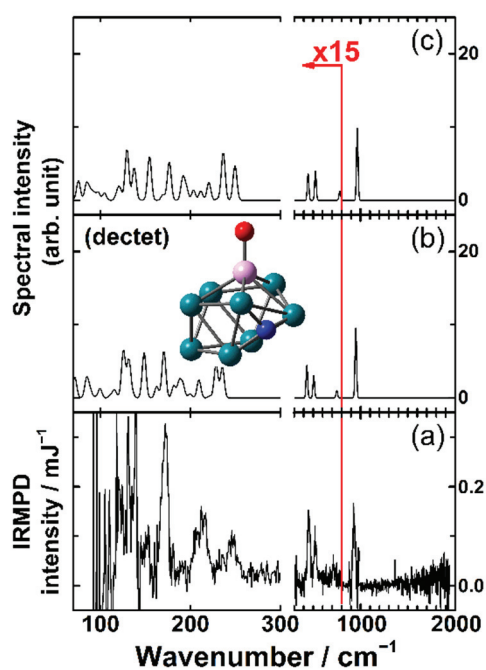
Figure 6.5. (a) IRMPD spectrum of $Rh_8Ta^+NO–Ar$. Vibrational spectra of the lowest energy isomer found for Rh_8Ta^+NO using (b) B3LYP and (c) PBE0.
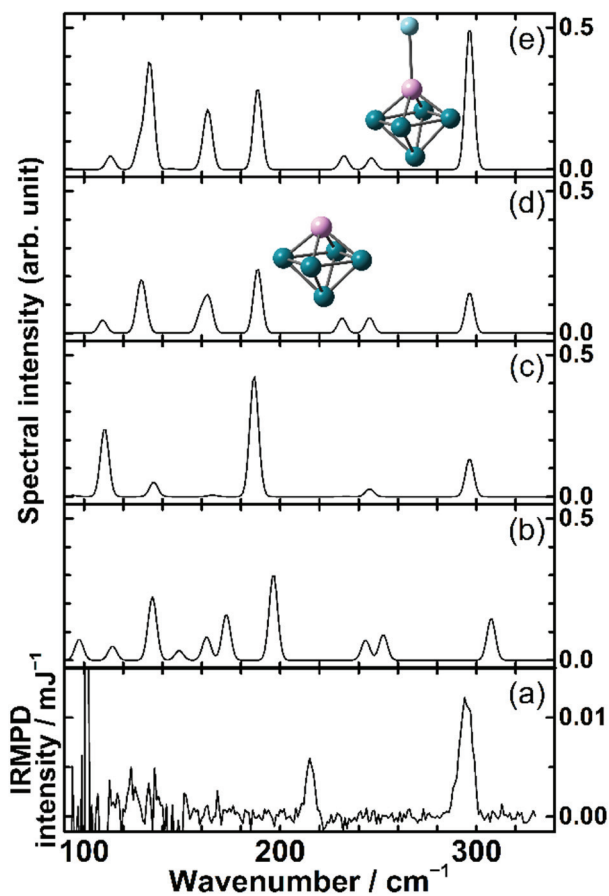
Figure 6.6. (a) IRMPD spectrum of Rh_5Ta^+–Ar. (b–e) Vibrational spectra of octahedral Rh_5Ta^+ obtained by computational calculations using (b) PBE0, (c) B3LYP constrained to C_{2v} symmetry, (d) B3LYP and (e) B3LYP with Ar tagging. SDD and 6-311+G(d) are used for every optimization (TZ level). Attachment of an Ar atom doesn't affect IR spectrum significantly.
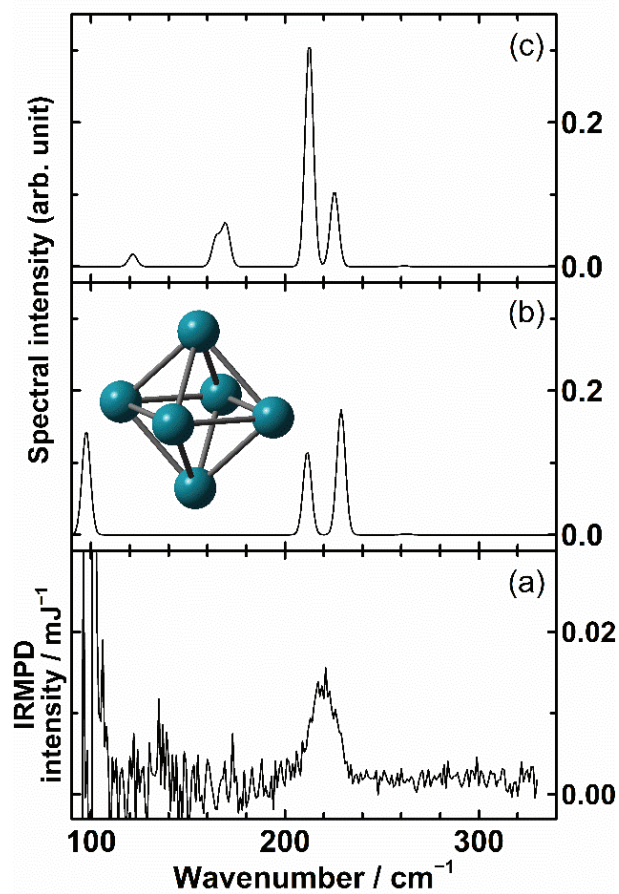
Figure 6.7. (a) IRMPD spectrum of $Rh_6{}^+$–Ar. (b,c) Vibrational spectra of octahedral $Rh_6{}^+$ obtained by computational calculations using (b) PBE0 and (c) B3LYP. The present result is consistent to the previous result by Harding et al.[26]
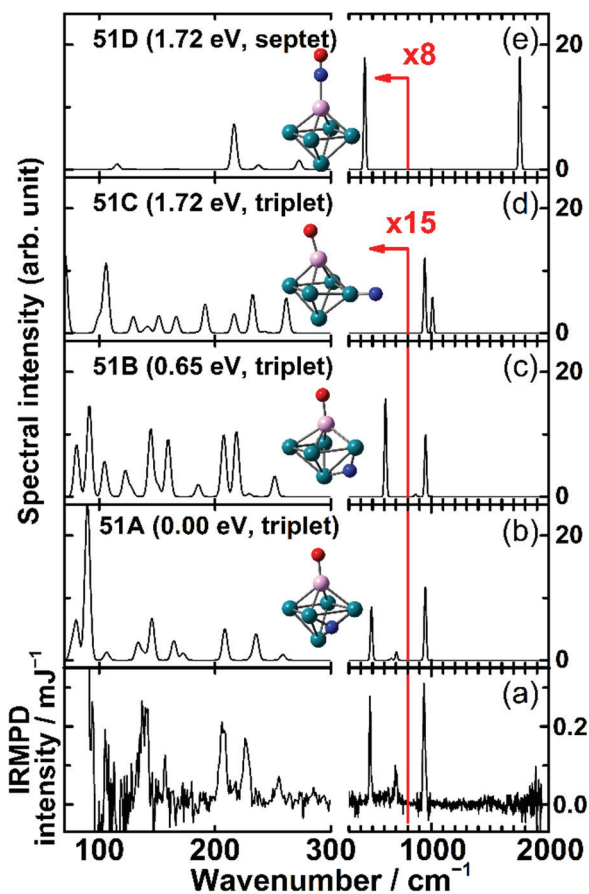
Figure 6.8. (a) IRMPD spectrum for Rh_5Ta^+NO-Ar and (b−e) DFT calculated vibrational spectra of stable isomers of Rh_5Ta^+NO. At frequencies below 800 cm^{-1} the experimental and calculated spectra are multiplied by the indicated factors to enhance visibility of the relatively weak bands at lower wavenumbers. For each structure (where Rh is color-coded dark-cyan, Ta pink, N blue and O red), the relative formation energy and spin multiplicity are shown in parentheses. Calculated IR intensities and frequencies of the harmonic vibrations underlying the calculated spectra are given in Table 6.1.
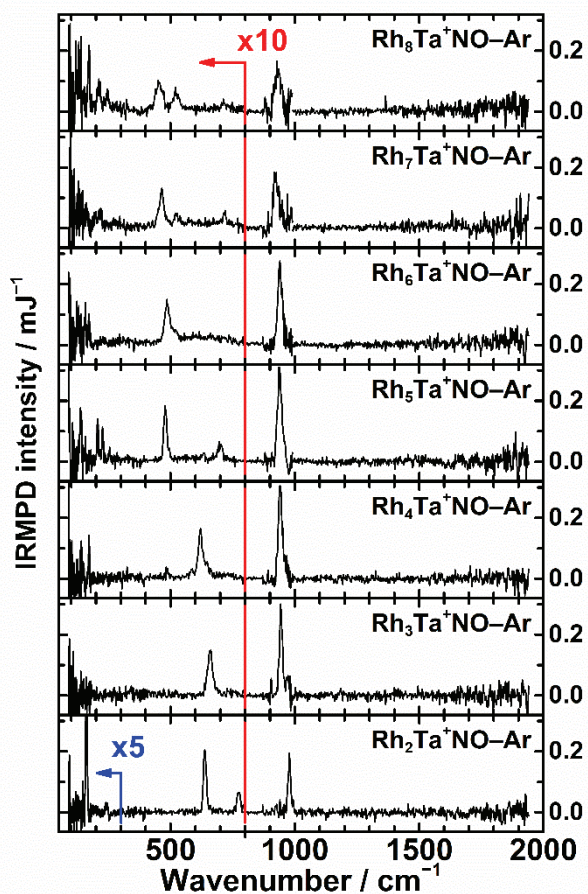
Figure 6.9. Observed IRMPD spectra of $Rh_nTa^+NO–Ar$ ($n = 2−8$). Multiplication factors (in red and blue) applied to the lower frequency range, as described for Figure 6.8.
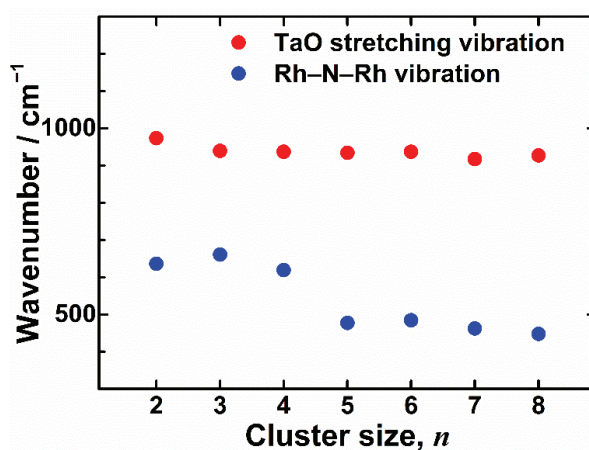
Figure 6.10. Experimental results on the wavenumbers of vibrations involving O and N atoms in $Rh_nTa^+NO–Ar$ as a function of the cluster size, n.
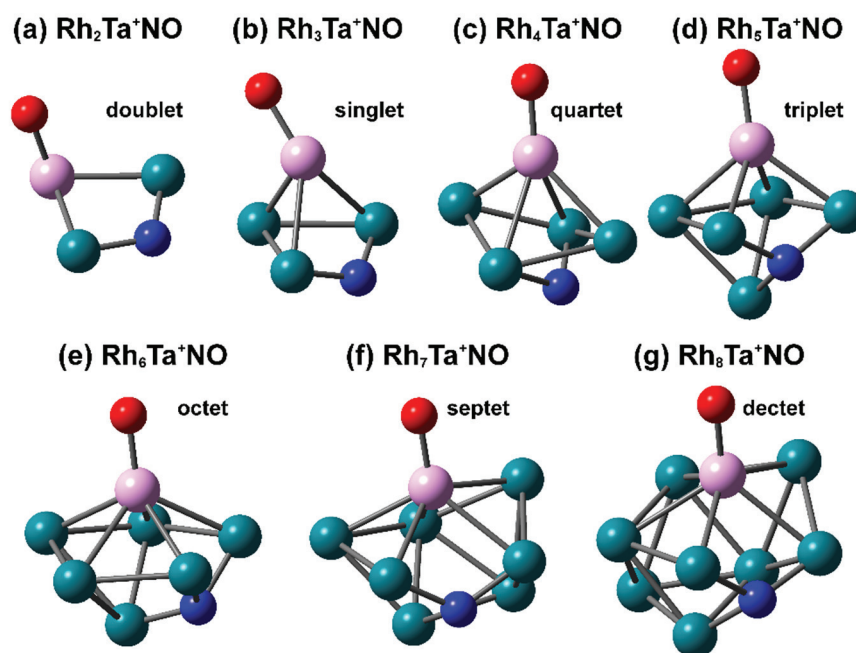
Figure 6.11. Geometrical structures of Rh$_n$Ta$^+$NO (n = 2−8) determined based on IRMPD spectroscopy and DFT calculations. Dark-cyan, pink, blue and red balls represent Rh, Ta, N and O atoms, respectively.
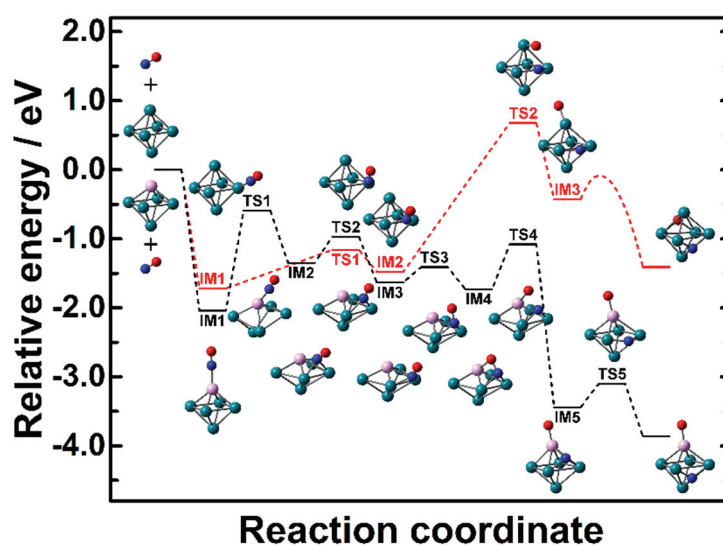
Figure 6.12. A reaction path for the dissociation of NO on Rh$_5$Ta$^+$ (black) and on Rh$_6$$^+$(red). The reaction crosses from the septet to the triplet surface after IM1. Details of the energies and spin states are available in Table 6.3.
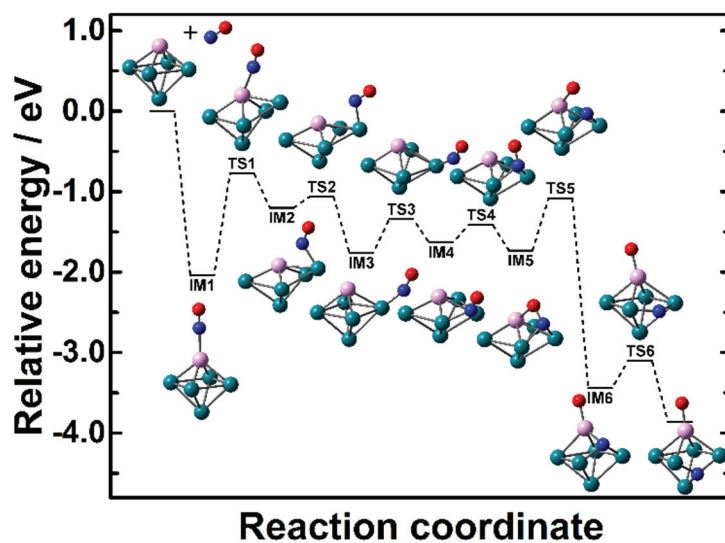
Figure 6.13. Another reaction path for the dissociation of NO on Rh_5Ta^+. To explore the reaction path, LANL2DZ and 6-31G(d) were used for initial optimization. The energies were obtained by the single point calculation with TZ level based on the optimized geometries.
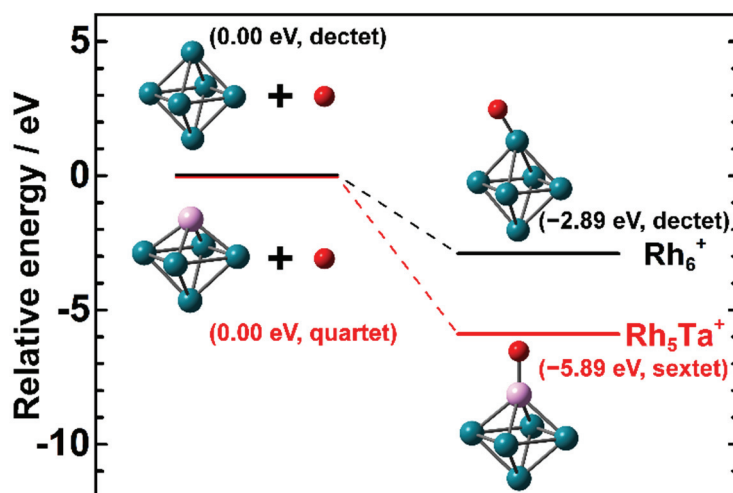
Figure 6.14. Comparison of the O binding energies to Rh_5Ta^+ and Rh_6^+ clusters. B3LYP with SDD and 6-311+G(d) were used for optimization.

Table 6.1. Vibrational wavenumbers and IR Spectral intensities for Rh_nTa^+NO clusters.

Obtained IR spectra for Rh_nTa^+NO (n = 2–8) are written below. B3LYP with TZ level optimization was used for every calculation.

Rh_2Ta^+NO doublet

	Wavenumbers / cm^{-1}	IR Intensities / 10^3 km mol^{-1}
1	100.9065	7.8244
2	134.8629	4.3125
3	151.0377	12.7006
4	166.1360	1.0718
5	176.8323	0.4055
6	251.2765	0.8883
7	675.9746	25.4403
8	755.0647	2.4955
9	994.0865	115.1917

Rh_3Ta^+NO singlet

	Wavenumbers / cm^{-1}	IR Intensities / 10^3 km mol^{-1}
1	39.7595	8.7237
2	106.1516	6.6675
3	116.8582	11.1763
4	143.3608	1.1063
5	156.9936	1.0033
6	189.0028	4.7427
7	199.0579	0.0033
8	234.9981	0.7735
9	284.0769	3.1968
10	656.9272	20.7369
11	846.8700	14.0414
12	962.4964	204.1554

Rh$_4$Ta$^+$NO quartet

	Wavenumbers / cm^{-1}	IR Intensities / 10^3 km mol^{-1}
1	23.4264	9.0000
2	90.3624	2.7708
3	100.1522	3.0146
4	101.3878	2.0749
5	125.6797	0.6873
6	159.2136	0.8722
7	160.3967	1.6525
8	183.8938	1.2736
9	197.1425	0.0171
10	246.1608	1.5888
11	272.3816	0.9626
12	501.9679	2.9352
13	628.5133	0.6456
14	632.7607	20.5773
15	955.2571	235.3890

Rh$_5$Ta$^+$NO 51A(hollow) triplet

	Wavenumbers / cm^{-1}	IR Intensities / 10^3 km mol^{-1}
1	76.7979	0.8636
2	80.5728	2.1333
3	89.2139	5.4561
4	90.2850	3.9422
5	106.0831	0.4652
6	133.0603	1.0187
7	138.2227	0.4084
8	145.2053	2.4138
9	164.2276	1.1252
10	172.5476	0.4071
11	208.1409	1.8043
12	231.8243	0.1768
13	235.9670	1.4833
14	258.4059	0.3200
15	491.0474	12.0722
16	659.7746	0.4256
17	702.6682	1.8824
18	949.5290	249.5104

Rh$_5$Ta$^+$NO 51B(bridge) triplet

	Wavenumbers / cm^{-1}	IR Intensities / 10^3 km mol^{-1}
1	57.0499	0.5397
2	80.9798	3.0178
3	91.8524	5.2856
4	104.2935	1.9331
5	107.9680	0.2341
6	123.0049	1.4829
7	127.4941	0.5026
8	144.5052	3.9258
9	150.9860	0.6664
10	159.4053	3.3270
11	185.6370	0.7011
12	207.2401	3.5894
13	218.2333	3.7852
14	229.1941	0.1661
15	251.9098	1.1766
16	610.0258	22.2839
17	865.2409	8.8780
18	950.7024	211.0962

Rh$_5$Ta$^+$NO 51C(terminal) triplet

	Wavenumbers / cm^{-1}	IR Intensities / 10^3 km mol^{-1}
1	59.6970	11.1597
2	70.3722	4.5322
3	99.8217	0.8857
4	104.8772	1.3795
5	106.5502	2.9885
6	129.2692	0.9472
7	139.8522	0.1665
8	142.1207	0.3087
9	151.6895	1.0171
10	166.2069	0.9574
11	184.6760	0.0523
12	191.0752	1.6673
13	216.9977	1.1207
14	232.5779	2.2346
15	242.5358	0.0965
16	261.2482	2.0189
17	943.5876	256.8902
18	1009.7466	122.2174

Rh$_5$Ta$^+$NO 51D(mol at O) septet

	Wavenumbers / cm^{-1}	IR Intensities / 10^3 km mol^{-1}
1	43.3893	0.4423
2	43.5010	0.4416
3	102.6650	0.0000
4	115.5508	0.2918
5	115.5846	0.2917
6	125.9852	0.0626
7	141.6121	0.0000
8	162.2662	0.0287
9	162.3140	0.0287
10	164.9274	0.0000
11	216.6000	1.6767
12	216.6210	1.7321
13	216.6679	1.5459
14	237.9330	0.2377
15	237.9457	0.2392
16	272.3696	0.9842
17	434.4677	47.6513
18	1752.7824	385.4630

Rh$_5$Ta$^+$NO 51E(mol at N) septet

	Wavenumbers / cm^{-1}	IR Intensities / 10^3 km mol^{-1}
1	15.2488	0.0131
2	31.7155	0.0631
3	79.5937	0.0618
4	104.9075	0.2332
5	115.8061	0.3063
6	118.0986	0.0057
7	120.4628	0.4923
8	140.2105	0.4923
9	145.3449	1.2610
10	175.8399	0.1919
11	187.7959	1.2657
12	237.0959	0.0081
13	238.0854	1.0920
14	263.1743	11.6928
15	273.4364	1.6163
16	298.9280	1.2384
17	516.6219	0.1855
18	1880.6756	1835.0299

Rh$_6$Ta$^+$NO octet

	Wavenumbers / cm^{-1}	IR Intensities / 10^3 km mol^{-1}
1	76.8490	0.1780
2	78.8933	0.2445
3	86.3677	0.0812
4	90.3421	1.4983
5	104.6172	1.0383
6	105.4320	1.7087
7	112.1450	1.1066
8	116.2054	1.9834
9	130.2416	0.8159
10	151.4927	2.7973
11	160.9300	5.0549
12	172.8199	0.8624
13	174.0485	1.4917
14	179.9491	0.4421
15	212.1145	0.3090
16	227.4135	0.9177
17	238.5537	0.4450
18	485.0091	15.0634
19	544.2833	0.5077
20	706.8559	3.1607
21	960.1153	207.3661

Rh$_7$Ta$^+$NO septet

	Wavenumbers / cm^{-1}	IR Intensities / 10^3 km mol^{-1}
1	72.6095	0.9283
2	88.4528	1.6454
3	93.8994	0.0954
4	97.8077	0.7894
5	104.2085	1.0003
6	106.9336	0.5164
7	116.6107	0.3911
8	123.4152	0.6893
9	130.3872	0.4358
10	135.6082	2.8267
11	142.9431	1.9762
12	154.1087	1.5454
13	161.9227	1.8844
14	171.5773	0.9543
15	189.3895	1.6864
16	194.6251	0.7611
17	201.9066	1.6722
18	216.0506	0.6458

19	225.6503	0.9909
20	233.9755	0.5950
21	483.5162	9.9597
22	510.2265	3.8456
23	727.6801	3.1911
24	946.8197	204.8984

Rh$_8$Ta$^+$NO dectet

	Wavenumbers / cm^{-1}	IR Intensities / 10^3 km mol^{-1}
1	71.3739	1.0225
2	84.3361	0.8486
3	85.8381	0.1256
4	88.3929	0.3727
5	93.8839	0.0485
6	99.6841	0.4553
7	111.8953	0.1254
8	115.3258	0.3835
9	119.3463	0.0293
10	125.6904	2.3051
11	131.9245	1.8407
12	135.2564	0.1926
13	148.7488	2.2287
14	162.5477	0.5638
15	170.2976	2.2925
16	181.1056	0.6009
17	187.6842	0.7817
18	191.7591	0.6518
19	199.3151	0.2029
20	209.6867	0.8889
21	221.4283	0.0972
22	228.2017	1.6625
23	235.9839	1.4924
24	432.6907	6.3067
25	506.5047	4.3683
26	748.6127	1.4077
27	950.0047	203.7698

Table 6.2. Natural Bond Charges.

The natural bond orbital (NBO) analyses were conducted to evaluate the bond strength. The variations of the natural bond charges by the NO adsorption can be seen in the table below.
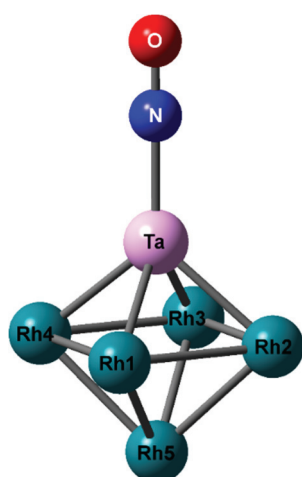
Rh_5Ta^+ quartet

	Charge / e
Rh1	−0.03141
Rh2	−0.02794
Rh3	−0.02796
Rh4	−0.03139
Rh5	0.14566
Ta	0.97304
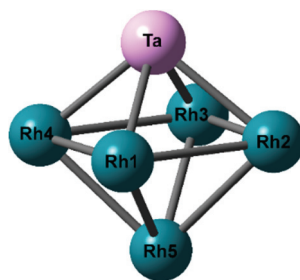
Rh_5Ta^+NO 51D(mol at O) septet

	Charge / e
Rh1	0.05919
Rh2	0.05924
Rh3	0.05921
Rh4	0.05923
Rh5	0.18475
Ta	1.21551
N	−0.14501
O	−0.10028

Rh$_5$Ta$^+$NO 51A(hollow) triplet

	Charge / e
Rh1	0.25845
Rh2	0.25850
Rh3	0.03683
Rh4	0.03679
Rh5	0.37700
Ta	1.21551
N	−0.46009
O	−0.72301
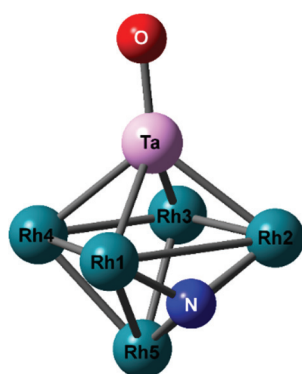
Table 6.3. Energy values along the reaction paths.

      Energies of the species appearing along the reaction paths displayed on Figure 6.12 and Figure 6.13 are shown below. In the table, "R" and "P" mean "Reactant" and "Product", respectively.

$Rh_5Ta^+ + NO$ (Figure 6.12, black line)

	Energy / eV	Spin state
R	0.00	4
IM1	−2.04	3
TS1	−0.59	3
IM2	−1.35	3
TS2	−0.97	3
IM3	−1.63	3
TS3	−1.41	3
IM4	−1.73	3
TS4	−1.08	3
IM5	−3.44	3
TS5	−3.10	3
P	−3.86	3

$Rh_5Ta^+ + NO$ (Figure 6.13)

	Energy / eV	Spin state
R	0.00	4
IM1	−2.04	3
TS1	−0.77	3
IM2	−1.20	3
TS2	−1.06	3
IM3	−1.76	3
TS3	−1.34	3
IM4	−1.63	3
TS4	−1.41	3
IM5	−1.73	3
TS5	−1.08	3
IM6	−3.44	3
TS6	−3.10	3
P	−3.86	3

Rh$_6^+$ + NO (Figure 6.12, red line)

	Energy / eV	Spin state
R	0.00	10
IM1	−1.72	9
TS1	−1.16	9
IM2	−1.48	9
TS2	0.68	9
IM3	−0.43	9
P	−1.41	5

Chapter 7

Oxophilicity as a Descriptor for NO Cleavage Efficiency over Group IX Metal Clusters

Iridium and rhodium are group IX elements that can both catalytically reduce NO. To understand the difference in their reactivity towards NO, the adsorption forms of NO onto clusters of Ir and Rh are compared using vibrational spectra, recorded via infrared multiple-photon dissociation spectroscopy. The spectra give evidence for the existence of at least two specific adsorption forms. The main Ir_6^+NO isomer is one in which NO is dissociated, whereas one other is a local minimum structure in the reaction pathway leading to dissociative adsorption. In contrast to adsorption onto Rh_6^+, where less than 10% of the isomeric population was found in the global minimum associated with dissociative adsorption, a substantial fraction (about 50%) of NO dissociates on Ir_6^+. This higher efficiency is attributed to a considerably reduced activation barrier for dissociation on Ir_6^+. The characteristic key identified for dissociation efficiency is the cluster's affinity to atomic oxygen.

7.1. Main Contents

Iridium and rhodium are group IX elements, that can both catalytically reduce NO.[1,2] As a consequence, both have been used in three-way catalytic converters in the aftertreatment system of automobiles,[3] and the reaction mechanism of NO reduction over these metals has been studied intensively for a few decades. The adsorption forms of NO on extended surfaces are known to be sensitive to surface morphology and coverage: at coverages of less than 0.25 ML NO on Rh(111), adsorption is preferential on hollow (fcc) sites, but this preference shifts to on-top sites at coverages between 0.25 and 0.50 ML.[4–7] For Ir(111) this is reversed: NO adsorbs on on-top sites at low coverage and only populates hollow sites at higher coverage.[8] In addition, on planar Ir(210) NO adsorbs on on-top sites, whereas on faceted Ir (210) it occupies bridge and on-top sites. Faceted Ir(210) has been demonstrated to be active toward NO decomposition even under 0.70 ML coverage by O atoms.[9]

As the reaction efficiency sensitively varies with reaction conditions, the use of a gas-phase cluster to investigate the largely unknown reaction mechanism can be very instructive, because clusters and molecules involved in the reaction can be probed with atomic detail using mass spectrometry,[10–14] providing scientific insights for creating state of the art nano-catalysis or for tuning them. Moreover, the combination with infrared (IR) spectroscopy allows structure determination of (intermediate) adsorption products allowing for the validation of proposed reaction mechanisms.

Recently, we elucidated the adsorption form of NO on cationic Rh clusters, Rh_n^+ ($n = 6-16$), using IR multiple-photon dissociation (IRMPD) spectroscopy combined with density functional theory (DFT) calculations.[15–19] The spectra show that NO molecules predominantly adsorb on on-top sites of Rh_n^+ for all n studied, and that only a small fraction of NO adsorbs dissociatively on Rh_n^+, with the precise ratio of dissociative to molecular adsorption depending on the cluster size n. For Rh_6^+, almost all NO adsorbs molecularly on the on-top site of the Rh_6^+ octahedron. Although the DFT calculations predict that dissociative adsorption of NO is thermodynamically favored over molecular (intact) adsorption for Rh_6^+, they also show that this is kinetically hindered by the activation barrier for NO cleavage, corroborating the rather low observed NO dissociation.

To understand what is the main factor that causes the relative height of this barrier, we here investigate the adsorption of NO on a cluster of a second group IX element. We probe the structure of Ir_6^+NO using IR photodissociation spectroscopy of complexes with Ar, $Ir_6^+NO\text{-}Ar_m$,

and observe the release of Ar atoms as a probe of vibrational excitation. Figure 7.1 shows the IRMPD spectrum for $Ir_6^+NO\text{-}Ar_m$ (panel a) and calculated spectra of three stable isomers (panels b-d), of which two exhibit separate binding of N and O atoms to Ir_6^+, and only one has NO as an intact molecule. The most stable isomer A (panel b), is an octahedral Ir_6^+ cluster with the N and O atoms on opposite on-top sites. Two other stable isomers are prismatic Ir_6^+ clusters with molecular NO on an on-top site (isomer B, panel c), or with the O atom on an on-top site and the N atom on a bridge site, respectively (isomer C, panel d).

The experimental IRMPD spectrum is dominated by relatively strong bands at 355, 375, 563, 940, and 1805 cm^{-1}, with weaker bands at 450, 603, and 1045 cm^{-1}. The 1805 cm^{-1} band is substantially broader than the lower frequency bands, even taking into account the larger spectral bandwidth of the IR laser at higher frequencies (approx. 0.5% of the central frequency FWHM); it thus appears likely that this band is saturated. A band observed at this frequency is characteristic for an intact NO molecule through its stretching vibration: for NO adsorbed on an on-top site of Ir(111) this frequency is 1860 cm^{-1}.[20] As shown in Figure 7.1(c), isomer B contains an intact NO molecule and exhibits a strong band around 1900 cm^{-1}. The maximum depletion observed for this band is 40-50%, suggesting that this is due to only one of multiple isomers present in the beam, and that the other isomers carry no intact NO, and consequently do not lose Ar at these frequencies. This experimental band thus indicates that at least a fraction of the population sampled has NO molecularly adsorbed on Ir_6^+. Consistent with this, the predicted vibrational spectrum of isomer B exhibits no bands in the 600−1800 cm^{-1} spectral region, so this isomer alone cannot explain the pronounced band at 940 cm^{-1} and the weaker band at 1045 cm^{-1} observed experimentally. In contrast, bands at such frequencies are predicted for isomer A with O and N atoms adsorbed separately on on-top sites; calculated at 980 and 1130 cm^{-1}, respectively, they correspond to stretching vibrations of the terminal O and N atoms, respectively. The bands observed at 563, 450, and 355 or 375 cm^{-1} are consistent with isomer B. Thus, the IRMPD spectrum agrees favorably with a combination of vibrational spectra of isomers A and B, leaving only the bands at 603 and 355 or 375 cm^{-1} unaccounted for. These two bands are likely due to one or more further isomers, of which we found a large number (cf. Figure 7.2), and one of these is isomer C. Other prismatic Ir_6^+ isomers with the O atom on the on-top site and the N atom on a different bridge site could be possible, but they typically exhibit a band or bands at >620 cm^{-1} (see Figure 7.2). In summary, we conclude that the spectrum is

due to the co-existence of three structural isomers, with both molecular and dissociative adsorption present.

If we assume that the band intensity in the IRMPD spectrum is proportional to the product of the calculated vibrational band spectral intensity and the relative isomeric population, the latter can be estimated to be approximately 25% and 60% for isomers A and B, respectively, with a possible further 15% for a third isomer, for instance isomer C. This estimate is consistent with the observed depletion on the order of 40−50 % at 1805 cm^{-1}.

The question arises whether the presence of these isomers can be rationalized based on a possible reaction pathway. Figure 7.3 shows a reactive potential energy surface (PES) for the adsorption and subsequent dissociation of NO on Ir_6^+ on the quintet PES. For Ir_6^+, we found a prism to be the global minimum structure with sextet multiplicity. Since isomer B, one of the lowest energy prismatic Ir_6^+ isomers with NO molecularly adsorbed, is found on the quintet surface, we restricted our reaction pathway search to this surface. The NO molecule initially adsorbs on an on-top site of Ir_6^+ through the N atom with a binding energy of 2.32 eV (IM1). This orientation is common to small, N-containing molecules on metal surfaces.[21,22] After adsorption, the NO molecule leans towards a neighboring Ir atom until the O atom is bound to it (IM2). The NO bond is ruptured after passing TS2, forming separately adsorbed O and N atoms (IM3). The N atom then migrates to the next Ir atom via a bridge site (IM4) to end up as a terminal N (IM5). Finally, Ir_6^+ transforms from prism to octahedron (P). The whole reaction path is downhill, and all barriers are below the energy of the reactants (R), thus the reaction is kinetically favored. However, as the internal energy of the cluster can be dissipated by thermalizing collisions with the surrounding carrier gas atoms during the reaction, each transition state can be a barrier which halts the successive reaction step, leaving population in the intermediate state. Indeed, isomers B and C correspond to intermediates IM1 and IM4 respectively, en route to the final product A. The highest barrier, TS2, is 0.26 eV below R; More than a half of the clusters were not able to cross this barrier and were observed as isomer B.

The found fraction of at least 50% isomers with NO dissociated (A and C) for Ir_6^+, is in stark contrast with Rh_6^+ where molecularly adsorbed NO is strongly dominant.[15] To understand this difference, we first compare the calculated reactive PESs. The reactive PES for NO dissociation over Rh_6^+ was found to be quite similar to that for Ir_6^+:[23] After on-top adsorption of NO on Rh_6^+, the NO molecule migrates to a bridge site, leaning toward a Rh atom until the O atom binds to it. However, the transition state for bond cleavage on Rh_6^+ is located 0.7 eV

higher than the reactants. This activation barrier thus prevents NO dissociation over Rh_6^+. In contrast, for Rh_5Ta^+, on which NO was observed to dissociate with near-unity efficiency, the transition state for bond cleavage is located 1.1 eV *lower* than the reactants. Thus, the activation barrier for bond cleavage, where the O is abstracted towards another metal atom, is critically important for dissociation of NO, and its relative height appears to be decisive for successful NO cleavage.

But what then underlies these relative barrier heights? For this, we examine the structural preferences for adsorption. We first note that the global minima, where NO is dissociatively bound to Rh_6^+ and Ir_6^+, respectively, are markedly distinct: where for Ir_6^+ both N and O are adsorbed on on-top sites (evidenced by the experimental band at 940 cm^{-1}), for Rh_6^+ both are located on hollow sites. This preference seems reflected in the transition state structures for both species (Figure 7.4) when NO undergoes bond cleavage: for Ir_6^+, N-bound on-top adsorption is retained even in the transition state structure, forming an Ir-N-O-Ir chain structure. On Rh_6^+, the N cannot retain its position on a hollow site, but still prefers bridge adsorption in the transition state. This propensity for Rh_6^+ to bind N on a bridge motif is seen throughout the reactive PES, with the exception of the entrance complex;[12] Ir exhibits on-top binding throughout the reaction pathway. These findings strongly correlate to the experimental findings for the low-coverage regime on (111) surfaces of Rh and Ir.[4] From this, we conclude that the adsorption of NO onto clusters is essentially the same as for the bulk, thereby establishing clusters as a useful model system for the adsorption, and potentially for the reduction reaction.

Separate N and O atoms can stably adsorb on on-top sites of the Ir cluster. This is also found computationally by Zhou *et al.*, who report that up to three O atoms adsorb on-top on pyramidal Ir_5^+.[24] The propensity of on-top adsorption is further reflected in the relatively high energy of formation of an isomer with O and N atoms on bridge sites of Ir_6^+ (+0.71 eV).

However, the key binding preference is not that for N, but for O. The structural characteristic common to all three transition states shown in Figure 7.4 is that the O binds to a neighboring on-top site. In a series of experiments, we obtained the propensities for NO dissociative adsorption on Rh_6^+, Rh_5Ta^+, and Ir_6^+. The found propensities exhibit a strong correlation with the oxygen affinities of the clusters as illustrated, whereas the affinities towards nitrogen are essentially identical (see Figure 7.5). This finding indicates that we are able to predict the NO dissociation efficiency by evaluating the oxygen-atom adsorption energies. This forms a crucial refinement of work by Sakaki and coworkers, who conclude that dissociation is

preferred by metals with strong N- and O-affinities (Ru$_n$ and Rh$_n$ in particular).[25] Here, we conclude that N-affinity facilitates adsorption, whereas it is the O-affinity that governs dissociation efficiency.

In conclusion, from the found dissociation propensities upon adsorption onto clusters with different elemental compositions, we conclude that the oxophilicity of the adsorption site forms a descriptor for the NO cleavage reaction efficiency. Although optimizing catalysts for the overall NO reduction reaction will certainly require more descriptors, we expect that employing the oxophilicity of adsorption sites will become an important figure of merit for the design of tailored NO reduction catalysts.

7.2. Appendix

Detail of the experimental methods, computational methods, procedure of isomeric ratio estimation, histogram of isomers amounts to the relative energies, and geometries and IR spectra of low-lying isomers of Ir$_6$NO$^+$ are written in here.

7.2.1. Experimental Methods

Geometries of cationic Ir$_6^+$NO clusters were investigated by IR multiple-photon dissociation (IRMPD) spectroscopy of their complexes with Ar (Ir$_6^+$NO-Ar) employing the IR free-electron laser FELIX. Clusters were produced using laser ablation of a solid Ir rod (purity: 99.95%) by the second harmonic of a Nd:YAG laser (532 nm) which operated at 20 Hz and a typical pulse energy of ~10 mJ, in the presence of an Ar/He mixture (approx. 0.43% Ar, 0.8 MPa stagnation pressure) injected into clustering channel using a pulsed valve. Generated clusters were reacted with a NO/He reactant gas mixture (approx. 11.11 % NO) which was introduced via a second plused valve (0.1 MPa stagnation pressure) about 30 mm downstream from the laser ablation point. To enhance the attachment of Ar to the cluster, reaction cell was cooled down to temperature of ~200 K.

After formation, the reactive mixture was expanded into vacuum forming a molecular beam which was collimated by a 2 mm diameter skimmer, and a 1 mm diameter aperture before entering the source region of a reflectron time-of-flight mass spectrometer. Prior to extraction by two high-voltage plates, the ions are irradiated by one macropulse of the FELIX laser beam, that was attenuated by fixed value mesh attenuators to prevent saturation of the strongest bands.

The experiment was operated at twice the FELIX repetition rate allowing for the recording of reference mass spectra which were used to correct for source fluctuations.

7.2.2. Computational Methods

The stable structures of Ir_6NO^+ were calclated by quantum chemical calculations using Gaussian 09.[19] Computational procedures were almost same as the one described in our previous article.[23] The density functional theory (DFT) was used for whole calclations of not only motief and viblational freqencies but also the reaction path. To make a complete search of the stable isomers with reduced computational costs, initial geometries, prepared manually and randomly, were optimized, at first, with the LanL2DZ and the 6-31G(d), for Ir and N, O atoms respectively for the conceivable spin states (see Figure 7.6). For the obtained low energy isomers, the geometris were re-optimized using the Becke's three-parameter hybrid density functional with the Lee-Yang-Parr correlation functional (B3LYP) with the Stuttgart/Dresden (SDD, MWB60) basis set and effective core potensial (ECP) for Ir atoms and the 6-311+G(d) basis set for N and O atoms.

Figure 7.5 in the article, is comparison of the binding energy of the O atom adsorbed on an on-top site of Rh_6^+, Ir_6^+ and Rh_5Ta^+ clusters. B3LYP with SDD and 6-311+G(d) were used for optimization, and the zero point energies were included. Those configurations are in their global minimum with the conceivable spin states except for Rh_6^+O. Most stable Rh_6^+O cluster possesses O atom at a hollow site surrounded by three Rh atoms with the 12tet spin state.

7.2.3. Isomeric Ratios

Isomeric ratios in the main text were estimated by comparison between the experimental band intensities and the computational IR intensities. Each band appearing in the IRMPD spectrum was assigned to a vibration of the isomers A, B and C. A band intensity was obtained from the spectral area of the band. The isomeric ratios were calculated based on the values of the band intensity divided by the IR intensity of the corresponding vibration calculated by Gaussian 09. Although observed IRMPD intensities do not necessarily scale linearly with IR laser pulse energy, such a linear power dependence does exist provided the threshold is low.[26] For our studies, we employ Ar tagging, with binding energies of ca 0.1 eV,[15] which ensures we are as close to the linear regime as possible.

To further reduce the effects of a potential non-linear relationship between Ar elimination and IR absorption cross-section, we compared several combinations of assigned bands to calculate the isomeric ratio. For example, to obtain the ratios of molecularly to dissociatively attached clusters, we not only compared the main bands (950 vs 1815 cm^{-1}) but also weaker bands (550, 600, 1050 vs 350 cm^{-1}), and their combinations (550, 600, 1050 vs 1815 cm^{-1}) and (950 vs 350 cm^{-1}). The standard deviation between the ratios obtained in the various ways is lower than 20%, thus ruling out large non-linear effects.

7.3. References

(1)   Kašpar, J.; Fornasiero, P.; Hickey, N. Automotive Catalytic Converters: Current Status and Some Perspectives. *Catal. Today* **2003**, *77* (4), 419–449, https://doi.org/10.1016/S0920-5861(02)00384-X.

(2)   Shimokawabe, M.; Umeda, N. Selective Catalytic Reduction of NO by CO over Supported Iridium and Rhodium Catalysts. *Chem. Lett.* **2004**, *33* (5), 534–535, https://doi.org/10.1246/cl.2004.534.

(3)   Nieuwenhuys, B. E. The Surface Science Approach Toward Understanding Automotive Exhaust Conversion Catalysis at the Atomic Level. *Adv. Catal.* **1999**, *44*, 259–328, https://doi.org/10.1016/S0360-0564(08)60514-3.

(4)   Zasada, I.; Van Hove, M. A.; Somorjai, G. A. Reanalysis of the Rh(111)+(2×2)-3NO Structure Using Automated Tensor LEED. *Surf. Sci.* **1998**, *418* (3), L89–L93, https://doi.org/10.1016/S0039-6028(98)00782-1.

(5)   Kim, Y. J.; Thevuthasan, S.; Herman, G. S.; Peden, C. H. F.; Chambers, S. A.; Belton, D. N.; Permana, H. Chemisorption Geometry of NO on Rh(111) by X-Ray Photoelectron Diffraction. *Surf. Sci.* **1996**, *359* (1–3), 269–279, https://doi.org/10.1016/0039-6028(96)00027-1.

(6)   Nakamura, I.; Kobayashi, Y.; Hamada, H.; Fujitani, T. Adsorption Behavior and Reaction Properties of NO and CO on Rh(1 1 1). *Surf. Sci.* **2006**, *600* (16), 3235–3242, https://doi.org/10.1016/J.SUSC.2006.06.009.

(7)   Wallace, W. T.; Cai, Y.; Chen, M. S.; Goodman, D. W. NO Adsorption and Dissociation on Rh(111): PM-IRAS Study. *J. Phys. Chem. B* **2006**, *110* (12), 6245–6249, https://doi.org/10.1021/jp057134p.

(8)   Fujitani, T.; Nakamura, I.; Kobayashi, Y.; Takahashi, A.; Haneda, M.; Hamada, H. Adsorption and Reactions of NO on Clean and CO-Precovered Ir(111). *J. Phys. Chem. B* **2005**, *109*, 17603–17607, https://doi.org/10.1021/JP053092T.

(9)   Chen, W.; Stottlemyer, A. L.; Chen, J. G.; Kaghazchi, P.; Jacob, T.; Madey, T. E.; Bartynski, R. A. Adsorption and Decomposition of NO on O-Covered Planar and Faceted Ir(2 1 0). *Surf. Sci.* **2009**, *603* (20), 3136–3144, https://doi.org/10.1016/J.SUSC.2009.08.027.

(10)   Johnson, G. E.; Mitrić, R.; Bonačić-Koutecký, V.; Castleman, A. W. Clusters as Model Systems for Investigating Nanoscale Oxidation Catalysis. *Chem. Phys. Lett.* **2009**, *475* (1–3), 1–9, https://doi.org/10.1016/J.CPLETT.2009.04.003.

(11)   Lang, S. M.; Bernhardt, T. M. Gas Phase Metal Cluster Model Systems for Heterogeneous Catalysis. *Phys. Chem. Chem. Phys.* **2012**, *14* (26), 9255–9269, https://doi.org/10.1039/c2cp40660h.

(12)   Tawaraya, Y.; Kudoh, S.; Miyajima, K.; Mafuné, F. Thermal Desorption and Reaction of NO Adsorbed on Rhodium Cluster Ions Studied by Thermal Desorption Spectroscopy. *J. Phys. Chem. A* **2015**, *119* (31), 8461–8468, https://doi.org/10.1021/acs.jpca.5b04224.

(13)   Anderson, M. L.; Ford, M. S.; Derrick, P. J.; Drewello, T.; Woodruff, D. P.; Mackenzie, S. R. Nitric Oxide Decomposition on Small Rhodium Clusters, $Rh_n^{+/-}$. *J. Phys. Chem. A* **2006**, *110* (38), 10992–11000, https://doi.org/10.1021/jp062178z.

(14)   Hirabayashi, S.; Ichihashi, M. Effects of Second-Metal (Al, V, Co) Doping on the NO Reactivity of Small Rhodium Cluster Cations. *J. Phys. Chem. A* **2017**, *121* (13), 2545–2551, https://doi.org/10.1021/acs.jpca.6b11613.

(15)   Nagata, T.; Koyama, K.; Kudoh, S.; Miyajima, K.; Bakker, J. M.; Mafune, F. Adsorption Forms of NO on Rh_n^+ ($n = 6-16$) Revealed by Infrared Multiple Photon Dissociation Spectroscopy. *J. Phys. Chem. C* **2017**, *121* (49), 27417–27426, https://doi.org/10.1021/acs.jpcc.7b08097.

(16)   Nagata, T.; Kudoh, S.; Miyajima, K.; Bakker, J. M.; Mafuné, F. Adsorption of Multiple NO Molecules on Rh_n^+ ($n = 6, 7$) Investigated by Infrared Multiple Photon Dissociation Spectroscopy. *J. Phys. Chem. C* **2018**, *122* (40), 22884–22891, https://doi.org/10.1021/acs.jpcc.8b04729.

(17) Hermes, A. C.; Hamilton, S. M.; Hopkins, W. S.; Harding, D. J.; Kerpal, C.; Meijer, G.; Fielicke, A.; Mackenzie, S. R. Effects of Coadsorbed Oxygen on the Infrared Driven Decomposition of N_2O on Isolated Rh_5^+ Clusters. *J. Phys. Chem. Lett.* **2011**, *2* (24), 3053–3057, https://doi.org/10.1021/jz2012963.

(18) Hamilton, S. M.; Hopkins, W. S.; Harding, D. J.; Walsh, T. R.; Gruene, P.; Haertelt, M.; Fielicke, A.; Meijer, G.; Mackenzie, S. R. Infrared Induced Reactivity on the Surface of Isolated Size-Selected Clusters: Dissociation of N_2O on Rhodium Clusters. *J. Am. Chem. Soc.* **2010**, *132* (5), 1448–1449, https://doi.org/10.1021/ja907496c.

(19) Frisch, M. J.; Trucks, G. W.; Schlegel, H. B.; Scuseria, G. E.; Robb, M. A.; Cheeseman, J. R.; Scalmani, G.; Barone, V.; Mennucci, B.; Petersson, G. A.; Nakatsuji, H.; CT, W.; et al. Gaussian 09, Revision E.01. Gaussian 09 2013.

(20) Cornish, J. C. L.; Avery, N. R. Adsorption of N_2, O_2, N_2O and NO on Ir(111) by EELS and TPD. *Surf. Sci.* **1990**, *235* (2–3), 209–216, https://doi.org/10.1016/0039-6028(90)90795-A.

(21) Zeigarnik, A. V. Adsorption and Reactions of N_2O on Transition Metal Surfaces. *Kinet. Catal.* **2003**, *44* (2), 233–246, https://doi.org/10.1023/A:1023308629868.

(22) Watanabe, K.; Kokalj, A.; Horino, H.; Rzeznicka, I. I.; Takahashi, K.; Nishi, N.; Matsushima, T. Scanning-Tunneling Microscopy, Near-Edge X-Ray-Absorption Fine Structure, and Density-Functional Theory Studies of N_2O Orientation on Pd(110). *Jpn. J. Appl. Phys.* **2006**, *45* (3B), 2290–2294, https://doi.org/10.1143/JJAP.45.2290.

(23) Yamaguchi, M.; Kudoh, S.; Miyajima, K.; Lushchikova, O. V.; Bakker, J. M.; Mafuné, F. Tuning the Dissociative Action of Cationic Rh Clusters Toward NO by Substituting a Single Ta Atom. *J. Phys. Chem. C* **2019**, *123* (6), 3476–3481, https://doi.org/10.1021/acs.jpcc.8b08575.

(24) Zhou, X.; Yang, J.; Li, C. Theoretical Study of Structure, Stability, and the Hydrolysis Reactions of Small Iridium Oxide Nanoclusters. *J. Phys. Chem. A* **2012**, *116* (40), 9985–9995, https://doi.org/10.1021/jp3064068.

(25) Takagi, N.; Ishimura, K.; Fukuda, R.; Ehara, M.; Sakaki, S. Reaction Behavior of the NO Molecule on the Surface of an M n Particle (M = Ru, Rh, Pd, and Ag; n = 13 and 55): Theoretical Study of Its Dependence on Transition-Metal Element. *J. Phys. Chem. A* **2019**, *123* (32), 7021–7033, https://doi.org/10.1021/acs.jpca.9b04069.

(26)   Berden, G.; Derksen, M.; Houthuijs, K. J.; Martens, J.; Oomens, J. An Automatic
        Variable Laser Attenuator for IRMPD Spectroscopy and Analysis of Power-
        Dependence in Fragmentation Spectra. *Int. J. Mass Spectrom.* **2019**, *443*, 1–8,
   https://doi.org/10.1016/j.ijms.2019.05.013.
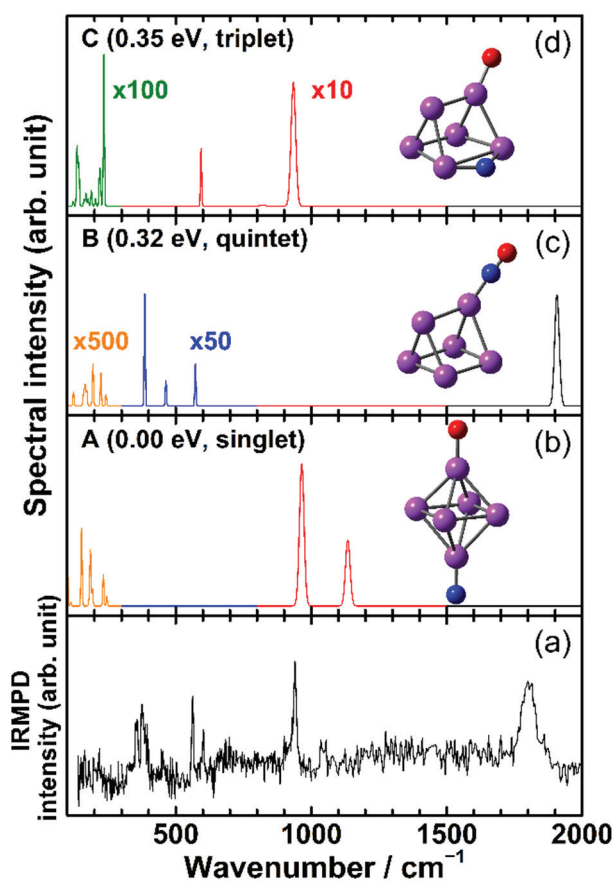
Figures

Figure 7.1. (a) IRMPD spectrum for Ir_6^+ NO-Ar and (b–d) DFT calculated vibrational spectra of the stable isomers of Ir_6^+NO. The relative energy of formation and spin multiplicity are shown in parentheses for each structure. Blue, red, and purple balls represent N, O, and Ir atoms, respectively (see Figure 7.2 for other isomers). The scaling factor was not applied to calculation results.
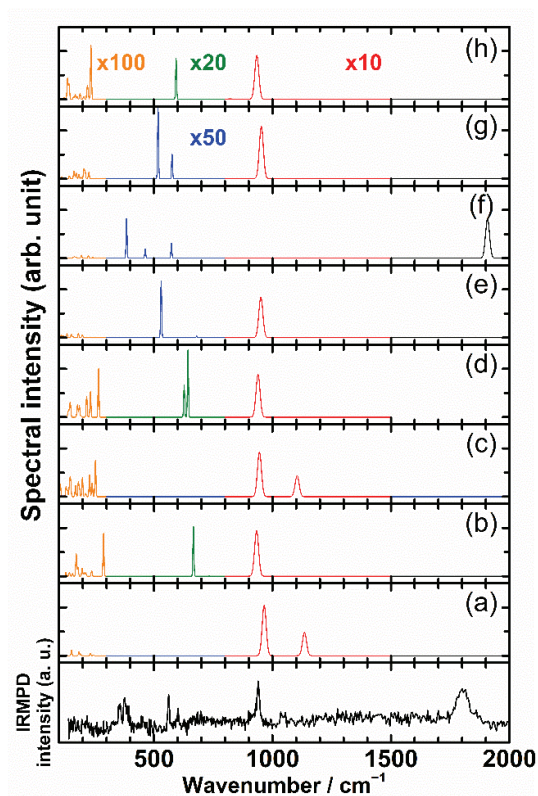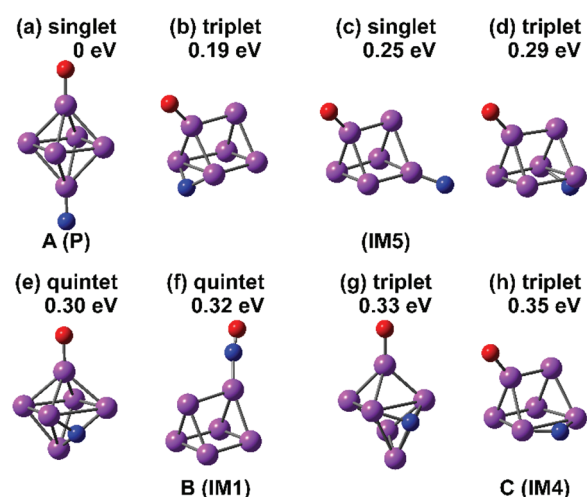
Figure 7.2. (a−h) Stable isomers of Ir_6^+NO and their vibrational spectra obtained by DFT calculations and IRMPD spectrum of Ir_6^+NO-Ar. Geometrical structures that are very similar to those appearing in Figure 7.3, but differing in spin, are nevertheless displayed using the same labels as in Figure 7.3, even though calculations displayed in Figure 7.3 were performed in the quintet spin state only.
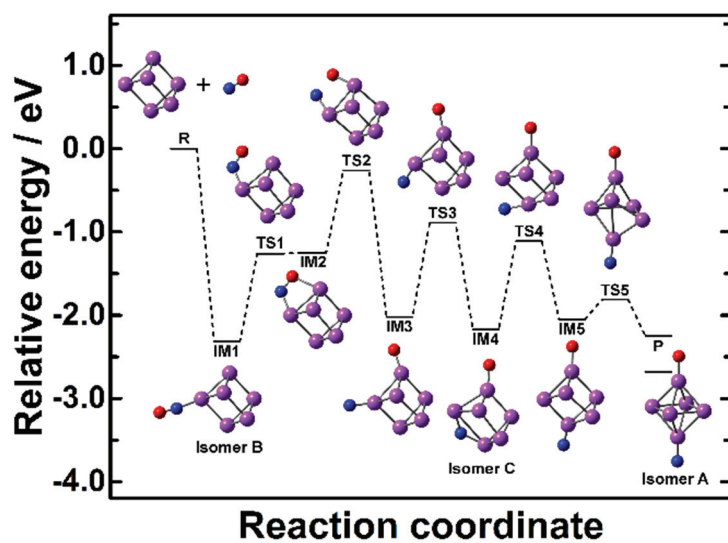
Figure 7.3. Reaction pathway for NO dissociation on Ir_6^+, calculated on the quintet spin surface. R, IM, TS and P indicate reactant, intermediate, transition state, and product, respectively. The most stable spin isomer of P (singlet) is also shown. Geometries of IM1, IM4 and P correspond to isomers B, C and A in Figure 7.1, respectively.
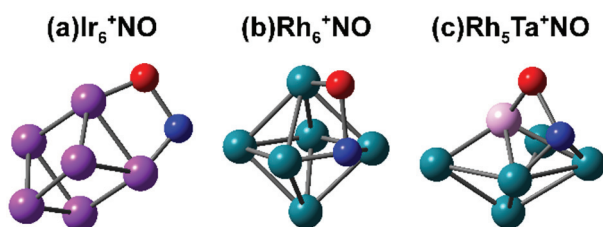
Figure 7.4. Geometrical structures of (a) Ir_6^+NO (b) Rh_6^+NO and (c) Rh_5Ta^+NO in the transition state for bond cleavage.
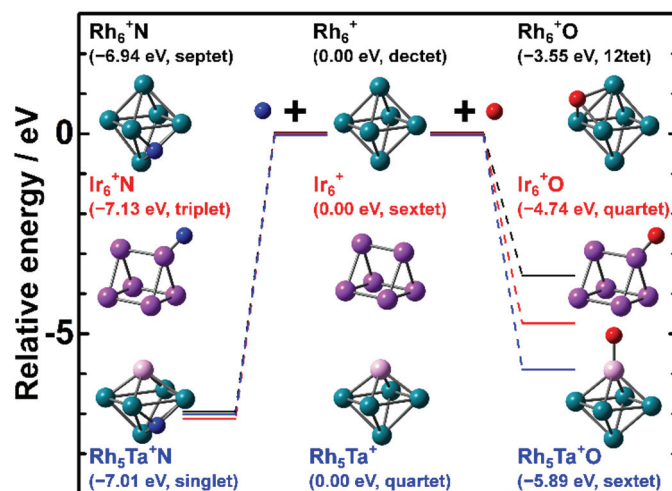
Figure 7.5. N- and O-atom affinities of the metal cationic clusters.
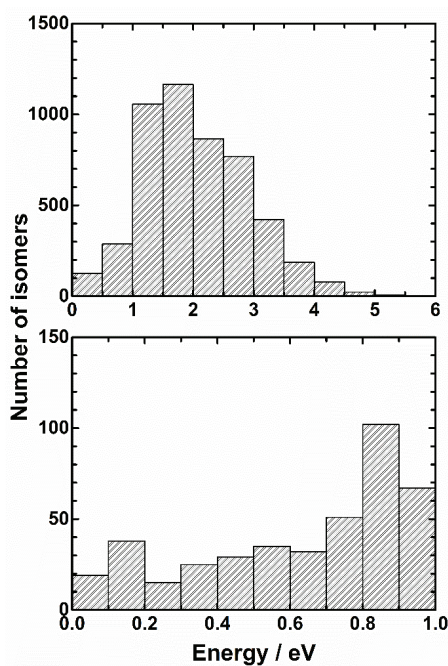
Figure 7.6. (a) Histogram showing the number of isomers obtained by the initial optimization for Ir_6^+NO by the DFT calculations using LanL2DZ basis sets from randomly set 5000 initial geometries, which is plotted against the difference in the formation energy from the most stable isomer. (b) Expanded histogram of (a) in the 0−1 eV energy range for each 0.1 eV.

Chapter 8

General Conclusion

8.1. Summary and Conclusion

In this thesis, I conducted research relating to precious metals, namely, Au, Rh, and Ir. The studies were focused on gas-phase clusters and were performed using thermal desorption spectrometry (TDS), infrared multiple-photon dissociation (IRMPD) spectroscopy, and quantum chemical calculations to elucidate the chemical properties and geometries..

The TDS analysis of $Au_nO_m^-$ anionic clusters showed an O_2 release trend with increasing temperature (Chapter 2). Typically, desorption temperatures decreased with the cluster size, n: $Au_2O_2^-$ maintained its composition until 600 K, whereas clusters with $n = 4$–14 showed complete desorption of O_2 in the same temperature range. The activation energies of these desorption processes were determined by fitting the Arrhenius equation to the experimental data. The low activation energies suggest that O_2 was attached intact.

The experiments using N_2O as the reactant revealed the presence of a variety of oxygen-attached clusters, $Au_nO_m^-$ ($n = 1$–12, $m = 0$–7), while experiments using O_2 indicated that only molecularly attached clusters were present (Chapter 3). The TDS analysis for clusters with $m = 2$ also showed different results from those using O_2: no desorption was observed until 1000 K. Thus, geometrical isomers are believed to be produced because of the different thermal responses. The results of the quantum chemical calculations suggested that the clusters with atomically adsorbed O were significantly more stable than those with molecularly adsorbed clusters. From the experiment about the oxidants, I could conclude that different geometrical isomers can be prepared.

NO- and NO_2-attached Au clusters, especially $Au_4(NO)_n^-$ ($n = 0$–3) and $Au_4NO_2^-$, were investigated using a combination of TDS, concentration dependence, and quantum chemical calculations (Chapter 4). The desorption energies of NO were determined to be lower than 1.0 eV, implying intact NO adduction. The detachment of NO_2 from $Au_4NO_2^-$ also occurred around 900 K, as revealed by the TDS results, and it was concluded that the attachment of NO_2 was

also intact. Moreover, the IRMPD spectra support these results and confirms that the geometries were accurately determined (Chapter 5).

The Ta-atom-doped Rh clusters, Rh_nTa^+ ($n = 2$–8), showed dissociatively attached NO, as revealed by IRMPD spectroscopy (Chapter 6). In particular, the Rh_5Ta^+ cluster possesses NO in the dissociative form, whereas almost all NO existed molecularly on Rh_6^+.[1] In the experiment on Ir clusters belonging to the same group as Rh, group IX, several geometrical isomers are indicated to be present in the generated clusters (Chapter 7). These isomers appeared in the reaction pathway of NO dissociation; hence, they were considered to be trapped at each metastable state. Based on these results, it was suggested that the dissociation ability of NO is dominated by oxophilicity (Figure 8.1).

8.2. Prospects

In this research, I explored and elucidated the chemical properties and molecular geometries of precious metal clusters. Here, I will focus on two topics as prospects.

In the series of experiments on $Au_nO_m^-$ clusters, I determined that the form of oxygen atoms on gold clusters can be controlled by using different oxidants such as O_2 and N_2O. Further investigation related to Au clusters, in combination with transition metal oxides (TMOs), could be conducted. As revealed in previous studies, bulk Au supported on TMO undergoes a low-temperature oxidation reaction wherein the oxygen form is important, and the oxygen molecules have collapsed into oxygen atoms.[2,3] In the cluster experiment, CO oxidation using Au has been reported.[4–6] In either case, separated oxygen atoms played an important role in the reaction scheme. Thus, oxygen adduction confirmed in the present study may facilitate the evaluation of the CO oxidation mechanism by comparing it with Au-TMO alloy clusters.

Under experiments for IX group elements, I reported NO dissociation reactions focused on the oxygen affinity of clusters. The high efficiency of NO rupture by Ta-doped Rh clusters, especially the Rh_5Ta^+ cluster, is one of the typical results of the effect of alloying elements, while the pure Rh_6^+ cluster showed hardly any NO dissociation. Nevertheless, the presence of a large population of NO-dissociated clusters implies that they have high stability. This may result in no O_2 or N_2 desorption through the presence of multiple NO attachments. In addition, the Ir cluster, one of the group IX metals, possesses several geometrical isomers with not only dissociatively but also molecularly attached NO. I concluded that these differences can be evaluated by determining the oxophilicity of each cluster, as shown in Figure 8.1. This insight

may advance further exploration of state-of-the-art catalysis through screening by recently developed computational systems.

8.3. References

(1)   Nagata, T.; Koyama, K.; Kudoh, S.; Miyajima, K.; Bakker, J. M.; Mafune, F. Adsorption Forms of NO on Rh_n^+ ($n = 6-16$) Revealed by Infrared Multiple Photon Dissociation Spectroscopy. *J. Phys. Chem. C* **2017**, *121* (49), 27417–27426, https://doi.org/10.1021/acs.jpcc.7b08097.

(2)   Haruta, M. Gold as a Novel Catalyst in the 21st Century: Preparation, Working Mechanism and Applications. *Gold Bull.* **2004**, *37* (1–2), 27–36, https://doi.org/10.1007/BF03215514.

(3)   Saavedra, J.; Pursell, C. J.; Chandler, B. D. CO Oxidation Kinetics over Au/TiO_2 and Au/Al_2O_3 Catalysts: Evidence for a Common Water-Assisted Mechanism. *J. Am. Chem. Soc.* **2018**, *140* (10), 3712–3723, https://doi.org/10.1021/jacs.7b12758.

(4)   Socaciu, L. D.; Hagen, J.; Bernhardt, T. M.; Wöste, L.; Heiz, U.; Häkkinen, H.; Landman, U. Catalytic CO Oxidation by Free Au_2^- Experiment and Theory. *J. Am. Chem. Soc.* **2003**, *125*, 10437–10445, https://doi.org/10.1021/ja027926m.

(5)   Wallace, W. T.; Whetten, R. L. Coadsorption of CO and O_2 on Selected Gold Clusters: Evidence for Efficient Room-Temperature CO_2 Generation. *J. Am. Chem. Soc.* **2002**, *124*, 7499–7505, https://doi.org/10.1021/JA0175439.

(6)   Li, X.-N.; Yuan, Z.; He, S.-G. CO Oxidation Promoted by Gold Atoms Supported on Titanium Oxide Cluster Anions. *J. Am. Chem. Soc.* **2014**, *136* (9), 3617–3623, https://doi.org/10.1021/ja412608b.

Figures

Figure 8.1. Varying NO bond cleavage for precious metal clusters. Isomeric ratios were directly calculated from the results of IRMPD spectroscopy and dissociation abilities against NO appear to have a correlation with the oxygen affinities for each cluster.

Acknowledgements

in this year. Although we have no collaborated research at present, I will appreciate it if we have opportunity to make that in near future.

Mr. Yufei Zhang is the second grade of doctor course student. He went to the FELIX twice with me. He has great perseverance against the research, and helped me not only aspects of research but also the daily life. I would like to express the appreciation.

I grateful to a technical staff in our department, Mr. Norio Nakajima. He has helped me to make equipment, and instructed how to use metal working machines.

I would like to thank present members of our laboratory, Mr. Kimihiro Kawada, Ms. Xuemei Chen, Ms. Tianyue Zhou, Mr. Keitaro Tatsukawa and Ms. Naoko Suzuki. Additionally, I also would like to thank Ms. Olga V. Lushchikova (FELIX Laboratory, Radboud University, Netherlands), Mr. Haohao Wang, Mr. Kohei Koyama, Mr. Daigo Masuzaki, Ms. Nako Kawashima, Ms. Manami Abe, Ms. Xinan Liu, Mr. Yuma Takehashi, Mr. Jun Yamagishi, Ms. Akari Yamada, and all of the person who related to my life.

Finally, I would like to appreciate to my family.

Tokyo, Japan, December 2020

Masato Yamaguchi